UNIVERSITÀ DI TRENTO
Department of Industrial Engineering
XXXVI cycle

Doctoral School in Materials,
Mechatronics and Systems Engineering

Functional interphases for structural composites

Laura Simonini

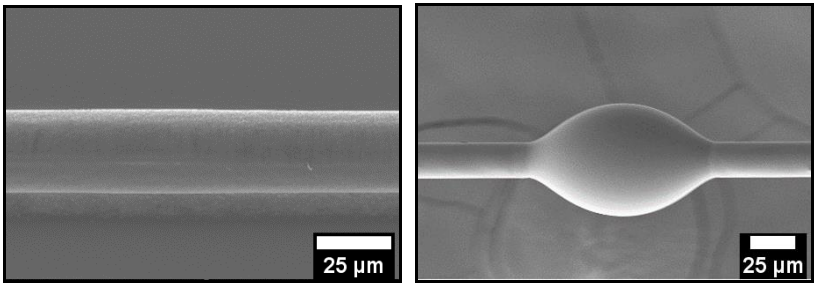

July 2024

Functional interphases for structural composites

Laura Simonini
e-mail: laura.simonini@unitn.it

Approved by:

Prof. Alessandro Pegoretti, Adv.
Dept. of Industrial Engineering
University of Trento, Italy

Prof. Andrea Dorigato, Adv.
Dept. of Industrial Engineering
University of Trento, Italy

PhD Commission:

Prof. Marino Quaresimin
Dept. Of Management and Engineering
University of Padua, Italy

Prof. Fabrizio Sarasini
Dept. of Chemical Engineering Materials Environment
University of Rome "La Sapienza", Italy

Prof. Devid Maniglio
Dept. of Industrial Engineering
University of Trento, Italy

University of Trento,
Department of Industrial Engineering
July 12, 2024

University of Trento – Department of Industrial Engineering
Doctoral Thesis
Laura Simonini – 2024

Cover image: SEM micrographs of a poly(ϵ-caprolactone) coated glass fiber (left) and a microcomposite formed by a glass fiber and an epoxy microdroplet (right).

To my family

Abstract

Safety of buildings and other structures is of great importance in engineering, since the structural integrity of a component may be compromised over time due to a variety of internal and external loads. The use of advanced materials, such as fiber-reinforced composites (FRCs), has become essential in construction due to their superior properties. However, FRCs suffer from interfacial debonding, i.e. the nucleation and the propagation of cracks at the contact region between matrix and fibers. Robust interfacial adhesion and self-healing capability are crucial to reduce defects and extend the material service life. The intent of this Doctoral Thesis was to provide a contribution in this field, by focusing on two primary research areas: the enhancement of the interfacial adhesion and the development of self-healing interfacial capability. Both research areas involved the investigation of microscale interfacial properties through the fabrication of microcomposites subjected to microdebonding tests, in order to allow highly accurate estimations of the interfacial properties.

In the first research area, two innovative methods such as triboelectrification and laser treatment were explored. Triboelectrification involved the rubbing of glass fibers (GFs) against a polytetrafluoroethylene (PTFE) surface to generate surface charge, therefore to attract graphene oxide (GO) nanosheets on the fibers and to create a compact and homogeneous coating. The resulting interfacial adhesion with epoxy resin (EP), which was expressed as interfacial shear strength (IFSS), was enhanced up to 45% compared to neat fibers. On the other hand, basalt fibers were treated with CO_2 laser to increase their mechanical interlocking with the EP, and in this case a 8% improvement in IFSS was obtained.

In the second research area, a continuous film and a nanostructured coating made of poly(ϵ-caprolactone) (PCL) were deposited on GFs and carbon fibers (CFs) to impart interfacial self-healing properties. Scanning electron microscopy and optical microscopy analyses

confirmed the formation of well-applied and homogeneous coatings. In the case of the PCL film, an increase of 16% in IFSS with EP was obtained, while in the case of the PCL nanostructured coating different effects on IFSS were obtained, ranging from +26% for glass fibers to -60% for carbon fibers. Self-healing efficiency (H.E.), calculated as the ratio of IFSS before and after thermal mending, reached an impressive 100% for the PCL-film coated GFs, with a gradual decrease over multiple debonding/healing cycles. An alteration of the matrix droplet's meniscus was observed, which was hypothesized being the cause of the decrease over multiple H.E., due to the modification of the stress state near the fiber/droplet contact point. Moreover, also in the case of PCL-nanocoated CFs, the interfacial debonding was completely restored.

Future steps of this research will include the development of a finite element model (FEM) of the interfacial region to simulate the microdebonding test and to provide a comprehensive understanding of the interfacial debonding and healing mechanisms over multiple healing cycles.

Contents

List of Figures

List of Tables

List of Acronyms

AFM	Atomic force microscopy
BF	Basalt fiber
CF	Carbon fiber
DSC	Differential scanning calorimetry
E1/E2	Steel electrodes
EP	Epoxy resin
FRC	Fiber-reinforced composite
GF	Glass fiber
sGF	Silane sized glass fiber
uGF	Unsized glass fiber
GO	Graphene oxide
rGO	Reduced graphene oxide
HFM	Heat flux meter
IFSS	Interfacial shear strength
ILSS	Interlaminar shear strength
LOI	Limit oxygen index
MB	Microdebonding tests
NEF	Non-electrified fibers
OM	Optical microscopy
PCL	Poly(ϵ-caprolactone)
PCM	Polymer matrix composites
PF	Phenolic resin
PTFE	Polytetrafluoroethylene
PU	Polyurethane
SEM	Scanning electron microscopy
TE	Triboelectric effect
TGA	Thermogravimetric analysis
dTG	First derivative TGA
1T	1-PTFE path
2T	2-PTFE path

List of Symbols

ϱ_{app}	Apparent density	g/cm^3
R_a	Arithmetic mean roughness	nm
P_{closed}	Closed porosity	%
η	Complex viscosity	Pa·s
E_c	Compression modulus	MPa
σ_c	Compression stress	MPa
E	Elastic modulus	MPa
E_f	Flexural modulus	MPa
σ_f	Flexural stress	MPa
ϱ_{geom}	Geometrical density	g/cm^3
T_g	Glass transition temperature	°C
H.E.	Healing efficiency	%
IFSS	Interfacial shear strength	MPa
LOI	Limit oxygen index	%
T_{max}	Maximum degradation temperature	°C
T_m	Melting temperature	°C
M_w	Molecular weight	g/mol
wt%	Percentage by weight	%
m_{700}	Residual mass (from TGA)	%
σ_0	Scale factor	
m	Shape parameter	
G''	Shear loss modulus	Pa
G'	Shear storage modulus	Pa
E''	Tensile loss modulus	Pa
E'	Tensile storage modulus	Pa
σ_s	Tensile strength at yield	MPa
ϱ_{th}	Theoretical density	g/cm^3
λ	Thermal conductivity	W/m·K
ϱ_v	Volumetric resistivity	Ω·m
ζ	Zeta potential	mV

1 Introduction

1.1 Motivation and objectives

The structural integrity of a building component is of great importance in engineering, since it may be compromised over time due to a variety of internal and external loads. The early identification of defects is therefore crucial to ensure the structural reliability. However, defects location and external maintenance are often particularly challenging due to hostile environments or inappropriate instrumentations. The current solution is the use of Structural Health Monitoring Systems (SHMS) that involve the continuous observation of the architectural integrity by using network of connected sensors. SHMS enable damage detection, damage location, damage assessment, and service-life prediction, and are employed in the construction, transportation and civil sectors. However, besides the good strategies coming from the sensing technologies, the attention of material engineers is focused on the development of advanced and high-performance materials, prior to address the aspects of their post-construction maintenance.

In this scenario, fiber-reinforced composites (FRC) find large applications, since they offer improved strength, stiffness, fatigue and impact resistance than conventional materials. However, they suffer from interfacial debonding, i.e. the nucleation and the propagation of defects at the contact region between matrix and fibers, with detrimental effects on the overall mechanical properties of the material. A robust interfacial adhesion ensures an effective load transfer from the “weak” matrix to the “strong” fibers, and therefore allows an optimal stress distribution and relaxation within the material.

Along with interfacial adhesion, interfacial self-healing is of paramount importance. Self-healing enables the material to autonomously repair minor defects that may occur during service, which includes micro-cracks at the matrix-fiber contact region. This

ability to self-repair mitigates the propagation of defects, extends the operational life of the composite, reduces maintenance frequency, and ultimately enhances the structural safety and lifetime of the structures.

Therefore, the concurrent advance of both the interfacial adhesion and the interfacial self-healing in FRCs allows the fabrication of structural materials that embody safety, durability, and sustainability, and opens the way for a new generation of materials that can effectively meet the demanding requirements of modern infrastructures.

In this sense, this Doctoral Thesis is presented to address the two main topics. The first part focuses on the exploration of some innovative methods to improve the *interfacial adhesion* between the matrix and the fibers. Through the utilization of triboelectrification and laser treatments on fiber surface, the interfacial bonding was notably improved resulting in the enhancement of fiber/matrix strength. This part is discussed in **Chapter 4 (Evaluation of the fiber/matrix interfacial adhesion)**.

The second part focuses on the exploration of innovative methods to provide the *interfacial self-healing capability*. The development of a thermoplastic coating on fiber surface offered interfacial healing, which was enabled by the application of an external temperature. This part is discussed in **Chapter 5 (Evaluation of the fiber/matrix interfacial self-healing).**

For both research topics, the key aspect was the investigation of the interfacial properties at microscale level, which involved the fabrication of microcomposites subjected to microdebonding tests. These tests required precise manipulation and analysis, but allowed to achieve extremely accurate estimations of the interfacial properties.

In conclusion, the importance of both the enhancement of interfacial adhesion and the implementation of interfacial self-healing mechanisms have been comprehensively investigated and discussed in this Thesis. This dual approach highlighted the multifaceted

nature of composite materials, and provided an extensive framework for future advancements in the field.

1.2 Thesis outline

This Doctoral Thesis is divided into eight Chapters:

- *Chapter 2* presents a detailed literature review on composites materials, interfacial properties and methodologies to achieve high performance composite materials.
- *Chapter 3* describes the materials and the experimental techniques used to prepare and characterize the samples.
- *Chapter 4* and *Chapter 5* contain the results of the main two topics of the research activity, i.e. the "Evaluation of the fiber/matrix interfacial adhesion" and "Evaluation of the fiber/matrix interfacial self-healing", respectively.
- *Chapter 6* contains concluding remarks and the main recommendations for future research on this topic.
- *Chapter 7* summarizes the results of two side works on different research topics.
- *Chapter 8* contains the bibliography.
- Finally, a list of *publications*, national and international *awards*, participation to *congresses* and *summer school*, a *visiting period* spent abroad, and *teaching activities* carried out during the Doctoral Program, is presented.

2 Scientific background

A composite is a structural material that consists of two or more different phases, mainly recognized as the reinforcing phase embedded in a matrix [1]. Many natural and artificial materials are of this nature, such as human bone and teeth, wood, filled polymers, reinforced rubbers, concrete, alloys, aligned and chopped fiber composites, etc [2].
In **Chapter 2 – Scientific background**, a detailed description of what is a composite material and what are the role and the characteristics of the reinforcing phase and the matrix is discussed. A particular attention is devoted to the description of the interphase, i.e. the region between reinforcement and matrix, with the focus on its properties, possible technological improvements and potential multi-functionalization to achieve advanced structural composites.

2.1 Composite materials

Composite materials are used in a variety of applications such as aerospace, automotive, industrial, structural and domestic products [3]. They offer several advantages over conventional materials, as improved strength, stiffness, fatigue, impact resistance and thermal conductivity. They also find application in corrosive environment to replace metal parts that are prone to corrosive attacks [4]. Composites are fabricated by reinforcements (fibers, particles, flakes, fillers) embedded in a continuous matrix. Figure 2.1 shows the main building steps of fiber-reinforced composites (FRCs), from micro-mechanic to the final structural component [5].

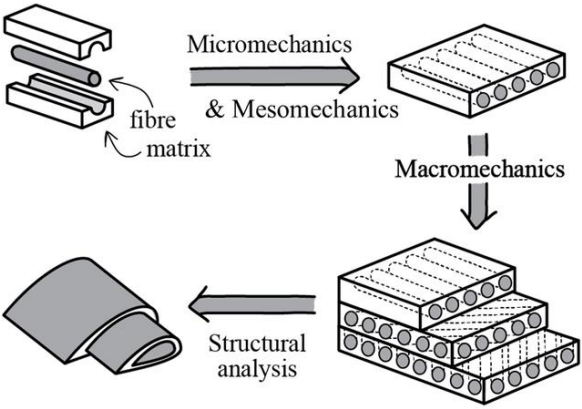

Figure 2.1 Composite structure: matrix and fibers, from micromechanics to the final structural component [5].

The monolithic materials cannot always meet the demands of advanced technological applications. Therefore, the combination of different materials as reinforcement and matrix in composites allows to improve those properties that would be otherwise inferior. This is possible only if the phases in contact possess good interfacial adhesion to enable the adequate load transfer from the "weak" matrix to the "strong" reinforcement. In Figure 2.2, six primary material properties (strength, toughness, formability, joinability, corrosion resistance, affordability) are plotted [6]. The shaded areas show values provided by metal, ceramic, and metal-ceramic composites. It is clear from the figure that the composite shows better strength than metals, and lower values of the other material parameters.

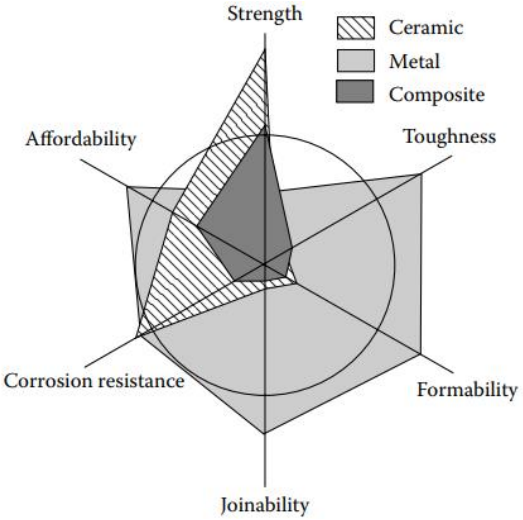

Figure 2.2 Primary material parameters for metals, ceramics and metal-ceramic composites [6].

In composites, the matrix can be either polymeric, metallic or ceramic. It holds and protects the reinforcements and transfer the load to them. Particles or fibers are mainly used as the reinforcing part, but they are also used to enhance the electrical, thermal, magnetic properties and abrasion resistance of the composite [7]. Fibers are characterized by high elastic modulus and tensile strength. Examples are glass fibers, carbon fibers, polymeric and natural fibers. Their orientation in composite laminates can be different according to the final properties required [8]. The Rule of Mixture [9] is useful to predict the composite elastic modulus and Poisson's ratio values. It comes from the hypothesis that the composite is loaded in longitudinal direction and the load carried by the composite is shared between the fibers and the matrix. By dividing the load for the cross-sectional areas of composite, fibers and matrix, it is possible to obtain the stresses acting on composite (σ_c), fibers (σ_f) and matrix (σ_m) (Equation 2.1). Assuming a perfect bond between fibers and

matrix, no slip occurs at the interface and therefore, the strain of the fibers and the matrix is equal to that of the composite. By dividing the stresses for the strain, it is possible to obtain the longitudinal elastic modulus of the composite (E_1), that is the sum of the elastic contributes of fibers and matrix multiplied by their volume fraction (Equation 2.2). For the transverse modulus (E_2) the inverse rule of mixture is considered (Equation 2.3), obtained by substituting the strain for the ratio between stress and modulus and considering $\sigma_c = \sigma_f = \sigma_m$. E_m and V_m are the elastic modulus and the volume fraction of the matrix, instead E_f and V_f the ones related to the reinforcement. The major Poisson's ratio υ_{12} is defined as the ratio between the composite's strains in longitudinal and transverse direction. It is given by the sum of the Poisson's ratios of reinforcement υ_f and of the matrix υ_m (Equation 2.4).

$$\boldsymbol{\sigma_c = \sigma_f V_f + \sigma_m V_m} \quad 2.1$$

$$\boldsymbol{E_1 = E_f V_f + E_m V_m} \quad 2.2$$

$$\frac{\boldsymbol{1}}{\boldsymbol{E_1}} = \frac{\boldsymbol{V_f}}{\boldsymbol{E_f}} + \frac{\boldsymbol{V_m}}{\boldsymbol{E_m}} \quad 2.3$$

$$\boldsymbol{\upsilon_{12} = \upsilon_f V_f + \upsilon_m V_m} \quad 2.4$$

2.1.1 Reinforcements

The role of the reinforcement in composite materials is to enhance the mechanical properties of the matrix (such as tensile and flexural properties, and fracture toughness) [10]. When the matrix is exposed to high mechanical loads that cannot withstand, microcracks can be formed. Therefore, the stress is transferred to the reinforcements that act as crack bridge slowing down the crack growth, as depicted in Figure 2.3 [11]. The breakage or the pullout of the reinforcements dissipate the strain energy at the crack tip, braking the crack propagation.

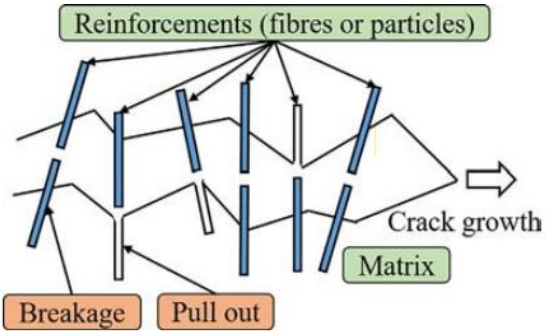

Figure 2.3 Schematization of the role of reinforcement during crack propagation in the matrix [11].

In addition to enhance the mechanical properties, the reinforcements can also improve the thermal property and acoustic performance of composites. For example the introduction of conductive reinforcement, such as carbon nanotubes (CNTs), aluminium and silicon carbide (SiC), have been used to increase the thermal conductivity of polymer composites [12-14], while the use of natural fibers such as flax and feather have been used to reduce and dissipate vibration [15] and sound energy [16].

The conventional reinforcement materials include glass, carbon, plastic (i.e., aramid, polypropylene, and nylon), steel, ceramic, and plant-based natural fibers. The conventional reinforcement forms include fibers, flakes or particles, as shown in Figure 2.4(a, c) [17].

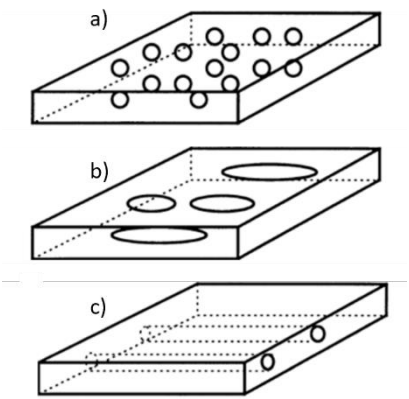

Figure 2.4 Conventional reinforcements in composite materials: (a) particles, (b) flakes, and (c) fibers [17].

Carbon and glass fibers carry the higher tensile modulus and strength compared to other fiber materials, therefore are most often used to reinforce polymer matrices, forming fiber-reinforced polymers (FRPs). Their mechanical properties are strictly correlated to their diameter, in fact as the fibers become smaller in diameter, the possibility of inherent flaws in the material are reduced (Figure 2.5) [18].

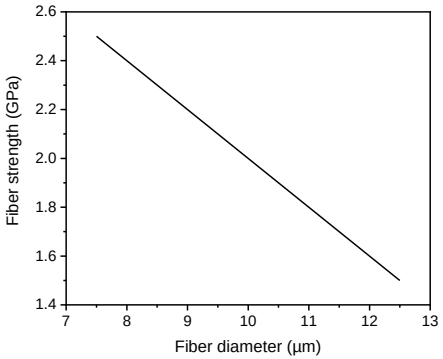

Figure 2.5 Fiber strength as a function of fiber diameter for carbon fibers [18].

Table 2.1 summarizes the tensile properties and density of fibers used in FRPs [11].

Table 2.1 Tensile properties and density of fibers used in fiber-reinforced polymer (FRP) composites [11].

Material	Tensile strength (MPa)	Tensile modulus (GPa)	Elongation at break (%)	Density (g/cm³)
Glass fibers				
E-glass	1800-3500	75	2.0-3.5	2.6
AR-glass	1800-300	75	2.0-3.0	2.7
Plastic fibers				
Polypropylene	400-750	1-18	5.0-20.0	0.9
KEVLAR 29	2800-3600	65	4.0	1.5
Polyvinyl alcohol	1600	30	6.0	1.3
Carbon fibers				
PAN-based	1925-6200	230-595	0.4-1.2	1.7-1.9
Pitch-based	2275-4060	170-980	0.2-0.7	2.0-2.2
Rayon-based	2070-2760	415-550	-	1.7
Natural fibers				
Sisal	511-635	9-22	2.0-2.5	1.5
Flax	345-1035	28	2.7-3.2	1.5
Basalt	1850-4800	70-100	2.5-3.5	2.5-2.9

AR = alkali resistant
PAN = Polyacrylonitrile

Not only the type of material, but also length, orientation and shape of the reinforcement can influence the mechanical properties of the final composites [19].

- *Length:* long fibers provide impact resistance, low shrinkage, improved surface finish, and dimensional stability, while short fibers are easy to work with, and have faster production times. Short fibers have fewer flaws and therefore have higher strength.

- *Orientation:* the composites behave as an isotropic material if the fibers are randomly distributed in the matrix. On the other hand, the composite have main load-carrying directions if the fibers are ordinally distributed in the matrix. Flakes (such as glass, mica, graphite, and aluminium) are usually parallel each other in composites, providing the strength to the matrix in 2D manner. Particles (such as aluminium, ceramic SiC, nano silica or nano-carbon) are generally randomly dispersed in the matrix, forming isotropic composites.
- *Shape:* fibers are usually circular in section due to their easier handling and manufacturing. However, also hexagon and square shaped fibers can be used, but their advantages of strength and high packing factors do not compensate for the drawback in handling and processing.

2.1.1.1 Glass fibers

Glass fibers (GFs) are characterized by mechanical strength and high elastic modulus, low weight, thermal resistance, dimension stability, humidity and corrosion resistance, easy production and low price [20]. They can be found in the form of:

- E (electrical) - glass fibers (low electrical conductivity)
- S (strength) - glass fibers (high strength)
- C (chemical) - glass fibres (high chemical durability)
- M (modulus) - glass fibers (high stiffness)
- A (alkali) - glass fibers (high alkali or soda lime glass)
- D (dielectric) - glass fibers (low dielectric constant)

In particular, the majority of glass fibers production is constituted by E-glass and S-glass, and their chemical composition is reported in Table 2.2 [21].

Table 2.2 Typical E-glass and S-glass fibers chemical composition [21].

Fibres	SiO_2 (%wt)	Al_2O_3 (%wt)	CaO (%wt)	B_2O_3 (%wt)	MgO (%wt)
E-glass	52-62	12-16	16-25	0-10	0-5
S-glass	64-66	24-25	-	-	9.5-10

To improve the compatibility of glass fibers with matrix, an important step during fibers production is sizing. Sizes can be temporary or permanent. In the first case, sizes, such as starch oils, are used to minimize the degradation of fibers as consequence of the abrasion mechanism against other fibers, to protect them from environment and to make fibers easier handled. Permanent sizes, such as silanes, are used to improve the fiber/matrix adhesion and to protect them from water exposure.

Glass fibers are usually obtained from melt spinning (Figure 2.6) [22]. In melt spinning, glass fibers are melted at about 1550 °C [23,24]. The molten glass is used to feed bushings, usually in platinum alloy, having hundreds of holes. Thus, basic glass strand is formed by drawing the molten glass though out the holes. During the forming stage, the strand is simultaneously sized by organic products dispersed in water. Finally, products can be subjected to direct roving or finishing operations like twisting for yarns, plying, texturizing, assembly of roving, chopping of strands and warping.

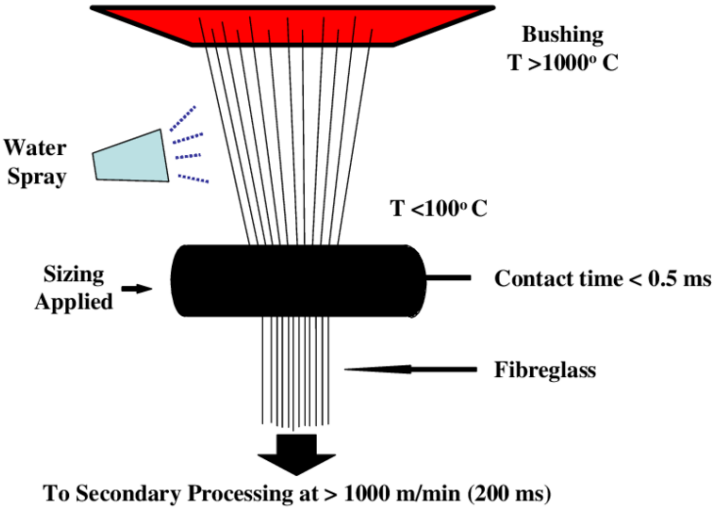

Figure 2.6 Schematization of melt spinning for the production of glass fibers [22].

2.1.1.2 Carbon fibers

Carbon fibers (CFs) are widely used as a reinforcement in composite materials because of their high specific strength and modulus [25]. Such composites have become a dominant material in the aerospace, automotive, and sporting goods industries [26-28]. The current technology for producing carbon fibers is generally based on the thermal decomposition of an organic precursor. The most important precursors are polyacrylonitrile (PAN), pitch and Rayon [29,30].

Carbon fibers can be classified into four categories according to their elastic modulus values:

- Ultra-high modulus (> 500GPa) - ex. Pitch
- High modulus (300-500 GPa) - ex. PAN
- Intermediate modulus (100-300 GPa) - ex. PAN
- Low modulus (<100 GPa) - ex. isotropic Pitch, Rayon

The production of carbon fibers from PAN is generally performed by solution spinning processes, such as the dry-spinning or the dry-jet wet spinning. Gel spinning is another variant of solution spinning

and is characterized by the use of higher molecular weight PAN and typical coagulation bath temperatures below room temperature. The obtained filaments are stretched at elevated temperatures to align the polymer chains, followed by stabilization in an oxidizing atmosphere (air) at about 200 °C, carbonization at temperatures greater than 1000 °C in inert atmosphere, and graphitization at temperature higher than 1800 °C in inert atmosphere to improve the crystallite structure and preferred orientation and therefore the tensile modulus.

On the other hand, pitch is an inhomogeneous low-molecular-weight substance (400-1000 g/mol) composed of primarily polyaromatic species. The production of carbon fibers from pitch is generally performed by melt spinning, where solid chips of pitch are fed into a heated screw extruder which provides the flow of pitch in the molten state to the metering pump and spinneret. The most convenient stabilization process is oxidation in the presence of air at temperatures of 275-350 °C. Treatment time and temperature is a function of the characteristics of pitch precursor fiber (isotropic or mesophase, filament diameter, molecular weight, etc.). Carbonization and graphitization processes are quite similar to those adopted for PAN-based carbon fibers.

Rayon is a synthetic fiber made from regenerated cellulose fiber. Rayon precursor fibers were pyrolyzed to form the first high-strength carbon fibers. However, currently less than 1% of all carbon fibers are produced this way.

A schematic view of production processes for PAN-based and pitch-based carbon fibers is reported in Figure 2.7 [31].

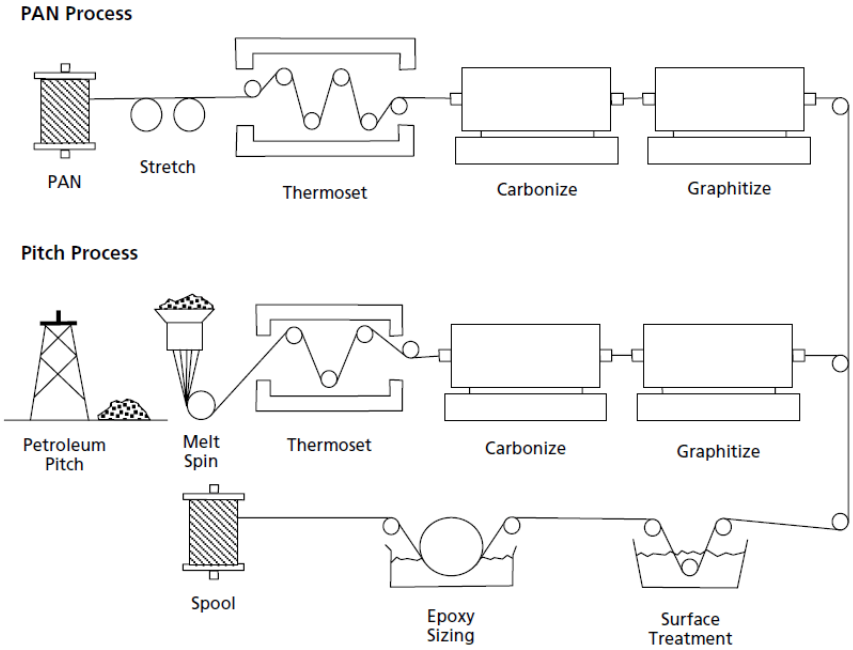

Figure 2.7 Production process of PAN-based and pitch-based carbon fibers [31].

2.1.1.3 Basalt fibers

Basalts are the most common minerals on the surface of the Earth, and are found in several geotectonic environments [32]. Safe and abundant, basalt rock has long been known for its thermal properties, strength, and durability [33]. Manufacturing processes of continuous basalt fibers (BFs) include the following key operations [34]:

- Raw material preparation
- Rock melting
- Melt homogenization and delivery to bushings
- Melt drawing through bushing units
- Drawing of elementary filaments, application of sizing agent, and winding on bobbins.

A schematic description of the process is shown in Figure 2.8 [35].

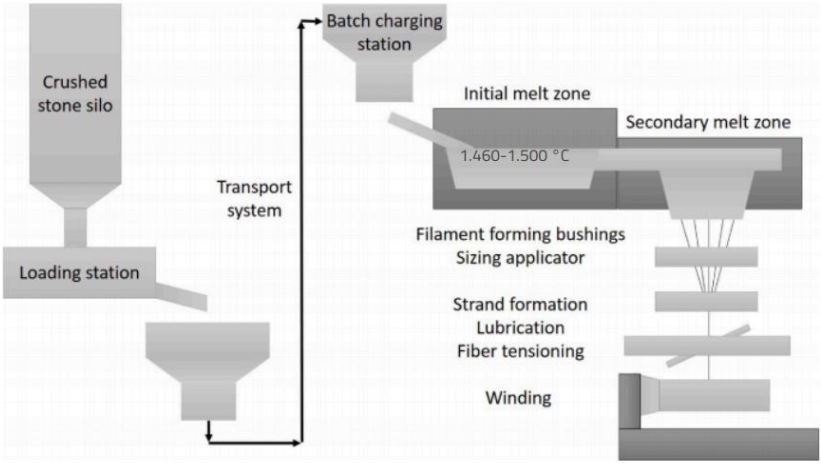

Figure 2.8 Schematic view of the manufacturing process of continuous basalt fibers [35].

2.1.2 Matrices

The role of the matrix is to hold the reinforcements, to transfer the load to them, and to protect the reinforcement from environmental impacts (i.e., water immersion, UV light, and acid/alkali solution). The matrix can be a polymeric, metallic or a ceramic material.

2.1.2.1 Polymer matrix composites (PMCs)

Polymer matrix composites (PMCs) are classified by the matrix type that can be either thermosetting and thermoplastic. Upon heating, thermosetting polymers show no melting, while thermoplastic polymers can melt and crystallize when cooled down. The different behaviour arises from the peculiar molecular structures, as shown in Figure 2.9 (a, b) [36]. In thermoplastics, the presence of no crosslinked chains allow the polymer to be melted, remoulded and recycled. On the other hand, the crosslinked molecular structure of

thermosetting prevents the sliding of chains making the polymer not meltable and recyclable.

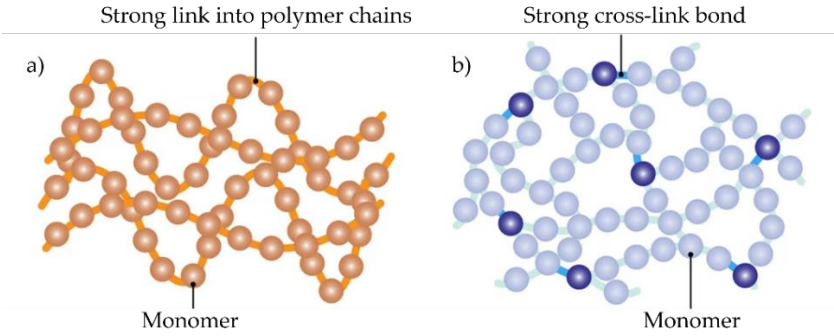

Figure 2.9 Molecular structure of (a) a thermoplastic polymer and (b) a thermosetting polymer [36].

Thermosetting resins are the most used in FRP composites since they offer great advantages, like good adhesion with other polymeric materials and reinforcements, higher service temperatures, high creep resistance and chemical resistance. For this reason, they can be used in mechanical and electrical applications.
In Table 2.3, the tensile properties of the most used matrices in fiber-reinforced polymer composites are listed [37].

Table 2.3 Tensile properties and density of matrices used in fiber-reinforced polymer (FRP) composites [37].

Material	Tensile strength (MPa)	Tensile modulus (GPa)	Elongation at break (%)	Density (g/cm³)
LDPE	40 - 78	0.1 - 9.4	90 - 800	0.91 - 0.93
HDPE	15 - 38	0.4 - 1.5	2 - 130	0.94 - 0.96
PS	25 - 69	4.0 – 5.0	1 - 3	1.04 - 10.60
Epoxy resin	35 - 100	3.0 – 6.0	1 - 6	1.10 - 1.40
Polyester	40 - 90	2.0 - 4.5	2 - 3	1.20 - 1.50
Vinyl ester	69 - 83	3.1 - 3.8	4 - 7	1.20 - 1.40

LDPE = low density polyethylene, HDPE = high-density polyethylene and PS = polystyrene

Epoxy resins (EP) are largely used in composite production due to their high chemical compatibility with glass, carbon or aramid fibers [38,39]. They possess more than one 1,2-epoxy group (Figure 2.10) per molecule, both within the chain and terminal.

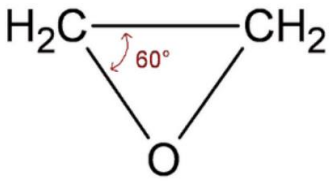

Figure 2.10 Epoxy group in epoxy resins.

The epoxy ring reacts with many substances allowing chain extension and crosslinking by rearrangement polymerisation. It exhibits lower curing shrinkage than other types of thermosetting plastics [39]. The non-epoxy part of the chain can be aliphatic, cycloaliphatic or aromatic hydrocarbon. They can be used at temperature up to 400 K and they exhibits high temperature performance. Epoxy resins finds application in printed circuit boards encapsulation, building sector, surface coating and automobile, aerospace, wind turbines [39]. Bisphenol A diglycidyl ether (DGEBA), novolac epoxy resins or aliphatic epoxy resins are mainly used. Typical properties of a fully cured epoxy resin (at 23 °C) are reported in Table 2.4 [40].

Table 2.4 Typical properties of a fully cured epoxy resin at 23°C [40].

Properties	Value	Unit
Density	1.2 - 1.3	g/cm^3
Tensile modulus	2.7 - 4.1	GPa
Tensile strength	55 – 130	MPa
Poisson's ratio	0.20 – 0.33	-
Cure shrinkage	1 – 5	%
Thermal expansion	50 – 80	10^{-6}/°C
Water absorption	0.08 – 0.15	%

Properties strongly depend on crosslinking degree that it is related to the number of the interconnected groups in the material [41]. It causes important changes in the properties of the polymeric material. Crosslinking improves resistance to thermal degradation, mechanical properties and creep resistance. Low crosslinking degree polymers show good recovery properties, while high crosslinking degree polymers show high stiffness and stability under heat and stress.

2.1.2.2 Metal matrix composites (MMCs)

Metal matrices such as aluminium (Al), magnesium (Mg), nickel (Ni), copper (Cu), lead (Pb), cobalt (Co), and titanium (Ti) and their alloys are often used in metal matrix composites (MMCs) [42]. Generally speaking, the fabrication processes MMCs can be classified into three methods, namely (i) solid-state processing, (ii) liquid-state processing, and (iii) deposition processing [43]. Solid-state processing is the most widely used since suitable for a large variety of metals, with a better control of the orientation and volume fraction of the reinforcement. However, large processing time is required. On the other hand, in a liquid-state process, the infiltration of liquid metals in fiber bundles allows to drastically reduce the processing time but the wetting of the reinforcements by the liquid metal is

usually challenging, making this method practically useless. In the deposition process, individual fibers are coated by the matrix by plasma spaying, chemical coating, electrochemical plating, chemical vapor deposition, and physical vapor deposition. In this way, the interphase and degree of interfacial bonding can be easily controlled though the amount of deposited material.
In practical applications, MMCs can be employed in aerospace applications due to their low density and high stiffness and strength [44]. They display improved performances against orbital debris, meteorites or atomic oxygen compared to polymer matrix composites.

2.1.2.3 Ceramic matrix composites (CMCs)

Conventionally, glass, silicon carbide (SiC), silicon nitride (Si_3N_4), alumina (Al_2O_3), mullite ($Al_2O_3 \cdot SiO_2$), boron nitride (BN), boron carbide (B_4C), and intermetallics (such as nikel aluminide, iron aluminide, titanium aluminide, and molybdenum disilicide) are employed as matrix to form ceramic matrix composites (CMCs) [45]. CMCs are usually processed by cold pressing and sintering, hot pressing, and chemical reaction [46]. In cold pressing and sintering, powder matrix and reinforcements are pressed at room temperature and sintered to form composites. In hot pressing, the reinforcement is added in unconsolidated matrix under high temperature and pressure levels. During this step, chemical reactions can take place between reinforcements and matrix, making the CMCs produced under chemical reaction process.
CMCs find high performance applications, such as in the aerospace sector, due to their high-temperature resistance and stability, wear and corrosion resistance [47]. For example, turbine engines, cutting tools, hot-gas filters are often made up of CMCs.

2.2 Interfacial properties in composite materials

In this section, a comprehensive review of the interphase mechanisms and interfacial properties in composites is discussed.
A key factor in determining the mechanical performances of composite is the fiber/matrix interfacial adhesion [48]. It establishes how well the matrix transfers the load to the fibers. Weak or cracked interfaces are detrimental since cause failure in the composites and reduce their properties. Moreover, they leave gases and moisture to attack the fibers [49]. However, in particular cases, also weak interface can result advantageous, for example in ceramic matrix composites. In fact, a weak interface is able to hinder the crack propagation in the brittle matrix and deflect it along the interface. In this way it is possible to improve the toughness of composites by up to five times compared to solid ceramic [50].
However, the term interface has a broader meaning, dividing this region into *interface* and *interphase*.

2.2.1 Interface and interphase

The region between matrix and reinforcements is defined in terms of interface and interphase, as shown in Figure 2.11 [11].

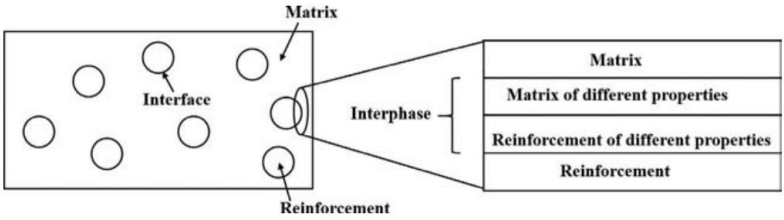

Figure 2.11 Schematic illustration of the interface and the interphase in the composites [11].

An *interface* is a sharp two-dimensional boundary between two phases. Either or both of these two phases may be solid or liquid or gaseous. On the contrary, an *interphase* is a three-dimensional

transition zone between two phases in a system. Therefore, in the specific case of fiber reinforced composites, the interphase is considered an intermediate interaction volume between bulk matrix and bulk reinforcement, where the properties can vary continuously from the reinforcement surface to some distance in the bulk matrix. It is important to underline that, as the size of the fiber (or reinforcement in general) decreases, the surface-to-volume ratio increases, making the interphase an essential concept in FRCs.

The interphase can be divided into *intrinsic* and *extrinsic* interphase [51]. It is defined intrinsic the interphase that is developed by the interaction of the polymer matrix with the reinforcement surface, while it is defined extrinsic the interphase that is developed by directly placing molecules on the reinforcement surface to achieve designed properties. For example, extrinsic interphases can be created by surface treatment of the fiber with small molecules to improve the thermodynamic compatibility with the matrix and to stabilize the fibers and filler dispersion. It is intuitive that the presence of the extrinsic interphase may alter the matrix structure and properties forming an intrinsic interphase with the reinforcement (ex., changes in crosslink density, crystallinity, density, etc.). Therefore, the extrinsic and intrinsic concepts are often interconnected.

Examples of the types of intrinsic and extrinsic interphase is depicted in Figure 2.12(a, b) [51].

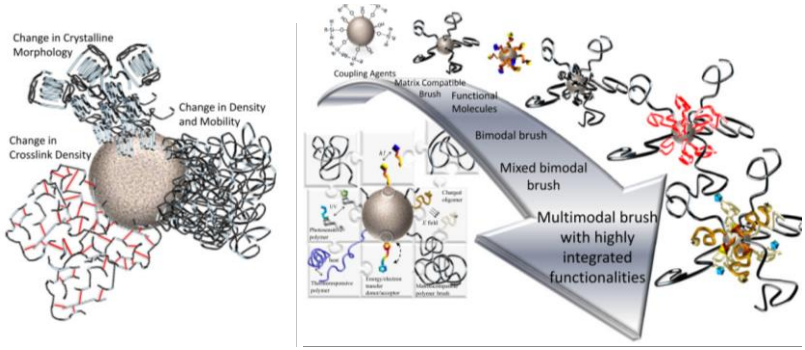

(a) (b)

Figure 2.12 Examples of the types of (a) intrinsic and (b) extrinsic interphase in composites [51].

2.2.2 Mechanisms of interfacial adhesion

Based on the theory of adhesion, the mechanisms acting at the interphase involve adsorption and wettability, interdiffusion, electrostatic attraction, chemical bonds, and mechanical adhesion [52]. Most likely, the final bonding is formed by the combination of some of these mechanisms.

- *Adsorption and wettability:* they depend on the surface energy/tension of the two surfaces in contact (matrix and fibers), by solving the forces acting along the horizontal direction (Equation 2.5),

$$\gamma_{SV} = \gamma_{LS} + \gamma_{LV} cos\theta \qquad 2.5$$

  where γ is the specific surface energy between solid/vapor (SV), liquid/solid (LS) and liquid/vapor (LV) phases. Wettability measures the ability of a liquid to spread over the surface of the material. It is possible to have good wettability when the contact θ is lower than 90°.
- *Interdiffusion: i*t involves the diffusion and entanglement of the molecules of the fibers with those of the matrix according to the thermodynamic equilibrium.

- *Electrostatic attraction: i*t involves the interaction at atomic scale between fibers and matrix since they have different electrical charges.
- *Chemical bonds:* they are formed between the chemical groups of the matrix and the fibers. Some fibers bond naturally to the matrix and other do not. Therefore, the chemical bonding can be enhanced by using coupling agents such as silane coupling agents and maleic anhydride agents. There are two main types of chemical bonds that can be formed: dissolution bonds that are short-lived bonds taking place at electronic scale; reaction bonds based on atomic transport controlled by diffusive processes.
- *Mechanical adhesion:* it depends on the degree of roughness of the fiber surface that can be either natural or etched, and by the different thermal expansion coefficients of the matrix and the fibers.

2.2.3 Failure modes of composites

Failure mechanisms in fiber-reinforced composites are a function of the constituents properties, geometry, state of stress and environmental conditions. According to the failure location, three forms of composite failure can be recognized: *failure of the matrix* (I stage), *failure of the interphase* (II stage) and *failure of the reinforcement* (III stage) (Figure 2.13 [53]). They may manifest individually or simultaneously. In general, transverse fracture of the matrix is the first damage process to occur, since the matrix has lower failure strength compared to all composites constituents. Two distinct case can be recognized: (i) the matrix is ductile and the fibers are brittle; (ii) the matrix is brittle and the fibers are brittle [54].

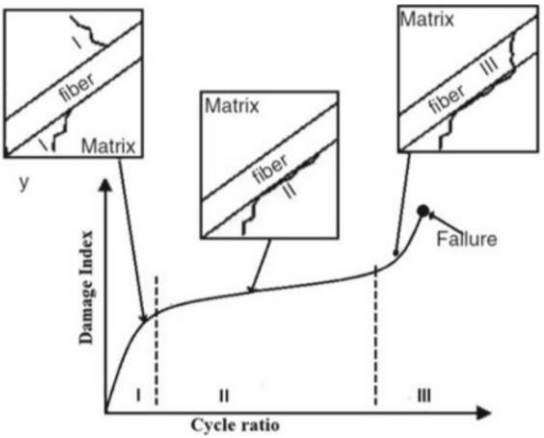

Figure 2.13 Failure steps of a composite material subjected to tension-compression cyclic loading: from failure of the matrix to failure of the reinforcement [53].

In the first case, the failure of the composite is governed by the ultimate strain of the fibers accompanied by the loss of effective fiber length. In Figure 2.14(a), the stress-strain curve of a composite is shown, while in Figure 2.14(b) the corresponding values of stress as a function of the fiber fraction is reported.

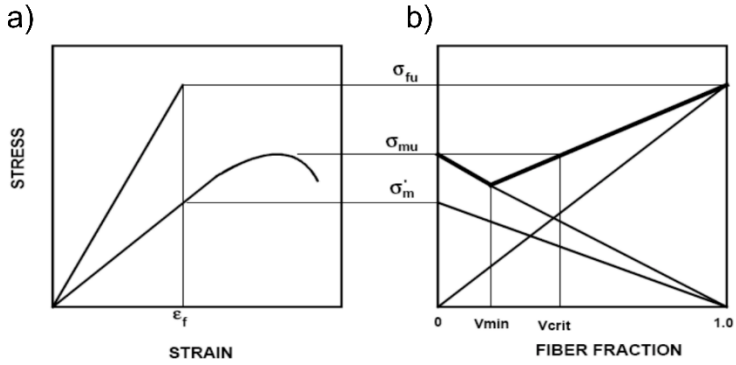

Figure 2.14 Failure of a composite made of ductile matrix and brittle fibers, (a) stress-strain curve and (b) stress-fiber volume fraction curve.

When σ_{mu}, defined as the ultimate stress of the matrix, is applied to the composite, the matrix fails, while when σ_{fu} is applied to the composites, defined as the ultimate stress of the fibers, the fibers fail. The limit in terms of deformability is given by the fibers, therefore as the deformation increases there is a point (ϵ_f) where the fibers break. When this happens, the stress that was supported by the fibers is transferred to the matrix (σ'_m), where $\sigma'_m < \sigma_{mu}$. If the fiber volume fraction (V_f) in the composite is higher than a minimum value (V_{min}), defined as the minimum amount of fibers needed to withstand the stress without the matrix to break, so that $V_f > V_{min}$, the matrix fails at σ'_m. From these values, it is possible to calculate the ultimate stress applied to the composite (σ^*_c) (Equation 2.6) by rewriting the mixture rule (Equation 2.1).

$$\sigma^*_c = \sigma_{fu} V_f + \sigma'_m (1 - V_f) \qquad 2.6$$

If $V_f < V_{min}$, the matrix carries σ'_m. However, as the load further increases, the number of failure sites increases causing cumulative weakening of the matrix. The ultimate failure occurs at σ^*_c when the number of localized fractures is that to form a weak path for complete fracture (Equation 2.7).

$$\sigma^*_c = \sigma^*_m (1 - V_f) \quad 2.7$$

In case of brittle matrix and brittle fibers, the failure of the composite is governed by the ultimate strain of the matrix. In Figure 2.15(a), the stress-strain curve of a composite is shown, while in Figure 2.15(b) the corresponding values of stress as a function of the fiber volume fraction is reported.

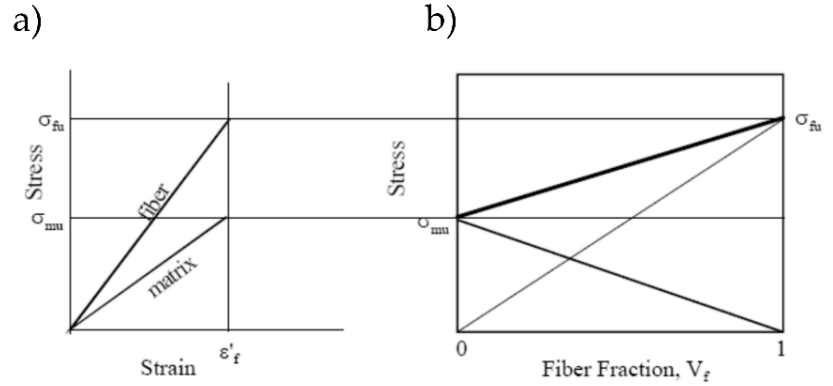

Figure 2.15 Failure of a composite made of brittle matrix and brittle fibers, a) stress-strain curve, b) stress-fiber volume fraction curve.

If $V_f < V_{min}$ and the matrix fails at σ_{mu}, the fibers are not able to withstand the load leading the composite to fail. The ultimate stress of the composites is calculated by the Mixture rule (Equation 2.1) and expressed by Equation 2.8.

$$\sigma^*_c = \sigma'_f V_f + \sigma_{mu}(1 - V_f) \quad 2.8$$

On the other hand, if $V_f > V_{min}$, the composite fail at σ^*_c, as reported in Equation 2.9.

$$\sigma^*_c = \sigma^*_f V_f \quad 2.9$$

This can only happen if between fiber and matrix there is a good interfacial adhesion to allow the stress transfer from the matrix to the fibers.

Figure 2.16 depicts a schematic description of the propagation failure of the interphase subjected to the application of the external load [11]. As the load starts to increase (segment OA), fiber and matrix are

well bonded and therefore can efficiently withstand the load. However, as the load further increases, an interfacial crack develops (point A), and propagates (point B), leading to the gradual reduction of the embedded length. At point B, the embedded length reaches a critical value and after that the interphase is fully debonded (point C). At this point, the fibers are continuously pulled out only against dynamic friction force (segment CD), namely frictional plateau

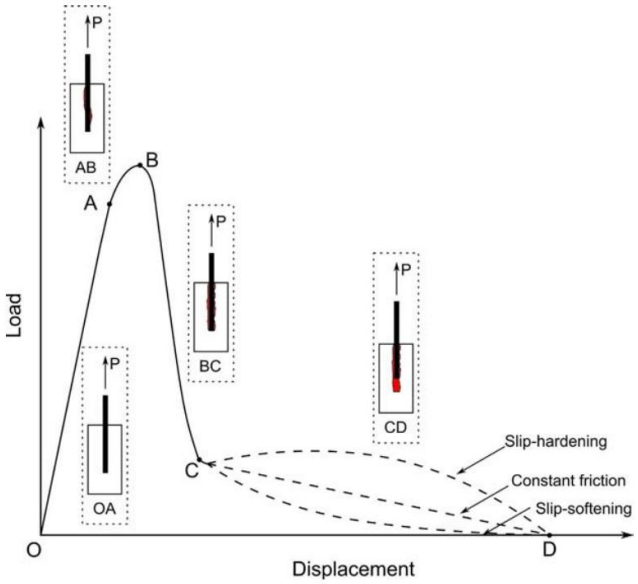

Figure 2.16 Schematic description of the failure propagation of the interphase subjected to the application of an external load, in a load-displacement curve [11].

2.2.4 Evaluation of interfacial adhesion

The interfacial shear strength (IFSS) is defined as the bonding strength acting at the interphase between matrix and reinforcement given by the ratio of maximum load (F_{max}, at point B of Figure 2.16) over the interfacial surface (A), which is also named as embedded area, as reported in Equation 2.10.

$$IFSS = \frac{F_{max}}{A} \quad 2.10$$

Microbond tests have been widely used to examine the bonding strength at the interphase due to their high consistency and easy reproducibility of the experimental results. The most widely used microbond tests are summarized and described in Table 2.5 [48].

Table 2.5 Testing methods to evaluate the interfacial shear strength values of the interphase [48].

Test	Standard	Description
Single-fiber fragmentation (SF-F)	n.a.	A tensile stress is applied on the composite specimen until the fiber breaks in different points.
Single-fiber push-out (SF-PushO)	n.a.	A thin composite sample is mounted on a sample holder with a groove located below the fibers to be tested. During single-fiber push-out test, an individual fiber is loaded by a diamond indenter tip with an increasing load resulting in fiber–matrix debonding and fiber push-out.
Single fiber pull-out (SF-PullO)	n.a.	An embedded fiber is pulled out by different loads. The relationship between load and length gives the interfacial shear strength.
Microdebonding (MB)	n.a.	A very small amount of resin is dropped on a monofilament and maintained in fixed position by a microvise, while the fiber is pulled upwards till debonding.
Bundle fiber pull-out test (BF-PullO)	n.a.	It is performed by embedding a bundle of fibers into the matrix, and then a tensile force is applied to the other end of the bundle in order to pull it out from the matrix, while the force is continually monitored and recorded.

Some typical values of IFSS for different types of fibers and matrices are summarised in Table 2.6.

Table 2.6 Typical values of IFSS for different types of fibers and matrices.

Fiber	Matrix	Testing mode	IFSS (MPa)	Reference
Carbon fiber	Epoxy resin	MB	60 ± 3	[55]
	PA6	MB	26 ± 3	[56]
	HDPE	SF-PullO	4 ± 1	[57]
Glass fiber	Epoxy resin	MB	55 ± 3	[58]
	PP	MB	4 ± 1	[59]
	PS	MB	11 ± 2	[59]
	HDPE	MB	5 ± 1	[60]
	PA6	MB	28 ± 6	[60]
	PBT	MB	24 ± 6	[60]
Natural fiber				
Basalt	Epoxy resin	SF-F	35 ± 6	[61]
	PA6,6	BF-PullO	26 ± n.d.	[62]
Henequén	HDPE	SF-F	4 ± 1	[63]
Jute	Epoxy resin	MB	12 ± 1	[64]
Kenaf	Epoxy resin	MB	6 ± 1	[64]
Curaua	Epoxy resin	MB	13 ± 1	[64]
Flax	Epoxy resin	MB	12 ± 1	[64]

HDPE = high-density polyethylene, PBT = Polybutylene terephthalate, PA = polyamide, PP = Polypropilene, PS = Polystyrene

In particular, a detailed description of the microdebonding tests is discussed, since it is the main technique used in this Thesis to characterize the interfacial properties. Microdebonding tests require the preparation of sample formed by single fiber filament embedded in one or more polymer microdroplets (Figure 2.17).

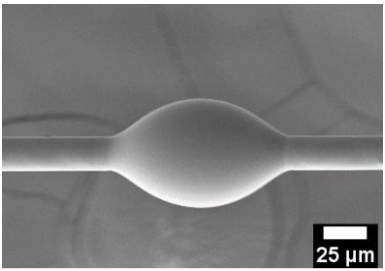

Figure 2.17 SEM image of a microcomposite for microdebonding test formed by a glass fiber embedded in an epoxy microdroplet.

The microdroplet usually has mass of some nanograms and has almost ellipsoidal shape, ranging from 30 to 200 μm of embedded length. During the samples preparation, single fibers are usually glued on a support. In case of thermosetting matrices, the polymer microdroplet is applied at liquid/viscous state by impregnating the tip of other fibers (such as carbon or flax) with the polymer. Another interesting method (which in some cases results suitable also for thermoplastic matrices) is based on the phenomena of "Fluid coating" [65] and "Rayleigh-Plateau instability" [66], explained in Section 5.1. However, the Rayleigh-Plateau instability is often disadvantageous, since causes the formation of multiple droplets from the collapse of an unstable single droplet, and this leads to a complicate post-debonding analysis of the frictional plateau, since the presence of close-range droplets may interfere each other preventing their sliding along the fiber (Figure 2.18). In fact, the frictional plateau (Figure 2.16) is important since provides indications about the roughness and other morphological aspects of fiber surface [67].

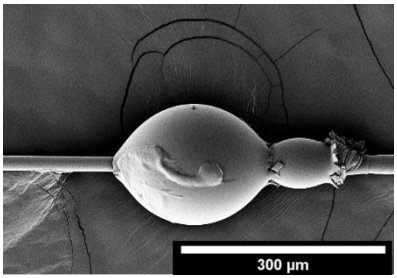

Figure 2.18 SEM image of interference between two consecutive microdroplets.

In case of thermosets, thermal curing is needed after deposition. It has been seen that the IFSS is function of the curing time, by showing an increase in the early stages of curing and then reaching a plateau for further duration of curing [68]. The resulting post-curing morphology of droplets have an absolute importance on the final micromechanics properties. As it can be seen in Figure 2.19(a,b), the presence of microdamages on the microdroplet (Figure 2.19a) and/or the not regularity of its shape (Figure 2.19b) implicate an anticipated debonding due to droplet failure or inadequate stress distribution along the interface, therefore underestimating the actual interfacial adhesion properties.

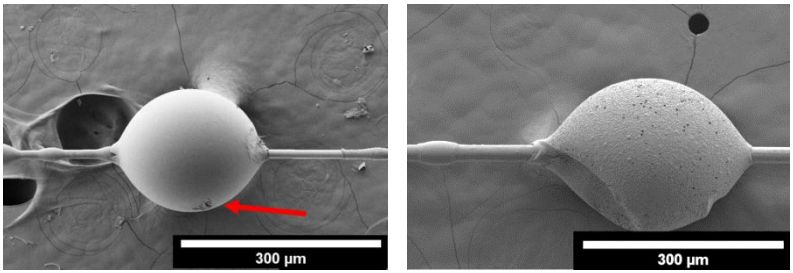

(a) (b)

Figure 2.19 SEM images of (a) microdamaged epoxy droplet, and (b) irregularly shaped epoxy microdroplet.

After sample preparation, the microcomposites are tested under shear stress: the microdroplet is constrained by a microvise while the fiber is pulled at a constant rate, or the contrary (Figure 2.20). Usually, the pulling rate ranges from 5 μm/min to 1 mm/min, depending on the type of fiber/matrix system analyzed. While testing, the shear load applied is measured up to interface failure, as depicted in Figure 2.16 [48], and divided for the embedded area (Equation 2.10). The dimension of fiber and droplets are usually measured optically.

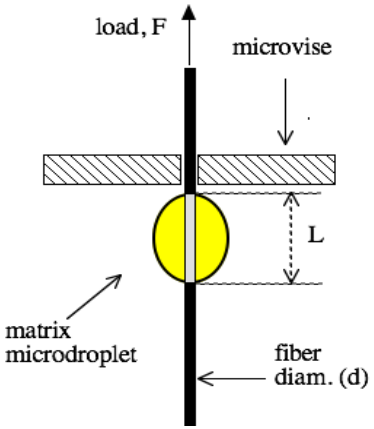

Figure 2.20 Example of a microdebonding test: the microdroplet is constrained in fixed position and subjected to shear stress while the fiber is pulled at constant rate [48].

As for microbond tests, the IFSS is calculated as reported in Equation 2.10. However there is a problem in this equation, since it only takes into account the interfacial properties without considering several other parameters that influence calculation of adhesion, such as the wide range of embedded lengths, the thermal-oxidative degradation of the matrix resin, the thermal interfacial residual stresses, and the compliance of the instrumentation (i.e. the blades), as explained by Cai et al. [42]. Therefore, an alternative method is the calculation of

the apparent IFSS ($IFSS_{app}$), described as the slope of the linear regression line that relates the maximum force (F_{max}) of multiple individual droplets to their embedded area (A) (Equation 2.11).

$$F_{max} = IFSS_{app} \cdot A + q \qquad 2.11$$

The slope corresponds to the apparent IFSS value, calculated in MPa, while the intercept q represents the influence of all the listed experimental factors which influence the actual IFSS value. Moreover the R^2 values, i.e. the goodness-of-fit for linear regression models, also provides the indication of the consistency of interfacial properties throughout the entire fiber length tested. An example is reported in Figure 2.21 [69].

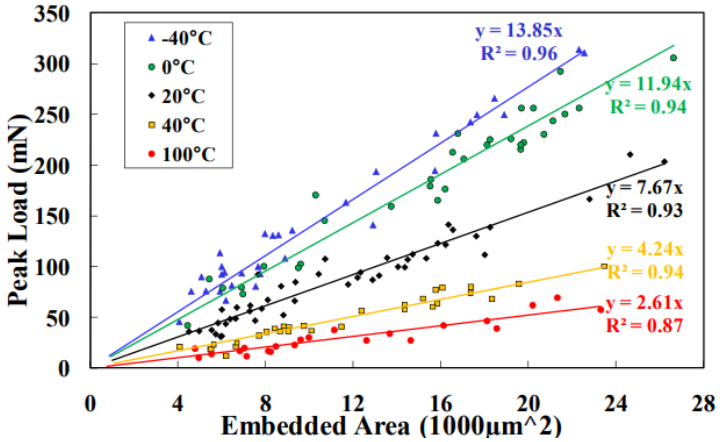

Figure 2.21 Microbond peak load (F_{max}) versus embedded area for a glass fibre/polypropylene at various test temperatures. The equation of the linear regression fits are reported from which the apparent IFSS values can be obtained [69].

2.2.5 Methods for interfacial characterization

Along with micromechanics, the microstructural characterization of the interfacial region is of crucial importance to explain and/or predict interfacial debonding. In this sense, scanning electron

microscopy (SEM), atomic force microscopy (AFM), optical projection tomography (OPT), Raman spectroscopy, X-ray tomography, transmission electron microscopy (TEM), etc., are useful techniques.

In particular, scanning electron microscopy (SEM) is an advanced type of electron microscopy, which allows to obtain highly detailed images of the fiber/matrix contact region. The surface of the sample is scanned with a tightly focused beam of electrons that interacts with the atoms in the specimen, generating signals that carry the information about the surface morphology. Though SEM, it is possible to observe qualitatively the morphological aspects of the fiber surface and of the matrix microdroplet, which determines in the adhesion bonding between the constituents and the potential defects. Samples are usually sputtered before being analyzed by a thin layer of conductive platinum/palladium or gold, to make them electrically conductive. An example of SEM images is reported in Figure 2.22(a, b).

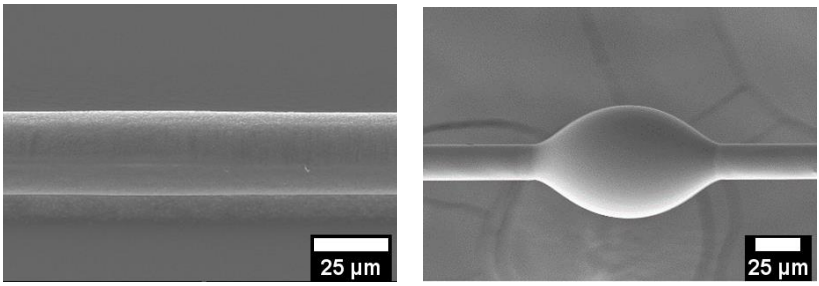

(a) (b)

Figure 2.22 Examples of SEM images, (a) glass fiber surface and (b) a microcomposite.

Atomic force microscopy (AFM) is a surface topography technique, usually used to analyze surfaces and coatings. A sharp tip scans the surface of the samples to obtain high-resolution nanoscale images of local sites, and provides qualitative and quantitative information on

surface morphology, surface texture and roughness. It gives the indication of the surface properties of the fibers in contact with the matrix, therefore providing information about the mechanical component of adhesion. An example of AFM image is reported in Figure 2.23.

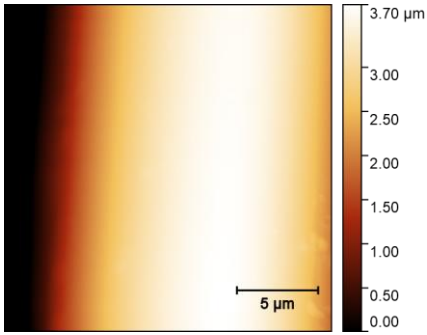

Figure 2.23 Example of glass fiber surface analyzed by AFM technique.

Optical projection tomography (OPT) is a form of tomography involving optical microscopy. Tomography is the imaging of surface section while the sample is rotating and subjected to a light source. A camera records multiple images during this rotation, which are stacked to obtain a 3D accurate reconstruction of the sample. This technique allows to obtain important information about the cross-sectional shape of the fibers in microcomposites, which is of crucial importance in the estimation of the embedded area for the calculation of the IFSS. In fact, in synthetic fibers (carbon, glass, or polymer fibres) the cross-sections can be measured from a single projection, since retains almost constant shape of the cross-section. On the other hand, natural fibres, i.e. pulp and flax fibers, have constant variation in their cross-section, making of paramount importance its punctual control. An example of OPT image is reported in Figure 2.24 [70].

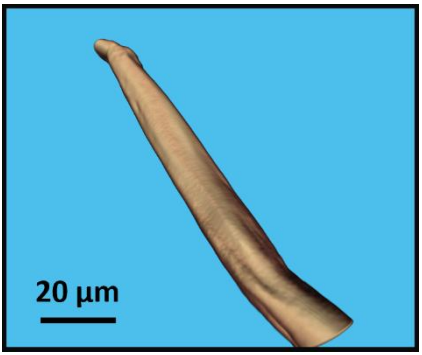

Figure 2.24 Surface of pulp fiber from 3D OPT reconstruction [70].

2.2.6 Techniques to improve the interfacial properties

The methods to improve the interfacial properties in composites can be divided into two categories: *reinforcement surface treatment* and *matrix structure modification*.

2.2.6.1 Reinforcement surface treatment

In fiber-reinforced polymer composites, "wet", "dry" and "multi-scales" treatments are applied to modify the fiber surface for a better interfacial bonding between fibers and matrix, without influencing their mechanical properties [71].

- *"Wet" chemical methods:* Chemical treatments include alkali, acetyl, silane, acrylic acid and enzyme treatments, which corrode the fiber surface and/or introduce functional groups, increase surface polarity and roughness, in order to improve fiber/matrix interlocking. These treatments effectively improve interfacial properties, however they can also compromise the single fiber strength. Moreover, these treatments have a negative environmental impact for the disposal of the chemicals. Another effective method to improve fiber/matrix adhesion is by the use of polymeric sizing/coatings on the fiber surface. In fact, the presence of an interphase with a molecular gradient (an extended

region, where two adjacent components are mixed) can promote adhesion and compatibility at the composite interface. Sizing is a method used to protect the brittle fibers from damage, to provide suitable strand integrity, to improve fiber/sizing/matrix adhesion and to improve composite processibility. Most of the commercially available sizes are compatible to epoxy. Some of them are silane coupling agents, polyurethanes and/or epoxy film formers. Also thermoplastic polymers are used as polymeric coatings to enhance cohesion through massive entanglements. Some of them are poly(vinyl alcohol) (PVA), polycaprolactone (PCL), ethylene vinyl acetate (EVA), poly (methyl methacrylate) (PMMA). Both coating and sizing can be achieved using techniques such as aqueous/solution dip coating, polymer grafting, electro-polymerization, sol-gel technique. However, it has been seen that the thickness of the sizing/coating plays a negative effect on the interfacial shear strength [72]. In fact, the higher the thickness, the lower the IFSS. The thickness can be measured by SEM, AFM thermogravimetric analysis (TGA).

- *"Dry" surface modifications:* the plasma treatment improves the fiber/matrix adhesion due to the inclusion of different functional groups (i.e., hydroxyl, ether, carbonyl, etc.) on the fibers surface to improve the surface reactivity and adhesion potential, and surface wettability with hydrophilic polymer matrix. High energy irradiation (HEI) is used to modify the fiber surface and is an efficient and environmental friendly technique, which improves fiber/matrix adhesion without deteriorating the strength. Examples as electron beams, X-rays, ultraviolet light radiation, and CO_2 laser emission, are some of the most used HEI methods.
- *Surface modification in "multi-scales":* the nanomaterial coating of fiber surface is a powerful method to increase the surface area, therefore to promote mechanical interlocking and local

stiffening of fiber/matrix interface, which imparts the strength to the interface by enhancing stress transfer from matrix to the fibers. The main challenge is the homogenous distribution of the nanomaterial on the fiber surface. Surface roughening is also beneficial for toughening. In fact, the crack developed at the interphase is forced to follow a zig-zag route since the nanofiller hinders its propagation. The higher the aspect ratio of the filler, the higher the crack deviation efficiency. For example, a multi-scale coating on CF consists of nano-particles/carbon nano-tubes/graphene coating obtained using techniques such as electrophoretic deposition (EPD), chemical vapor deposition (CVD), and dip coating.

2.2.6.2 Matrix structure modification

The matrix composition and microstructure can strongly influence the fiber/matrix interphase and thus the performances of the corresponding composites. Matrix modification is usually achieved by nanofillers dispersion in the matrix and possible nano-structuring within the matrix [48].

- *Nanofillers in the bulk matrix: t*he matrix modifications can be achieved by adding 0D (spherical), 1D (i.e. CNT) and 2D (i.e. clay, graphene) nanofillers. The enrichment of the nanofillers in the interphase allows the reaction of the fillers reactive groups with those of the bulk matrix and the silane sizing of the fibers. For example, Hossain et al. [73] investigated the addition of CNTs and graphene nanoplates in CF/EP composites, obtaining an improvement in the interlaminar adhesion of 15%.
- *Bulk matrix structuring:* in case of thermoplastics and thermosets, the idea is to create a bi-continuous structure. The bi-continuous structure is achieved in the early stage of mixing, then can be preserved using nanofillers as "phase stabilizers". The key point of this type of structure is that it

allows to create different functionalized patterns that are periodically repeated along the fiber length, relieving local stress concentrations at the interphase. Czigany et al. [74] showed that an interpenetrating network (IPN) structure of vinyl ester/epoxy resin matrix combined with basalt fibers strongly improved the interfacial adhesion and therefore the mechanical performance of the composite.

2.3 Multifunctional composites

Fiber-reinforced composites, beside their structural role, can be utilized for exploiting other functions. When the structural and secondary functions are merged, multifunctional materials are created. For example, a multifunctional composite has high strength, high stiffness, high fracture toughness and high damping capability. Or, it can have load-bearing, noise and vibration control, self-healing, thermal insulation, and energy harvesting/storage capability.

From the interfacial point of view, some treatments and modifications of the interphase region have been coupled to achieve multifunctionality in composites. The extrinsic interphase offers a powerful way to alter the electrical, optical, dielectric, mechanical, degradation, and biological properties of composites. In this sense, some examples include the deposition on the fibers of electrical conductive nanofillers (such as graphene oxide (GO) nanoplates, single-wall (SWCNT) or multi-wall (MWCNT) carbon nanotubes) or the grafting and the deposition of polymeric chains.

2.3.1 Sensing /damage detection

The most widely used composites are made by polymeric matrices, which are typically poor electrical conductors. As an example, in aircraft structures, structural composites should possess electrical conductivity to monitor the health condition of the component during the flight, as a valid alternative to metallic parts. On the other

hand, enhanced thermal conductivity of composites is important for cooling of electronic circuits and propulsion systems. Therefore, the use of a very small concentration of conductive fillers in the interphase region lead to large improvements in the electrical/thermal conductivity of FRC [68,69]. For example, the formation of networks of graphene oxide (GO), or carbon nanotubes (CNT), or carbon nanofibers (CNF) allows in situ sensing of deformation and damage. In this sense, Mahmood et al. [75] used reduced graphene oxide (rGO) coated glass fibers embedded in an epoxy matrix to enhance the electrical resistance of the composite subjected to an applied strain.

2.3.2 Self-healing composites

The detection of damages in composite can be often a problem, in particular for those internal where it is not possible to detect properly the onset of the damage. In this sense, the development of self-healing materials, able to self-repair autonomously or under the application of a stimulus, could be an interesting approach. The development in the field started by the bulk modification of polymer, prior to focus on interphases. However, as already empathised, the interphase is most often the weakest region in the composites, demanding self-healing properties preferentially located between matrix and fibers. Two distinct self-healing systems can be recognized: (i) *capsule based self-healing systems*, and (ii) *reversible self-healing systems.*

2.3.2.1 Capsule based self-healing systems

In these systems, the healing agent is constrained in discrete structures, such as microcapsules, hollow fibers and vascular networks. Its release occurs when the capsules break because of the damage and/or the crack growth. Typically, the healing agent is in liquid state to facilitate the capillary flow of the agents into the crack, where it solidifies in the presence (or not) of a catalyst. Examples of

healing agents are monomers, dyes, and hardeners. As the process does not need a manual or external intervention, it is autonomic. However, once the capture is broken and the healing agent is released, no more healing cycles can be performed. This is the major drawback of extrinsic over intrinsic self-healing systems, that instead allow for multiple healing cycles.

- *Microcapsules:* a microcapsule is made by the core and the shell. It can have spherical or irregular shape and may vary in size from nano- to microscale. The healing agent and/or the catalyst are contained in the capsule and released once needed. Jones et al. [76] coated the glass fibers with microencapsulated epoxy resin and ethyl phenylacetate (EPA) solvent to obtain a full recovery of fiber/matrix interfacial strength evaluated by microdebonding tests.
- *Hollow fibers:* hollow fibers are nano- or microstructures containing the healing agent, usually an uncured resin and/or an hardener. The advantages of the use of hollow fibers over microcapsules are: (i) higher volume of healing agent is available to repair damage; (ii) different activation methods/types of resin can be used; (iii) hollow fibers can easily be mixed and tailored with the conventional reinforcing fibers. However, there are also several disadvantages: (i) fibers must be broken to release the healing agent; (ii) low-viscosity resin must be used to facilitate fiber infiltration; (iii) use of hollow glass fibers in carbon fiber-reinforced composites will lead to coefficient of thermal expansion (CTE) mismatch, multistep fabrication is thus required. For example, Bleay et al. [77] studied the effect of the addition of hollow glass fibers in an epoxy FRP, demonstrating a 5% healing efficiency upon vacuum-assisted heating.
- *Vascular networks:* in vascular networks, a 3D network is employed to distribute the healing agent in a continuous pathway. However, the fabrication process is very complex,

making these system used only in very specific applications. For example, Norris et al. [78] incorporated a vascular network in carbon fiber-reinforced laminates and activated the healing mechanism by epoxy resin infusion through the network, followed by curing. A 95% healing efficiency was observed.

2.3.2.2 Reversible self-healing systems

In these systems, the healing agent is not confined and the material itself possesses the ability to self-heal, triggered by heat or another physical stimulus (i.e., electrical voltage, magnetic field, etc.).

- *Diels-Alder (DA) and Retro-DA reactions:* DA reactions are thermally reversible chemical reactions, used as crosslinking mechanism in mendable polymers, and involve the reaction between maleimide and furan moieties. In the particular case of self-healing interphases, the basic idea is to add one of the required functional groups onto the fiber surface, and the counterpart groups are added in the matrix. For example, Zhang et al. [79] grafted maleimide groups onto CF embedded in a furan-containing epoxy resin. 82% healing efficiency was obtained by microdebonding tests.
- *Ionomers:* ionomers are polymeric materials that contain a hydrocarbon backbone and pendent acid groups, that are partially or fully neutralized to form salts. Ionomers can be synthetized from the copolymerization of a low-level functionalized monomer with an olefinic unsaturated monomer, or by the post-functionalization of a saturated preformed polymer. The introduction of a small amount of ionic group in polymer composites causes dramatic improvement of the tensile strength, tear resistance, impact strength, and abrasion resistance. They can be processed like thermoplastics, and they are used in food packaging, automobile parts, coatings, etc. The reversible nature of the

ionic bonds make them good candidates for self-healing applications.

- *Supramolecular polymers: s*upramolecular polymers involve the reversible noncovalent assembly of low molar mass monomers, that show therefore self-healing capabilities. Hydrogen bonds is the most popular route to design supramolecular polymers. The main challenge is to balance assembly and reversible capacity. The higher the assembly, the lower is the reversibility of interaction. Hayes et al. dissolved different concentrations of thermoplastic (poly bisphenol-A-co-epichlorohydrin) into epoxy resin, showing a recovery in Charpy impact energy of 50% upon thermal healing.
- *Molecular diffusion with entanglements:* interdiffusion of molecular chains to form interphase regions is the simplest way to weld polymeric materials, and therefore it is important for self-healing. This can happen either within one polymer or between two polymers. When the chain ends entangle, they promote adhesion strength. The process is divided in four stages, as depicted in Figure 2.25: (i) rearrangement and surface approach, (ii) wetting of the surfaces, (iii) low level diffusion between surfaces, (iv) diffusion equilibration and randomisation [80]. As more chains cross the interface, the entanglement density at the interfacial zone increases, and thus the interphase becomes strengthened. Since entanglement is time-dependent, after a critical time (τ_c) the two layers completely merge into one. For example, Zhang et al [80] studied the diffusion process of poly (vinylidene fluoride) (PVDF) and poly (methyl methacrylate) (PMMA), that formed a functionalized time-dependent interphase.

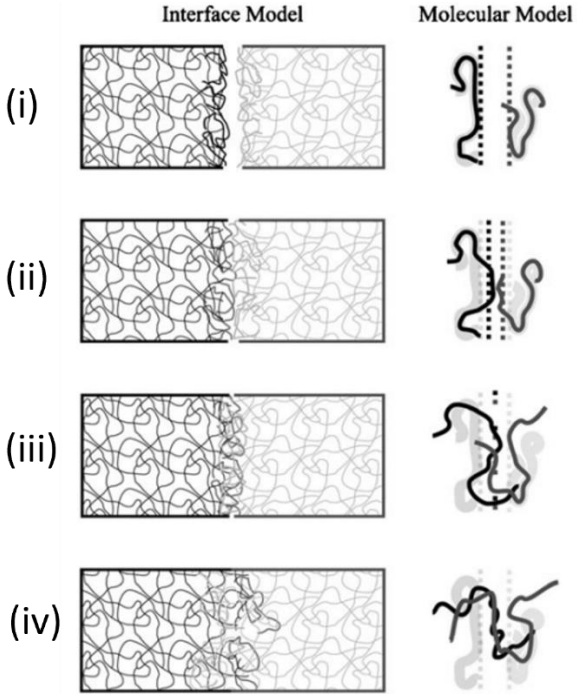

Figure 2.25 Scheme of the healing process across a polymer interface via molecular inter-diffusion [81].

- *Melting of a thermoplastic phase:* this concept is strictly related to molecular diffusion and entanglement. Upon heating, a low melting thermoplastic material mobilizes and diffuses forming an entangled interphase. Upon removal of the heat, it solidifies providing the heal. Experimental results regarding healing conditions revealed that polymers generally heal at atmospheric pressure or under vacuum, with a range of temperature from −50 to +100 °C, and time from minutes to years [82]. However, in some thermoplastic polymers like PMMA, the glass transition temperature (T_g)is relatively high (above 100 °C) and high temperature is required for the initiation of self-healing. This limitation can

be overcome by mixing the polymer with a substance that has a plasticizing effect on the polymer [83].

2.3.2.3 Evaluation of the self-healing

To quantify the recovery of a property upon damage of the interphase, the healing efficiency (HE) can be estimated following Equation 2.12, where F is the property of interest.

$$HE = \frac{F_{healed} - F_{damaged}}{F_{virgin} - F_{damaged}} \quad 2.12$$

$F_{damaged}$ is the property in the damage state, that is often set to zero. F_{virgin} is the property in the virgin state, i.e. of the unhealed material. F_{healed} is the property in the healed state, and in some situations, it can be higher than that of the virgin property, since crack-healing systems can produce an interface of a new material, which may perform better than the original one.

2.3.3 Other multifunctional properties

Vibration damping is of great interest in composites materials. Vibration energy can be dissipated via frictional interaction, therefore vibration damping capability can be provided at fiber/matrix interfacial level improving the frictional contributions of the interphase. For example, the fibers can be coated with highly viscoelastic polymers and with nanofillers. In fact, stick-slip contributions given by CNT-CNT interactions and CNT-matrix may contribute to energy dissipation [84].

2.4 From microscale to macroscale composites

A final consideration is dedicated to how a microcomposite can be representative of a macrocomposite. It has been observed that the physical and mechanical properties of microdroplets can differ significantly from those of the bulk material, and this is especially true for epoxide droplets. The main discrepancy between micro and macroscale is related to the thermal characteristics of epoxy. Curing is of paramount importance since determines the degree of cross-

linking and the residual stresses acting at the interface. Therefore, an efficient cure cycle must be carefully selected while preparing microcomposites. It has been seen that the microdroplets show T_g values up to 50 °C lower than the bulk materials, by considering droplets ranging between 100 μm and 800 μm of length, as found by Rao et al. [85]. Under 100 μm, T_g is not subjected to further reductions. The loss of T_g is attributed to the lack in the stoichiometry caused by the vaporization of the volatile components in the hardener during the early stages of the curing cycles. This phenomenon is more evident as the surface-to-volume ratio of droplet increases. The lack of stoichiometry does not influence only the T_g values, but also affects the tensile and shear modulus, the Poisson's ratio and thermal expansion coefficient [86]. Droplet has been observed to have higher Young's modulus than the bulk material. This is of great importance since influences the stress distribution at the interphase, therefore affects the estimation of the IFSS. Therefore, simulations and models are needed to predict the adhesion properties, given these discrepancies. By modelling the interface at microscale using the properties of a bulk material, Zinck et al. [86] have observed an underestimation up to 80% of the interfacial properties compared to a real microcomposites. Regardless the residual stresses, Wagner et al. [87] modelled the compressive stresses induced by the matrix during the cooling stage on the fibers of microcomposites. They observed a notable difference of one order of magnitude in the stress acting around a single fiber in a macrocomposite (a few tenths of MPa) and in microcomposites (12 GPa). This indicates that the compressive stresses have a more significant impact on the adhesion values in microcomposites than in macrocomposites.

Additionally, another consideration is related to the strain rate in testing. In microdebonding, the strain rate might be significantly lower than that used to test macrocomposites. It has been seen by Gaur et al. [88] that varying the strain rate of two orders of magnitude, a slight increase (< 10%) in the average IFSS was found,

while Zinck et al. [86] showed a drastic influence of the loading rate. Possibly, there is a change in the fracture behaviour with the strain rate, passing from a more ductile (using 0.05 mm/min) to a completely brittle fracture of the interface (using 1 mm/min).

On the other hand, a robust understanding of the interfacial adhesion properties in macrocomposites is highly affected and hindered by several other defects in the bulk structure, primary accounting for matrix failure, fiber failure, interlaminar and intralaminar failures, delamination, etc. These defects alter the stress state in the material either anticipating or preventing debonding.

Therefore, all of these aspects highlight the noticeable importance of micromechanics (and in particular of microdebonding tests) in the definition of the matrix/fiber interfacial properties. It is evident that the interfacial micromechanics is a complex representation of the interfacial macromechanics, and unfortunately this correlation still remains not completely understood.

3 Experimental part

Chapter 3 – Experimental part introduces the matrices, the fibers and the materials employed to coat the fiber surface, and describes the main characterization techniques used to investigate the prepared samples. The procedures adopted for sample preparation are, instead, described in Chapter 4 and Chapter 5.

3.1 Materials

In this section, all the materials employed in the Thesis are listed, divided in *matrix*, *fibers* and *coating materials*. Thermosetting polymer matrices where utilized, combined with fibrous reinforcements such as glass, basalt, and carbon fibers. Materials like graphene oxide and polycaprolactone were used to coat the fibers surface.

3.1.1 Matrix

Two sets of bicomponent epoxy matrices (EP-1 and EP-2) were employed in the fabrication of thermosetting composites. Both systems were constituted by a base (B) and a hardener (H). EP-1 consisted of an epoxy base (EC 157) and an hardener (W 342), and EP-2 consisted of an epoxy base (EC 141 NF) and an hardener (W 242 NF). Both systems were provided by Elantas Italia S.r.l. (Colecchio, Italy). In EP-1, base and hardener were mixed at a weight ratio 100:30, in EP-2 base and hardener were mixed at a weight ratio 100:45. The specific properties of base and hardener for the both systems obtained from datasheets of the producer are reported in Table 3.1.

Table 3.1 Properties of base and hardener of EP-1 and EP-2 utilized in this thesis.

		Code	Viscosity (mPa·s)	Density (g/ml)
EP-1	B	EC 157	600 – 800	1.14 -1.16
	H	W 342	30 – 70	0.94 – 0.96
EP-2	B	EC 141 NF	650 – 950	1.10 – 1.14
	H	W 242 NF	250 - 350	0.98 – 1.02

The recommended curing cycle for EP-1 was 24 h at 25 °C + 15 h at 60 °C, while for EP-2 was 15 h at 60 °C.

Quasi static tensile tests were performed on 1BA dumbbell specimens of cured epoxy resin (ISO 527) using an INSTRON 5969 (Instron, Norwood, USA) universal tensile tester equipped with loading cell of 10 kN, as shown in Figure 3.1(a,b). The elastic modulus was evaluated in tensile mode as a secant value between deformation levels of 0.05% and 0.25%, at crosshead speed of 0.25 mm/min with a maximum axial deformation level of 1%. The strain was recorded by using a resistance extensometer Instron model 2620-601 (gage length of 12.5 mm). Ultimate tensile properties were evaluated at a crosshead speed of 1 mm/min, without using the extensometer. At least five specimens were tested for each sample

.

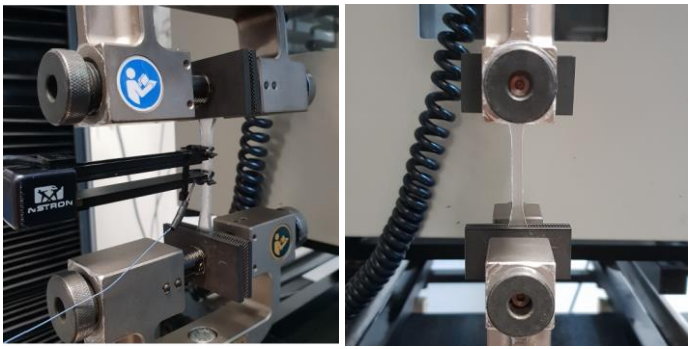

(a) (b)

Figure 3.1 Quasi static tensile test setup: with the use of the extensometer (a), without the use of the extensometer (b).

Thermal degradation (T_{max}) of cured epoxy was evaluated through thermogravimetric analysis (TGA) by using a Mettler TG50 thermobalance (Mettler Toledo, Columbus, OH). Nitrogen gas was used with constant flux of 100 mL/min. Heating was performed from 35 to 700 °C at 10 °C/min. Differential scanning calorimetry (DSC) test was carried out by Mettler DSC30 calorimeter (Mettler Toledo, Columbus, OH) to determine the glass transition temperature (T_g) at first heating scan. A heating scan of 0/150°C was performed in a nitrogen environment with constant flux equal to 100 mL/min at 10 °C/min. The mechanical and thermal properties of cured epoxy systems are summarized in Table 3.2.

Table 3.2 Mechanical and thermal properties of EP-1 and EP-2 utilized in this thesis.

	Elastic Modulus (GPa)	Tensile strength (MPa)	Strain at break (%)	T_g (°C)	T_{max} (°C)
EP-1	2.8 ± 0.5	38 ± 2	2 ± 1	80	366
EP-2	3.5 ± 0.4	44 ± 3	11 ± 1	55	357

3.1.2 Fibers

Various types of fibers were employed to prepared structural composite materials. Glass fibers (GFs), basalt fibers (BFs), and carbon fibers (CFs) were selected since commonly used to fabricate composites, due to their high tensile strength and stiffness, and excellent resistance to temperature and chemical corrosion. Glass fibers were used both silane sized (sGF) and unsized (uGF). The properties of the employed fibers taken from the datasheets are summarized in Table 3.3.

Table 3.3 Properties of glass, carbon and basalt fibers utilized in this thesis.

	Producer	Form	Type	Density (g/cm^3)	Mean diam. (μm)	Sizing
Glass fibers						
PPG 2001	PPG Industries Inc.	Strand	E	2.50	24	silane
Windstrand® (sGF)	Owens Corning Inc.	Strand	E	2.30	18	silane
Windstrand® (uGF)	Owens Corning Inc.	Strand	E	2.30	18	unsiz.
Carbon fibers						
GV 201 U TFX	Angeloni Srl.	Fabric	PAN	1.71	8	PU
Basalt fibers						
BAS 220 P	Basaltex Nv	Fabric	-	2.67	15	silane

*PU = polyurethane

The mechanical properties of the fibers were evaluated by single fibre tensile tests, which were carried out on single fiber filaments by using an Instron 4502 tensile machine (Instron, Norwood, USA) equipped with a 100 N load cell for GFs and BFs and 1 kN for CFs. The fiber were attached on paper tabs by glue, as schematically reported in Figure 3.2a at gauge length of 15, 30 and 60 mm. At least ten specimens were tested. Single fibers filament testing setup is reported in Figure 3.2b.

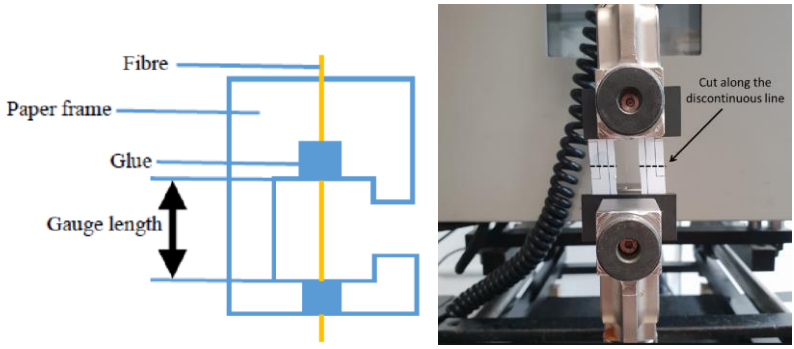

(a) (b)

Figure 3.2 Schematic pictures of: (a) single fiber glued on the paper tab and (b) single fibers filament testing setup.

Tests were performed according to ASTM C1557 standard using a constant displacement rate of 0.05 mm/min. The results from this test allowed to determine the shape (m) and the scale (σ_0) parameters of the Weibull distribution by using an iterative approach [89]. The Weibull distribution (Equation 3.1) is commonly used to describe the continuous failure probability of brittle fibres ($F(\sigma)$), for a given fibre length (L) and a reference fibre length (L_0).

$$F(\sigma) = 1 - \exp\left(\frac{s}{\sigma_0}\right)^m \quad 3.1$$

The reduced stress (s) is expressed by Equation 3.2.

$$s = \sigma \cdot k^{1/m} \quad 3.2$$

Where k is the ratio between lengths, as expressed by Equation 3.3.

$$k = \frac{L}{L_0} \quad 3.3$$

The Weibull distribution is linearised (Equation 3.4) to obtain the scale parameters, as shown in Equation 3.5 (where q is the intercept of the linearised curve), and the shape parameters.

$$ln\{-ln[1 - F_i]\} = m\, ln(s_i) - m\, ln\sigma_0 \quad 3.4$$

$$\sigma_0 = \exp\left(\frac{q}{m}\right) \quad 3.5$$

It should be noted that F(σ) is the probability of the failure of each fibre and is calculated as shown in Equation 3.6, where "i" is the indicator of the stress at the break value of each specimen and N is the total number of specimens [90,91].

$$F_i = \frac{i-0.5}{N} \quad 3.6$$

Since the shape parameter is unknown, the following iterative approach can be used:

a) an initial tentative m value is chosen;
b) values of s_i, i = 1, …, N are calculated taking into account the size (L) of each specimen;
c) parameters σ_0 and m' are calculated using the conventional Weibull distribution method;
d) if the difference $\frac{|m-m'|}{m} < 0.01$ the convergence process is assumed to be completed. Otherwise, the iterative process is continued by returning to step (b) with m = m'.

Furthermore, since three different fibre lengths were tested, as indicated in the standard ASTM C1557, the Young's modulus (E) of the fibres was estimated from Equation 3.7 [89]:

$$\frac{\Delta L}{F} = \frac{l_0}{EA} + C_s \quad 3.7$$

The plot of (ΔL/F), which is the inverse of the slope of the force versus cross-head displacement curves, versus (l_0/A) yields a straight line with constant slope of (1/E) and intercepts (Cs) that is the value of the system compliance.

The mechanical properties of the fibers are listed in Table 3.4.

Table 3.4 Mechanical properties of fibers utilized in this thesis.

	E (GPa)	σ_0 (MPa)	m
Glass fibers			
PPG 2001	75 ± 3	2188 ± 211	2.5
Windstrand®(sGF)	72 ± 1	1974 ± 168	3.6
Windstrand® (uGF)	69 ± 5	1944 ± 116	3.3
Carbon fibers			
GV 201 U TFX	312 ± 32	3220 ± 49	4.6
Basalt fibers			
BAS 220 P	74 ± 9	2802 ± 189	5.7

3.1.3 Coating materials

3.1.3.1 Graphene oxide (GO)

A GO water solution (4 mg/mL) was used as the source for glass fiber coating. It was provided by Graphenea Inc (San Sebastian, Spain). The mean particles size was < 10 μm.

3.1.3.2 Poly (ϵ-caprolactone) (PCL)

PCL was used as the interfacial self-healing agent and deposited on fiber surface as a coating. PCL was selected due to its physical and chemical compatibility with thermosetting matrices, and due to its low melting temperature (60 °C) that allows to easily melt and flow in the crack. Two types of PCL (PCL-1 and PCL-2) were used, and their properties from datasheet are listed in Table 3.5.

Table 3.5 Properties of poly (ϵ-caprolactone) utilized in this thesis.

	Code	Producer	Form	Density (g/cm^3)	M_w * (g/mol)	T_g (°C)	T_m (°C)
PCL-1	Facilan™	3D4maker Inc.	Filament 3D-print	1.1	84500	-68	61
PCL-2	-	Poly science Inc.	Granules (3 mm)	1.1	80000	-67	60

* M_w = number average molecular weight

Quasi static tensile tests were performed as previously described for the cured epoxy systems. They were carried out on 1BA type dumbbell specimens (ISO 527), using an INSTRON 5969 (Instron, Norwood, USA) universal tensile tester equipped with load cell of 10 kN at 0.25 mm/min for the evaluation of the elastic modulus (using an extensometer Instron model 2620-601 with gage length of 12.5 mm) and at 1 mm/min for the evaluation of the ultimate properties.
PCL-1 exhibited tensile modulus (E) equal to 420.1 ± 52.2 MPa, tensile strength (σ_y) equal to 31.5 ± 3.5 MPa and elongation at break (ϵ_f) equal to 18.2 ± 4.3 %. PCL-2 showed tensile modulus (E) equal to 385.3 ± 68.6 MPa, tensile strength (σ_y) equal to 13.5 ± 0.2 MPa and elongation at break (ϵ_f) equal to 26.9 ± 3.3 %.

3.2 Experimental techniques

In this section, a comprehensive overview of the experimental techniques utilized for the characterization of the prepared materials is presented. The description includes the specific techniques, procedures, and instrumentations employed in the investigation.

3.2.1 Microstructural properties

3.2.1.1 Optical microscopy (OM)

Optical microscope was utilized to observe the surface of neat and coated fibers, and to measure the fiber diameter and the epoxy

microdrop length in microdebonding. A Nikon SMZ25 optical microscope was used, equipped with a Nikon DS-Fi2 digital camera (Nikon, Tokyo, Japan).

3.2.1.2 Scanning electron microscopy (SEM)

The morphological analysis of the neat fibers and treated/coated fibers was carried out using a Zeiss Supra 40 (Carl Zeiss Ag, Oberkochen, Germany) field-emission scanning electron microscope, and a JSM-IT500 (Jeol Ldt, Dubai, UAE) scanning electron microscope. The first operated at 3.5 kV, the second at 10 kV. In both cases, prior to the analysis, the samples were coated with a Pt/Pd alloy (80:20) for 20 seconds in order to have a coating thickness of about 4 nm.

3.2.1.3 Atomic force microscopy (AFM)

Surface topography of coated and uncoated glass fibers was studied using a NT-MDT Solver Pro (NT-MDT Inc., Tempe, USA) system equipped with an Nova scanner. Images were collected in intermittent-contact mode using silicon tips (NSG-10, NT-MDT, 10 nm nominal tip radius, resonance frequency of 181 kHz). 20 × 20 μm^2 (512 × 512 pixels) topography scans were collected paying attention to land on the top of the glass fibers, in order to avoid areas outside the 4 μm scanner's Z range. Data representation and statistical analysis were performed with the support of Gwyddion analysis software. Roughness arithmetical mean height (R_a) and root mean square (R_q) was calculated following ISO standard 4287.

3.2.2 Evaluation of the density

An Accupyc 1330 helium pycnometer (Micromeritics Instrument Corporation, Norcross, USA) was used to measure the density of treated basalt fibers, keeping a constant temperature of 23 °C with a Haake D8 immersion heater. A 3.5 cm^3 crucible was used and a

minimum of 99 cycles were run to get an average density value for each sample.

3.2.3 Brookfield viscosimetry

The rheological properties of the PCL solutions used to coat the fibers were analysed through a Anton Paar Physica MCR 301 (Anton Paar, Graz, Austria) viscosimeter, by employing coaxial cylinders (diameter 17 mm). Tests were carried out at 24 °C to simulate the temperature conditions at which the coating of fibers was performed. An angular frequency of 100 rad/s was employed, with measurement points duration of 5 s.

3.2.4 Thermogravimetric analysis (TGA)

Thermogravimetric analysis was carried out in order to evaluate the amount of PCL nanoparticles deposited on the surface of the fibers, by comparing the residual mass at 700 °C (m_{700}) of samples before and after coating. The measurements were performed by using a TA-IQ5000 IR (TA Instruments Inc, New Castle, USA) thermobalance under an nitrogen flow of 100 mL/min in a temperature interval from 35 °C to 700 °C and at a heating rate of 10 °C/min. Moreover, TGA was used to determine the thermal behaviour of PCL coating upon repeated healing cycles. Three isothermal measurements were performed at 80 °C for 30 minutes each, interrupted by heating and cooling ramps 30/80 °C at 10 °C/min in nitrogen environment with a flow of 100 mL/min.

3.2.5 Microdebonding tests (MB)

Fiber/matrix interfacial adhesion was evaluated by microdebonding test in terms of interfacial shear strength (IFSS). Both Instron 4502 universal testing machine (Instron, Norwood, USA) and Fibrobond® microdebonding apparatus (Fibrobotics Oy, Tampere, Finland) were employed. The first equipped with a 2.5 N load cell, the second with a 1 N load cell. Tests with Fibrobond® apparatus were performed at the Faculty of Engineering and Natural Sciences of Tampere

University (Finland). Epoxy resin droplets, ranging in diameter from 30 μm to 400 μm, were manually or automatically applied and subsequently cured on individual fiber filaments, which were randomly selected from the bundles and fixed to metallic frames. Figure 3.3 shows the debonding setups used for Instron 4502 (a) and for Fibrobond® apparatus (b). Test were carried at 0.75 mm/min in the case of Instron 4502, and at 8 μm/min in the case of Fibrobond® apparatus. Approximately 10-25 droplets were debonded on each fiber, with a total of ten fibers tested per sample.

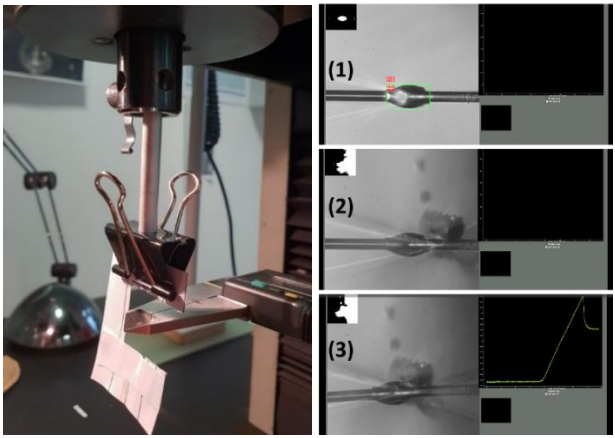

(a) (b)

Figure 3.3 Debonding setup for: (a) Instron 4502 and (b) Fibrobond® apparatus.

The interfacial shear strength (IFSS) was calculated as reported in Equation 3.8.

$$IFSS = \frac{F_{max}}{\pi dl} \quad 3.8$$

Where F_{max} represents the maximum force applied at the contact point between fiber and droplet, d is the diameter of the glass fiber, and l is the embedded length of the droplet. However, since the shear stress distribution varies along the interphase of the same fiber filament [41,42], in the case of Fibrobond® tests, the apparent IFSS

was calculated as the slope of the linear regression line that relates the maximum force (F_{max}) of individual droplets to their embedded area (A) (Equation 2.11).

$$F_{max} = IFSS_{app} \cdot A + q \quad 2.11$$

The slope corresponds to the apparent IFSS ($IFSS_{app}$) value, calculated in MPa, while the intercept q represents the influence of several experimental factors such as the range of embedded length selected, thermal-oxidative degradation of the matrix resin, and thermal residual stresses, as explained by Cai et al. [42].

After being debonded, the droplets were healed. In the case of GFs and BFs, the samples were placed in an oven at 80 °C for 30 or 60 minutes, while in the case of CFs, the samples were subjected to Joule heating as described in Section 3.2.6.2. After healing, samples were retested for debonding as previously described. From one to three cycles of debonding and healing cycles (i = 1,…3) were performed. The healing efficiency (H.E.) was calculated as the ratio between the interfacial shear strength after healing ($IFSS_H$) and the initial value of adhesion (IFSS), as reported in Equation 3.9.

$$H.E._{(i)} = \frac{IFSS_{H(i)}}{IFSS}, i = 1,..3 \quad 3.9$$

3.2.6 Electrical characterization

3.2.6.1 Evaluation of the electrical resistivity

The volumetric resistivity (ρ_v) of samples was evaluated by using a four point probe connected to an ammeter for current measurement, a voltmeter for voltage measurement and a DC power supplier (Figure 3.4a). A schematic representation of the probe is depicted in Figure 3.4b. Equation 3.10 was used to calculate the resistivity, where ΔV is the voltage measured by the voltmeter in volts, w and t are the width and thickness of the sample in meters, I is the current measured by the ammeter in amperes and L is the fixed distance between the two points where the voltmeter wires make contact to the sample and it is measured in meters. The total length of the sample was not considered in the calculation of the electrical resistivity.

$$\rho_V = \frac{\Delta V \cdot w \cdot t}{I \cdot L} \qquad 3.10$$

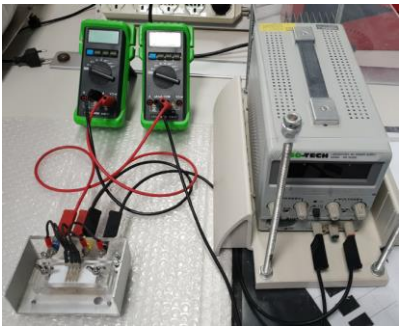

(a)

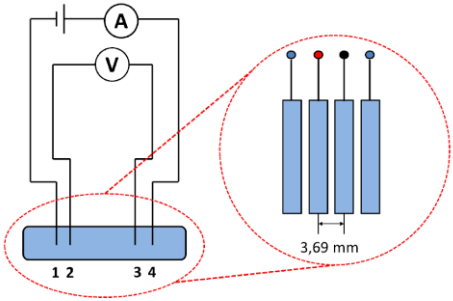

(b)

Figure 3.4 (a) Four-point probe equipped with an ammeter, voltmeter and current supplier, (b) probe's schematic representation.

3.2.6.2 Electrical conductivity test for self-healing

The interfacial healing of CFs was performed by Joule heating using a four-point probe connected to an ISO-tech DC supplier (ISO-tech IPS303DD, Germany) to apply a voltage at the two extremities of CFs (from 3.3 to 10 V). The temperature rise was measured against time using a RS 1319A K-type thermocouple placed in contact with the fibers in the probe. Figure 3.5 shows the used setup.

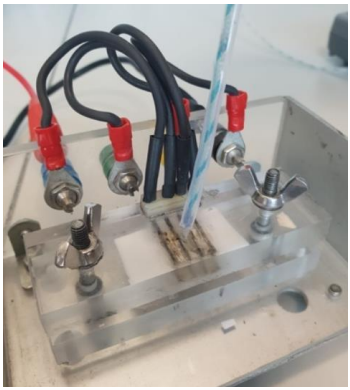

Figure 3.5 Joule heating of CFs measurement setup.

4 Evaluation of the fiber/matrix interfacial adhesion

Chapter 4 – Evaluation of the fiber/matrix interfacial adhesion presents the methodologies and the experimental results referred to the evaluation of the fiber/matrix interfacial adhesion of the prepared microcomposites. Some of the experiments were conducted in collaboration with the University of Vigo, in Spain, and the University of Tampere, in Finland.

4.1 Graphene oxide coating of glass fibers

Published paper:
Mahmood, H.; Simonini, L.; Dorigato, A.; Pegoretti, A. Graphene deposition on glass fibers by triboelectrification. *Applied Sciences* **2021**, *11*, 3123-3135.

The objective of this study was the investigation of a novel deposition method for electrically charged nanomaterials, like graphene oxide, on the surface of glass fibers. The aim was to enhance the quality of the deposition by exploiting the triboelectrification effect (TE) generated on the fibers, which attracts the nanomaterial forming a compact and highly uniform coating, as compared to a conventional dip-coating procedure. In fact, TE has never been investigated as a technique for fiber coating with nanofillers. TE is also known as contact electrification (CE), which technically means the creation of charges due to physical contact between (at least) two surfaces [92]. Briefly, TE is a tribological process involving two dissimilar materials that, when come in contact or are rubbed with each other, creates an electrical charge on their surfaces. Under given contact conditions, the magnitude and type of charges depend on the specific triboelectrification behaviour

of the materials in contact. This is summarized in the form of the so-called triboelectric series, which rank different materials according to their "tendency" to gain or lose electrons during the process. In the triboelectric series, glass is located on the top of the list, while polytetrafluoroethylene (PTFE) is located at the bottom of the series. Rubbing or even touching these two materials results in a high charge transfer on both of them. On the basis of this natural phenomenon, in this work, glass fibers roving was passed at different velocities over one or two PTFE surfaces, and the amount of charge developed by CE on GF was analyzed. In another step, such triboelectrified fibers were passed through GO solutions at different concentrations to be coated. Next, GO coatings were chemically reduced to create rGO coated GF. Such coating, having an electrically conductive nature, could provide the possibility to achieve multi-functionality in composite materials.
The materials and the techniques utilized to prepare and characterize the samples are presented in this section. Their detailed description have already been presented in Chapter 3.

4.1.1 Materials and methods

4.1.1.1 Materials

The materials employed in the preparation of samples are listed in Table 4.1. A more detailed description can be found in Section 3.1.

Table 4.1 List of materials employed for the preparation of samples.

Constituent	Label	Material
Matrix	EP-1	Epoxy matrix (EC 157, W 342)
Fibers	GF	Glass fibers (PPG 2001)
Coating material	GO	Graphene oxide

Additionally, hydrazine hydrate was used to reduce GO to reduced-graphene oxide (rGO). It was provided by Sigma Aldrich Co. (Saint

Louis, Missouri, USA) as a liquid having purity of 99.9% and density of 1.029 g/ml at 25 °C.

4.1.1.2 Sample preparation

Graphene oxide was deposited taking advantage from the "triboelectric effect" (TE) that induces surface electrification due to the contact between different objects [92]. A schematic and realistic representation (inside and outside a Faraday cage) of the lab-made setup employed for the TE of glass fibers is presented in Figure 4.1(a,b).

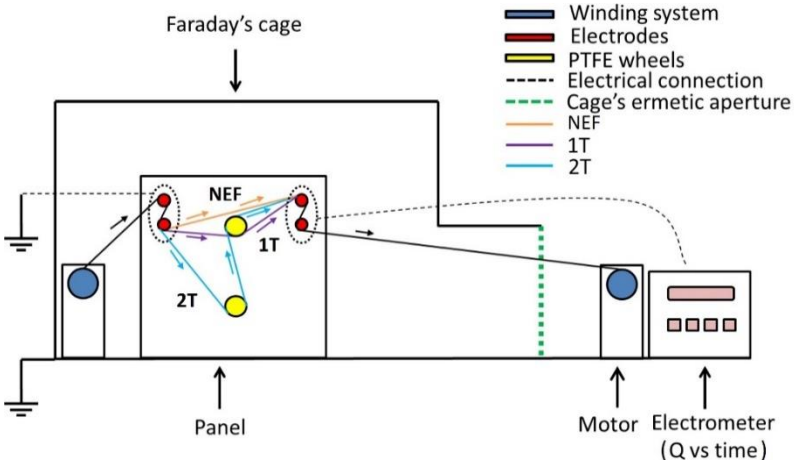

(a)

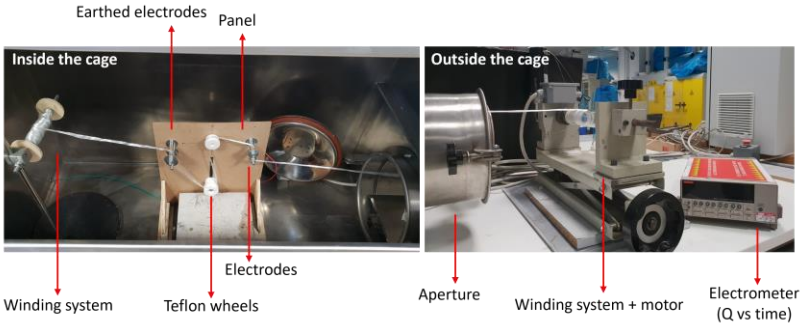

(b)

Figure 4.1 (a) Schematic representation and (b) realistic representation (inside and outside a Faraday cage) of the lab-made setup for the triboelectrification of glass fiber and charge measurements tests.

The system consisted of two fiber winding systems: the first system housed wound fibers (W1), while the second system drawn the fibers using an electric motor (W2). The apparatus comprised a vertical insulating wooden panel containing two grounded steel electrodes (E1), along with two polytetrafluoroethylene (PTFE) wheels (P1 and P2) mounted at the centre. Additionally, there were two other steel electrodes (E2) connected to a Keithley 6517A electrometer (Tektronix Inc., USA). The electrometer was controlled using a MATLAB program to enable real-time acquisition of the surface charge on the glass fibers (GFs) with respect to the fiber scrolling time. All components of the system, except the electrometer, were enclosed within a grounded Faraday cage. The TE process of the glass fibers initially involved the scrolling of fibers from W1 to E1. The positioning of the two electrodes in E1 ensured that both sides of the fibers made contact with the electrodes, facilitating the discharge of any pre-existing electrification in the as-received fibers. Subsequently, for the analysis of the TE process, the discharged fibers followed three distinct paths. For the analysis of discharged fibers only (NEF – non electrified fibers), the fibers passed over the

E2 electrodes for charge measurement. In the case of TE involving one PTFE (1T), GF passed over P1 exclusively and then over E2 electrodes for charge measurement. Finally, for charge enhancement involving two PTFEs (2T), GF passed over both P2 and P1 before proceeding over E2 electrodes for charge measurement. The NEF pathway served the purpose of assessing pre-existing electrification phenomena present in the fibers. On the other hand, the 1T pathway was utilized to examine the effect of contact electrification on fibers using a single point of contact with PTFE. The 2T pathway was used to understand the potential impact of an increased number of contact points between fibers and PTFE on the electrification level. Throughout the experimental tests, a close monitoring of temperature and humidity levels within the enclosure was conducted, as these factors could significantly influence the charge measurements. According to established literature, to ensure reliable charge measurements, the recommended temperature should be maintained around 23 °C with an optimal humidity range between 20% to 25% [93]. The entire TE process encompassed testing at three distinct scrolling velocities (2.8 rpm, 5.4 rpm and 18.4 rpm) to comprehensively evaluate their influence on the development of surface charge.

Regarding the TE-based deposition of graphene oxide (GO), a similar setup was employed with a slight modification: the fibers did not pass over the second set of electrodes (E2). Instead, after following paths 1T or 2T (as illustrated in Figure 4.2), the fibers were immersed in a graphene oxide bath. Subsequently, electrified coated fibers were compared with NEF fibers, whereby the GO coating for NEF was manually applied by immersing the discharged fibers in a GO bath. After deposition, all coated fibers were subjected to a drying process in an oven for a minimum of 12 hours at 50 °C under vacuum conditions. The chemical reduction of GO-coated glass fibers involved exposing them to a hydrazine hydrate-rich environment at 100 °C for a duration of 24 hours [75].

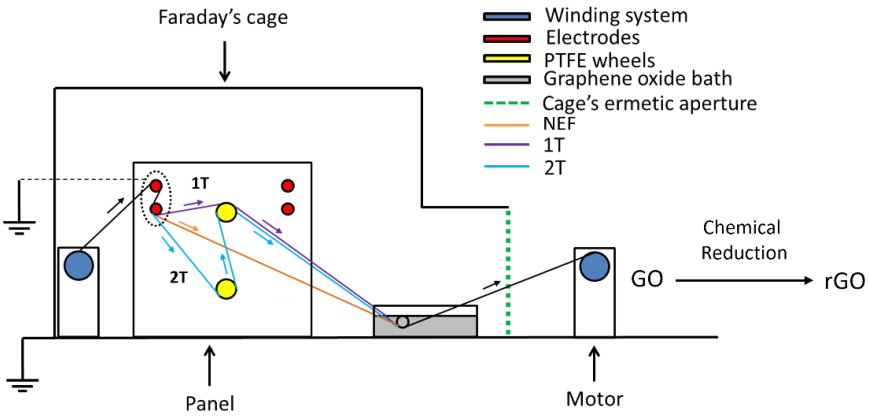

Figure 4.2 Schematic representation of the triboelectrification deposition process of graphene oxide on glass fibers.

The list of the produced GO and rGO coated glass fibers is reported in Table 4.2. The first number represents the initial graphene oxide concentration (wt%), then the coating type (GO or rGO) and the electrification process are reported.

Table 4.2 List of the prepared uncoated and coated glass fibers.

Sample Name	GO (wt%)	Electrification process
GF*	-	-
0.005 GO NEF/ 0.005 rGO NEF	0.005	NEF
0.005 GO 1T/ 0.005 rGO 1T	0.005	1T
0.005 GO 2T/ 0.005 rGO 2T	0.005	2T
0.05 GO NEF/ 0.05 rGO NEF	0.05	NEF
0.05 GO 1T/ 0.05 rGO 1T	0.05	1T
0.05 GO 2T/ 0.05 rGO 2T	0.05	2T
0.1 GO NEF/ 0.1 rGO NEF	0.1	NEF
0.1 GO 1T/ 0.1 rGO 1T	0.1	1T
0.1 GO 2T/ 0.1 rGO 2T	0.1	2T

*Glass fibers neither triboelectrified nor coated with graphene oxide

4.1.1.3 Experimental techniques

The techniques used to characterized the prepared samples are listed in Table 4.3. A more detailed description can be found in Section 3.2.

Table 4.3 List of experimental techniques.

Technique	Parameters	Aim
Optical microscopy	Section 3.2.1.1	To measure fibers diameter and epoxy drops lengths
SEM	Section 3.2.1.2	To analyze the surface morphology of coated and uncoated fibers
Microdebonding tests	Section 3.2.5	To evaluate the interfacial shear strength (IFSS)
Electrical resistivity tests	Section 3.2.6.1	To evaluate the electrical conductivity of coated GF

4.1.2 Results and discussion

4.1.2.1 Morphological characterization

The physical appearances of glass fibers coated by the TE method are compared in Figure 4.3.

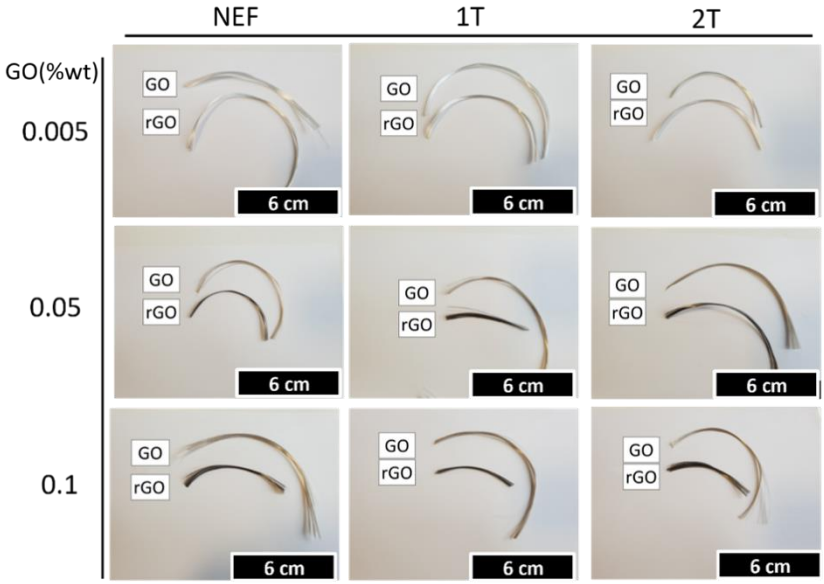

Figure 4.3 Representative images of 0.005 GO/ rGO, 0.05 GO/ rGO, and 0.1 GO/ rGO fibers (NEF, 1T, 2T).

GO-coated fibers show a light brown colour, while rGO coated glass fibers assume a darker colour due to the chemical reduction process [94]. The darkening effect can be better seen on GF-coated fibers with higher GO concentrations, probably because of the higher amount of deposited nanomaterial. Apparently, the effect of triboelectrification of GF on the GO deposition is not so evident, as NEF, 1T, and 2T specimens obtained with the same GO concentration have a similar optical appearance. The amount of electrical charges accumulated on GFs within 100 s by adopting NEF, 1T, and 2T paths is summarized in Figure 4.4.

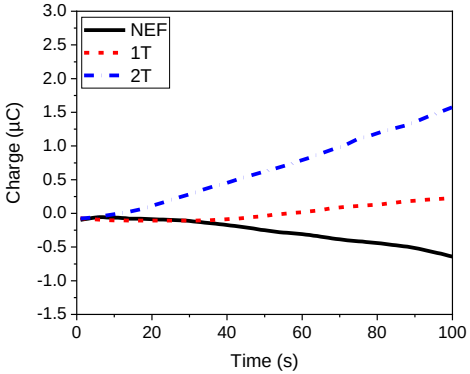

Figure 4.4 GF electrification curves obtained adopting NEF, 1T, and 2T paths at a scrolling velocity equal to 2.8 rpm.

For these preliminary charge measurements, the scrolling velocity was chosen arbitrarily equal to 2.8 rpm. The GF that followed the path NEF shows a partially negative pre-existing surface electrification owing to the rubbing of fibers with other materials during their storage. The grounded electrodes allow the fibers to be partially discharged. The use of efficiently grounded electrodes could be a valid possibility for improving the discharging of the fibers. Nevertheless, a completely discharged GF surface is not strictly necessary since the curve obtained from the NEF path account for the charge background. This is eventually subtracted from the curves obtained from 1T and 2T paths, allowing to detect the neat triboelectrification effect on the GF surface. GF, as expected, assumes a positive surface charge when rubbed against the PTFE wheels, thus indicating that an effective triboelectrification process has occurred. The increased number of contact points given by the contact with the second PTFE wheel allows a more intense surface charge electrification.

In Figure 4.5, the GF surface charge electrification curves obtained at three different scrolling velocities (i.e., 0.61 cm/s, 1.19 cm/s, and 4.05 cm/s), and following 1T path are reported.

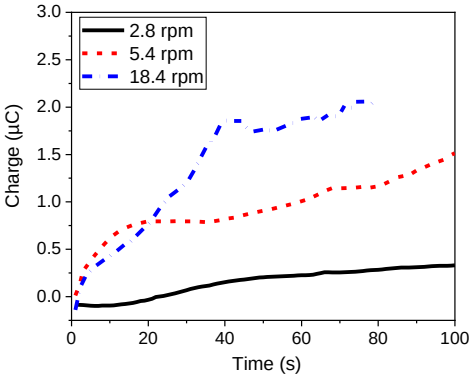

Figure 4.5 GF electrification curves at different scrolling velocities obtained following 1T path.

It can be seen that the higher the scrolling velocity, the greater the contact electrification. High scrolling velocity results in low contact time between fibers and PTFE wheels and thus in a high contact frequency. This means that the fibers are not discharged in air before being analyzed by the electrometer. Moreover, a high scrolling velocity induces an elevated contact pressure between the fibers and PTFE since the motor applies a higher tension on the fibers. High contact frequency and tension allow to have a higher contact efficiency and thus a higher triboelectrification effect. However, an excessive scrolling velocity leads to an unstable charge measurement due to the limitations on the maximum amount of charge measurable by the electrometer used (±2 μC). In fact, the curve obtained at the highest velocity (18.4 rpm) show a rapid increment of the surface electrification up to 40 s, then the electrification stabilizes showing a plateau approaching 2 μC. At about 80 s the measurement stops since the detectable charge limit is reached. Thus, for the coating process, an optimal scrolling velocity equal to 5.4 rpm was selected since it represents a good compromise between the intensity of the surface electrification and the requirement to minimize the

force applied on the fibers to preserve their mechanical properties. In Figure 4.6, a SEM image of a neat GF specimen is shown.

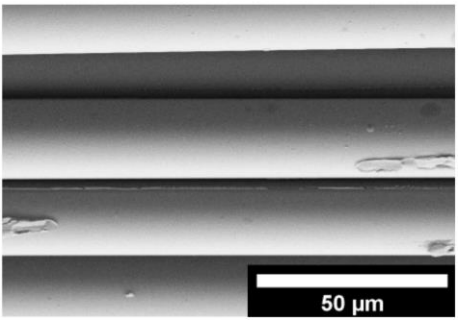

Figure 4.6 SEM image of neat GF.

The surface appears to be smooth with no substantial defects except for the presence of the sizing agent since the GF was used without any pretreatment. The surface morphology of the fibers after the rGO deposition as a function of CE intensity and the GO solution concentration can be evaluated in Figure 4.7.

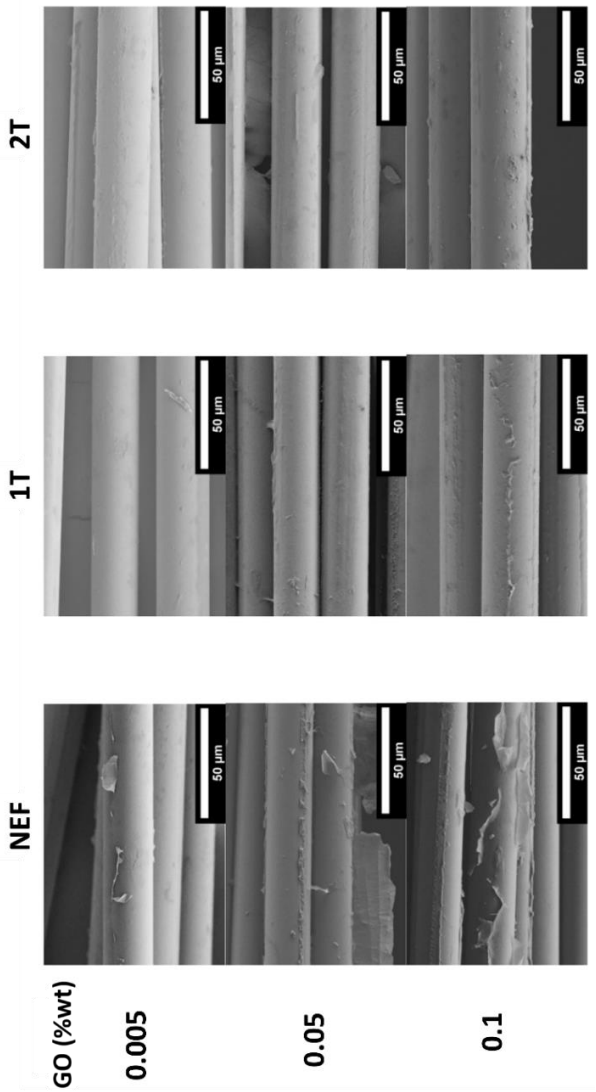

Figure 4.7 SEM images of rGO coated samples with varying graphene oxide (GO) concentration and electrification process.

It can be seen that for all GO solutions, the rGO nanosheets appear to be more homogeneously attached to the GF by increasing the intensity of the TE process (i.e., moving from NEF to 1T or 2T). This is due to the creation of an increasing amount of positive charges on the GF surface by TE, which electrostatically attracts the negatively charged graphene sheets on the fibers. Qualitatively, SEM images confirm the increase of rGO deposition with the concentration of the GO solution. The same conclusions cannot be done considering the intensity of the TE process, since the difference of the rGO amount deposited passing from NEF to 2T is too small to be detected by SEM analysis. Further quantitative investigations, for example by using friction force microscopy (FFM) [95,96], could give more information on the effective quantity of the nanomaterial deposited upon the electrification. However, it can be deduced that a physical interaction between GO nanosheets with charged GF takes place due to the creation of attractive surface charges on the latter. At a general level, it can be stated that the obtained homogeneity level of the deposited nanomaterial is a promising indication of an efficient deposition method.

4.1.2.2 Mechanical characterization

Representative load–displacement curves obtained from microdebonding tests on rGO coated glass fibers characterized by 2T electrification are reported in Figure 4.8 and compared with those of the uncoated GF sample. For each specimen, the obtained values of the pull-out force (F_{max}) were used for the calculation of the interfacial shear strength (IFSS), as described in Equation 3.8.

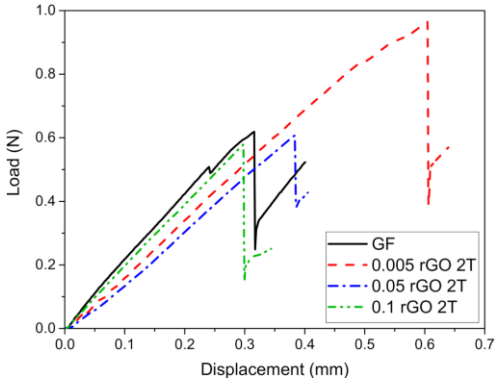

Figure 4.8 Comparison of load-displacement curves from microdebonding tests of uncoated GF and rGO coated GFs, with electrification path 2T.

A comparison of the average IFSS values of uncoated and rGO coated GF is shown in Figure 4.9.

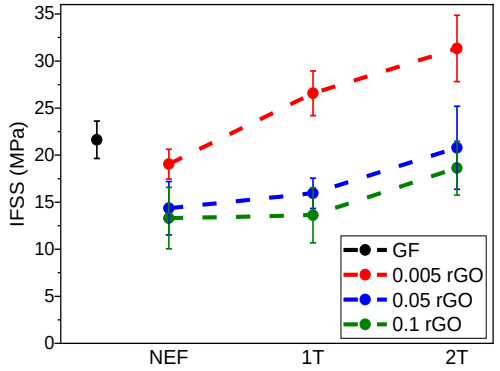

Figure 4.9 Comparison of interfacial shear strength (IFSS) values obtained from microdebonding tests on uncoated and rGO coated GFs.

A decrease of IFSS values is observed by increasing the GO content in the solution, while a considerable increment of IFSS values from

NEF to 2T can be registered in the case of 0.005 rGO coated fibers (+45% with respect to GF). It can be deduced that the TE-based coating under 2T conditions from the GO solution at the lowest concentration leads to the creation of an optimized rGO interphase that enhances fiber/matrix interfacial adhesion. The positive effect of electrification could be due to the fact that it promotes good compaction of the deposited coating since the GO sheets are electrostatically attracted by the opposite surface charges of the fibers. This results in lower relative sliding of the rGO sheets, favoring the adhesion of the matrix on the coated fibers. This compaction is likely partially lost, increasing the amount of nanomaterial deposited and allowing easier sliding between nanosheets, thus decreasing matrix/fiber adhesion.

4.1.2.3 Evaluation of the electrical resistivity

All rGO coated glass fibers were subjected to surface electrical resistivity measurements to evaluate the extent of the reduction of GO to rGO, and electrical resistivity values are reported in Figure 4.10.

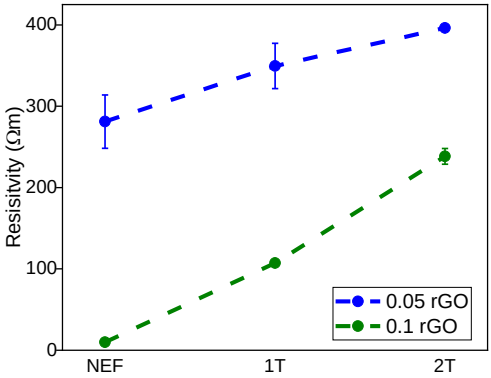

Figure 4.10 Electrical resistivity values of rGO coated fibers.

As expected, the presence of the conductive rGO layer on the fibers imparts a good electrical conductivity to the insulating GFs, thus demonstrating the validity of the deposition method. However, this is true only for the fibers coated with an elevated GO concentration, i.e., 0.05 and 0.1 rGO coated glass fibers. In the case of 0.005 rGO coated glass fibers, the resistivity measurement was not possible. An explanation could be that, for this sample, the percolation limit, i.e., the formation of a continuous network of reduced graphene oxide on the fiber surface, was not reached, and therefore electrical conductivity was too low to be measured. For 0.05 and 0.1 rGO coated GFs, the electrical resistivity shows lower values in the case of 0.1 rGO coated glass fibers. Having such fibers resistivity values much lower than neat GF, the successful reduction of GO to rGO is confirmed. However, the TE process does not significantly affect the resistivity values of rGO coated fibers. This suggests that the TE process for graphene coating does not significantly increase the amount of GO coating, rather than it only improves the quality of the coatings produced.

4.1.3 Conclusions

For the first time, triboelectrification was proposed as a valuable method for the deposition of electrically charged nanoparticles onto continuous glass fibers. The GF roving was rubbed against PTFE surface to generate surface charges by contact electrification. As per the triboelectric series, positive charges were created on the GFs, and these naturally attracted negatively charged GO in an aqueous dispersion. It was found that the electrical charge on the GF surface increased with the intensity of the TE process. GO coating on GFs was then chemically reduced to produce rGO coated GF. FESEM analysis confirmed the presence of the coating of rGO on GFs, as the TE process forced the rGO sheets to completely adhere onto the GFs surface. Micro composites were created by depositing epoxy drops on both uncoated and coated GFs. The micro debonding tests highlighted an enhancement of the fiber/matrix interfacial shear

strength of 45% in the case of rGO coated fibers in comparison to the uncoated ones. Moreover, electrical resistivity values significantly decreased to the presence of a continuous rGO coating onto the GF surface.

4.2 CO_2 laser treatment of basalt fibers

Paper in press:
Pozueco, S.; Simonini, L.; Mahmood, H.; Rigotti, D.; Kakkonen, M.; Riveiro, A.; Comesaña, A.; Pou, J.; Tanhuanpää, O.; Kanerva, M.; Sarlin, E.; Kallio, P.; Pegoretti, A. Influence of CO_2 laser surface treatment of basalt fibres on the mechanical properties of epoxy/basalt composites. *Polymer Composites.*

The objective of this study was the investigation of an alternative method to improve fiber/matrix interfacial adhesion, different from the conventional chemical approaches that result costly and environmentally impactful. In the study, CO_2 laser surface treatment on basalt fibers was utilized to provide morphological changes of fiber surface, therefore to enhance the mechanical interlocking component of adhesion.
The materials and the techniques utilized to prepare and to characterize the samples are presented in this section. Their detailed description have been already presented in Chapter 3.

4.2.1 Materials and methods

4.2.1.1 Materials

The materials employed in the preparation of the samples are listed in Table 4.4. A more detailed description can be found in Section 3.1.

Table 4.4 List of materials employed in the preparation of samples.

Constituent	Label	Material
Matrix	EP-2	Epoxy matrix (EC 141 NF, W 242 NF)
Fiber	BF	Basalt fibers - fabric (BAS 220 P)

4.2.1.2 Sample preparation

Basalt fibre mats were treated using a CO_2 laser (Synrad 48 – 2 Series) emitting a continuous wave (CW) laser radiation. A TEM00

laser beam (M2<1.2), with a wavelength of 10.6 μm, was scanned over the surface of the basalt fabric by using a F-theta lens with focal length of 300 mm. The laser treatment was carried out on both sides of the mats. The treatment was performed with a scanning speed of 600 mm/s and 0% overlap. To observe the macroscopic influence of the laser on the basalt fibres, power levels were used in 0.13 W/mm^2 increments from 0.65 W/mm^2 to 1.30 W/mm^2 (i.e., 0.65, 0.73, 0.78, 0.81, 0.88, 0.91, 0.96, 1.04, 1.17 and 1.30 W/mm^2), and two further power levels of 1.56 W/mm^2 and 2.08 W/mm^2. For the rest of the experiments, power levels with 0.18 W/mm^2 increments from 0.73 W/mm^2 to 1.12 W/mm^2 were used. The processing parameters were selected based on preliminary tests.

4.2.1.3 Experimental techniques

The techniques used to characterize the prepared samples are listed in Table 4.5. A more detailed description can be found in Section 3.2.

Table 4.5 List of experimental techniques.

Technique	Parameters	Aim
Optical microscopy	Section 3.2.1.1	To observe the surface morphology of BF and to measure their diameters
SEM	Section 3.2.1.2	To analyze the surface morphology of BF
Density	Section 3.2.2	To measure the BF density
Single fiber tensile tests	Section 3.1.2	To measure shape (m) and scale (σ_0) parameters of Weibull distribution
Microdebonding tests	Section 3.2.5	To determine the interfacial shear strength (IFSS)

4.2.2 Results and discussion

4.2.2.1 Morphological characterization

Optical microscope images visualise the structural changes of basalt fibre fabrics after CO_2 laser treatment. Figure 4.11 shows that at a low power (0.65 W/mm^2) some fibres break, while increasing further the power the formation of fused fibres starts to get evident at the macroscopic level. However, as the laser power is further increased, the melting becomes clearer creating large areas where fibres are fused, and small spheres formed because of the agglomeration of the molten basalt. The observed micro-damages on fibre surface induced by the treatment could provide the necessary mechanical interlocking between the fibre fabric and the polymer matrix, thus potentially improving the interfacial shear strength. However, this rise in power is also accompanied by excessive fibre breakage and thermal degradation, since, as it can be seen, for laser powers above 1.12 W/mm^2, large voids are formed in the fabric. At this point, it was decided to continue further investigations using selected treated fibres i.e., 0.73 W/mm^2, 0.81 W/mm^2, 0.88 W/mm^2, 0.96 W/mm^2, 1.04 W/mm^2, 1.12 W/mm^2. Fibres treated at a power levels lower than 0.81 W/mm^2 and higher 1.12 W/mm^2 were ignored due to in-existent or excessive structure modification, respectively.

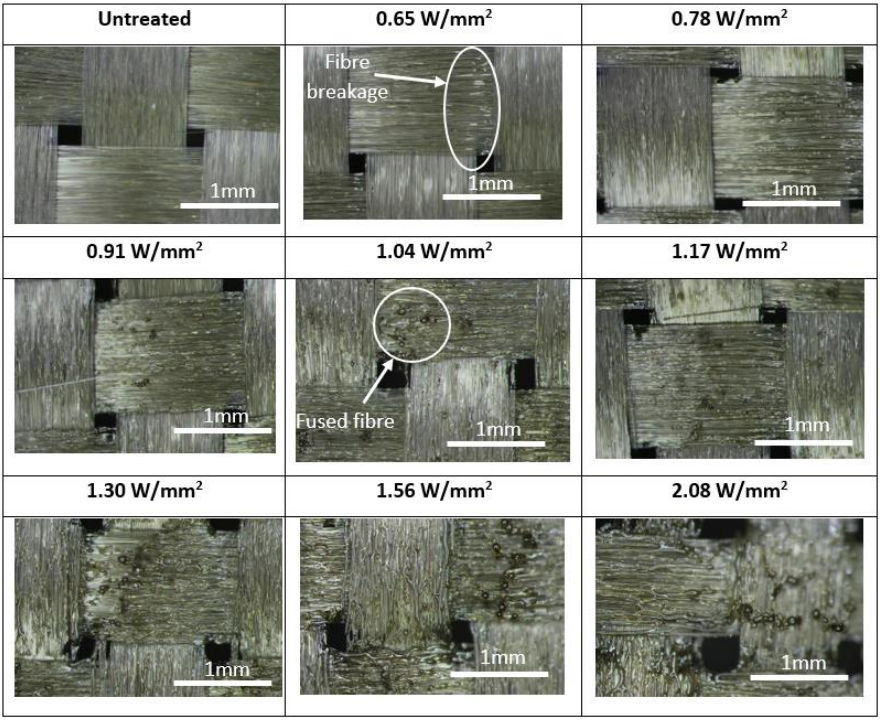

Figure 4.11 Optical images of untreated and some laser-treated basalt fibre mats (laser power ranging from 0.65 to 2.08 W/mm²).

On the other hand, no significant superficial modification at the microscopic scale can be observed, as it can be seen in the SEM images for laser power levels lower than 1.04 W/mm² (see Figure 4.12). However, when a laser power of 1.04 W/mm² is applied, the laser treatment provides energy enough to induce a surface roughness increase as shown in Figure 4.13(a, c). At such energy level, melting of basalt fibres is also observed, as shown in Figure 4.13(b), in which fibres fused together can be noticed. However, when a power higher than 1.04 W/mm² is applied, as shown in Figure 4.13 (d-f) for power level 1.12 W/mm², the treatment provides excessive thermal energy that goes beyond the induction of surface

roughness, producing a melting and breakage of the fibres as hence reducing the strength of the reinforcing phase. Also, an accumulation of material is also observed at the fibre ends in Figure 4.13(e).

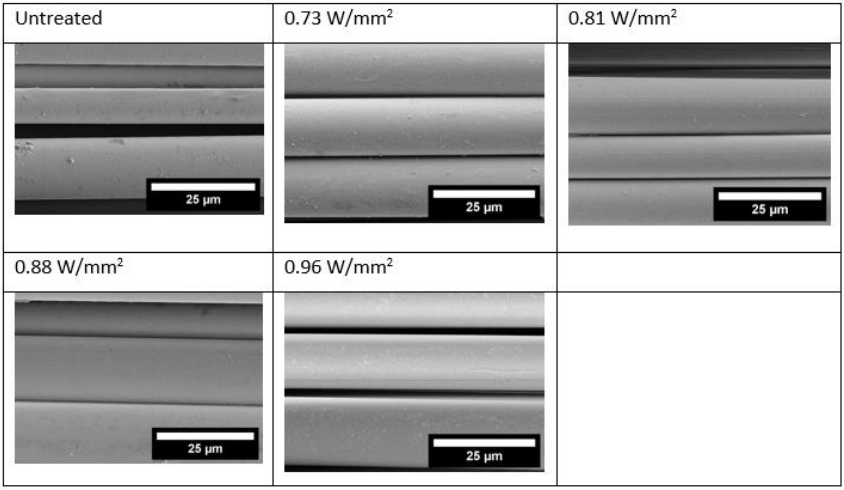

Figure 4.12 SEM images of untreated and treated basalt fibres under laser power lower than 1.04 W/mm² (laser power ranging from 0.73 W/mm² to 0.96 W/mm²).

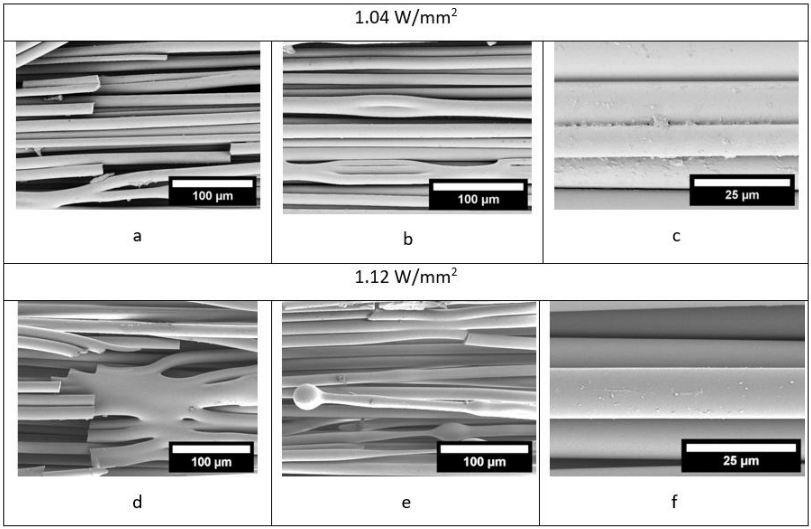

Figure 4.13 SEM images of treated basalt fibres under a laser power of 1.04 W /mm² and 1.12 W/mm²

4.2.2.2 Mechanical characterization

The Weibull scale parameter (λ) in Table 4.6 (L_0 = 15 mm)) shows how the treatment modifies the tensile strength of individual fibres for almost all treated fibres. From the table, it can be induced that the higher the laser power, the higher the damage, for any of the tested lengths. However, for a laser power of 1.04 W/mm² the tensile properties are improved, as the scale parameter increases respect to the untreated sample. On the other hand, when 1.04 W/mm² is exceeded, the surface damage is reflected in a decrease in the fibre scale parameter. The shape parameter (m) shows to be susceptible to the elevated power. As the power increases to 1.12 W/mm², the value of m is drastically reduced. As known, the value of m is related to the variation of the tensile strength of the fibres, the higher the values of m, the less scattered are the strength values of the fibres [97]. Therefore, at elevated power, the basalt fibres show less homogeneity and more fluctuation in the tensile strength. This may

also be due to the fact that some fibres are above others and therefore the laser irradiation does not affect them all equally (or melt them together in fabric). In this regards, in a future development of this treatment, it would be recommended to use unidirectional basalt fibre fabrics or to subject the fibres to laser treatment prior to weaving. In this way, it would be possible to mitigate the presence of non-irradiated fibre regions, thereby to optimize the efficacy of the laser treatment along the entire fibre surface. Furthermore, the shape parameter values achieved for the untreated fibres are similar to those found in the literature [98] and their scale parameter are to that of certain commercial basalt fibres [99].

Table 4.6 Shape (m) and scale (λ) parameters for the untreated and laser-treated basalt fibres together with the adj R^2 of the fitting. Scale factor is referred to a fibre length of 15 mm.

		CO_2 laser treatment					
Power (W/mm^2)	Untreated	0.73	0.81	0.88	0.96	1.04	1.12
i*	5	4	5	4	6	5	6
m	5.28	3.37	3.70	2.37	2.45	3.91	2.45
σ_0 (MPa)	2776	2113	1911	2298	2698	3359	2462
Adj R^2	0.995	0.997	0.991	0.990	0.969	0.993	0.988

*i = number of iterations

The Young's modulus of both treated and untreated fibres is also calculated from the tensile tests performed. The investigation aimed to assess whether the treatment applied to the fibers had a discernible impact on their elastic modulus. The results indicate that there are no significant differences in elastic modulus across the various treatments, as illustrated in Figure 4.14. Statistical analysis, specifically analysis of variance (ANOVA), yields a p-value equal to 0.459 which indicates that the variations in elastic modulus are not statistically significant. Therefore, it can be inferred that the

treatment does not exert a substantial influence on the elastic modulus of the fibers.

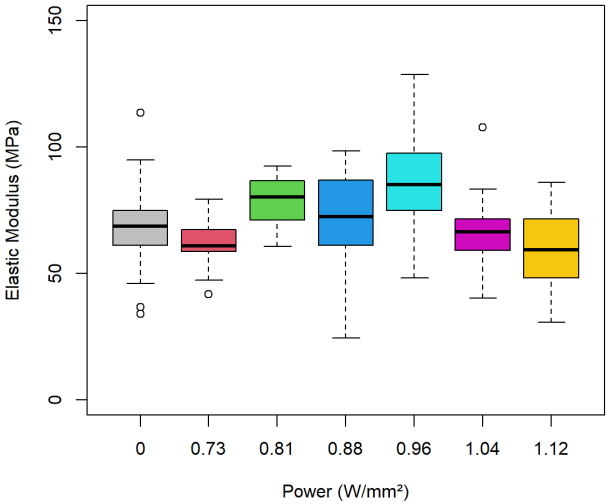

Figure 4.14 Boxplot for elastic modulus of untreated and laser-treated basalt fibers. Circular points represent outliers, points that differ significantly from other observations [100].

Any physical variation brought by the laser treatment was verified by analysing the physical aspects of the fibres i.e., the diameter and density. Looking at Figure 4.15(a), it can be seen that the fibres after the laser treatment manifest a slight decrease in the diameter, which could mean an increase in fibre density and thus explain the increase in the strength of the fibres treated with 1.04 W/mm² of laser power. However, the results obtained with helium pycnometer do not show a significant increase in density but a slight trend of densification with respect to laser treatment (Figure 4.15 (b)).

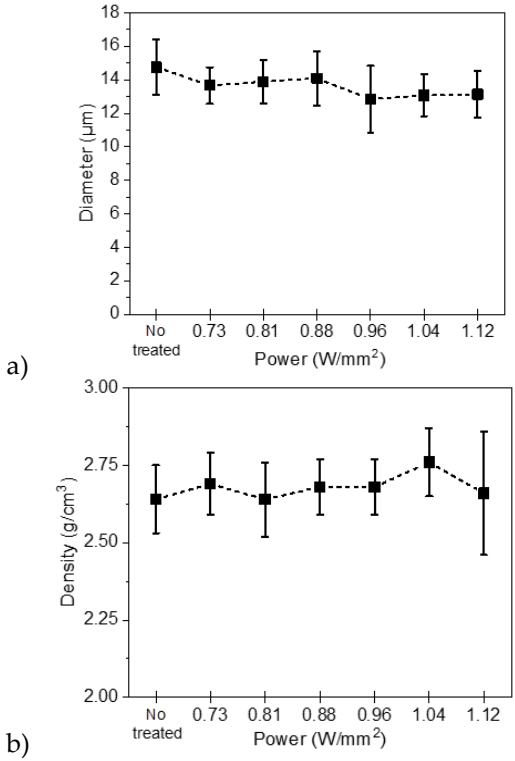

Figure 4.15 (a) Diameter and (b) density of untreated and laser-treated basalt fibres.

The IFSS of treated basalt fibres with epoxy resin was tested by measuring the load required to debond 24-28 droplets per fibre with varying embedded lengths. In Figure 4.16, one example of linear regression of the maximum force of individual droplets and the embedded area is shown for each sample. Meanwhile, in Table 4.7, the average values of IFSS resulting from the linear regression of each specimen per sample are summarized. Evidently, the "soft" laser treatment initially degrades the interfacial adhesion. However, gradually, the relatively high-powered treatment i.e., from 0.96

W/mm², the IFSS values start to increase. Clearly, the mean values are not significant among each other i.e., due to the presence of high uncertainties. This can be owed to the characteristic placement of filaments in a fibre mat which causes some fibres to be laser-treated more than the fibres that are present beneath. Hence, such non-uniform treatment of the fabric would be noticeable at such micro-level tests. Overall, these results also indicate the positive effect of laser treatment in terms of the enhancement of interfacial adhesion between the basalt fibres and the epoxy matrix. The morphological changes like surface roughness induced by the laser treatment enhances the physical locking mechanism at the interface which contribute positively on the bonding of the epoxy with the basalt fibres.

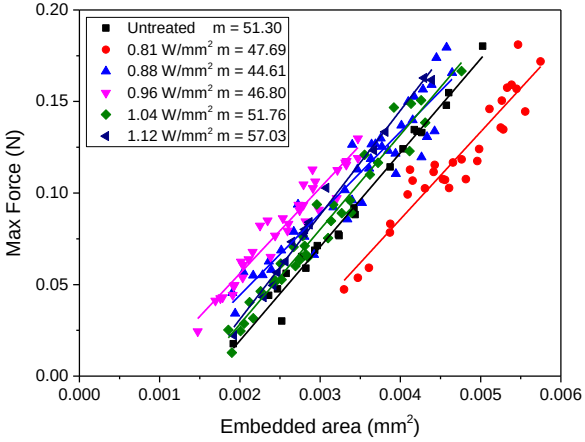

Figure 4.16 Maximum force vs embedded area from microdebonding test on untreated and treated basalt fibers.

Table 4.7 IFSS values from microdebonding tests on untreated and treated basalt fibre samples.

		CO_2 laser treatment				
Power (W/mm^2)	Untreated	0.81	0.88	0.96	1.04	1.12
IFSS (MPa)	51.8±4.7	48.3±4.4	41.4± 9.4	47.9 ± 13.6	53.7±8.4	56.0± 8.7

It is worthwhile to analyze the surface of the fibre after the droplet debonding in the microbond test. In this way, it is evident that the effect of laser treatment results in an increased interfacial adhesion at a microscale. Almost all the debonded droplets of each sample were analyzed under the FESEM and the characteristic fractography images of the most promising samples are reported in Figure 4.17. The figure compares three cases of microbond tests i.e., untreated fibres and fibres treated at 1.04 W/mm^2 and 1.12 W/mm^2. Apparently, the untreated basalt fibre surface after debonding appears to be without any residual epoxy resin adhered to its surface. This indicates a flat fracture path for the epoxy droplet to debond from the fibre which indicates to weak interfacial strength. Conversely, the samples treated at 1.04 W/mm^2 and at 1.12 W/mm^2, which provide significant enhancement in the interfacial adhesion, show a rough surface where debonding occurred. Hence the laser treatment promoted a morphological change of the fibre surface, which promotes mechanical interlocking of the matrix with the fibre and favours an enhancement of the interfacial adhesion.

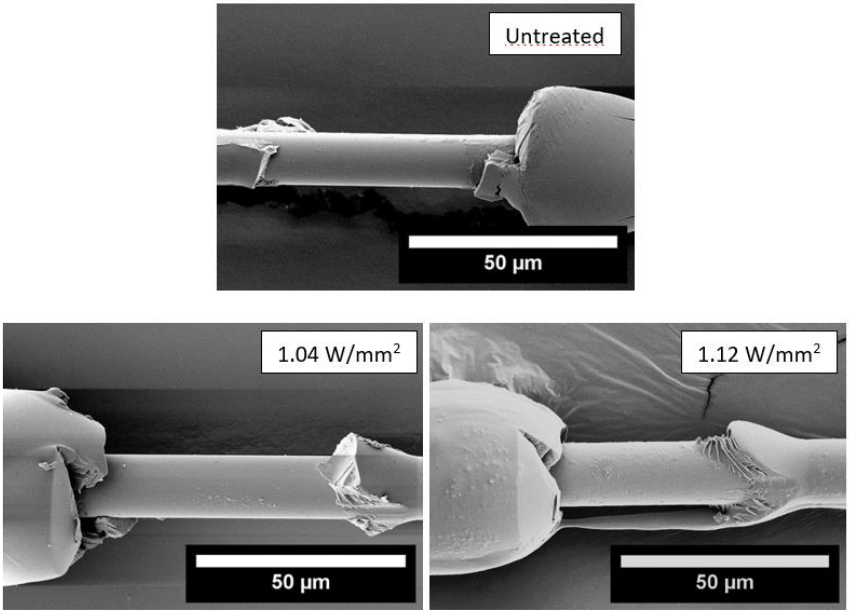

Figure 4.17 Representative micrographs of debonded microdroplets in microdebonding tests.

Therefore, this work demonstrates that, by means of laser irradiation, it is possible to improve the mechanical properties of basalt fibre-based composites. This requires the use of powers levels of 1.04 W/mm², as this creates both microscopic and macroscopic structures that facilitate the mechanical interlocking between the fibres and the matrix. In addition, this treatment leads to an improvement in both the interfacial adhesion and the mechanical strength of the fibres.

4.2.3 Conclusions

In this study, different tests have been carried out to characterise the influence of laser treatment on basalt fibre fabrics and their interfacial strength with epoxy resin. It was found that for a power of 1.04W/mm² the tensile strength increased, while the Young's

modulus did not experience a substantial variation due to the treatment. The increase in tensile strength was linked to the densification of the fibres at high scanning powers. The interfacial adhesion between the fibres and the epoxy matrix, tested by an automated microbond testing, was observed to improve at the highest investigated laser powers. Traces of residual epoxy matrix on the debonded surface of the treated fibre was also noted. Such improvement is concluded mainly due to the surface roughness induced by the laser radiation when melting the fibres surfaces, which is observed macroscopically, and to the structures formed at the microscopic level with 1.04W/mm^2 power, which improved the mechanical interlocking between the fibres and the matrix. This study opens the door for the promotion of the mechanical properties of basalt fibre composites by the utilization of low-power CO_2 laser sources.

5 Evaluation of the fiber/matrix interfacial self-healing

Chapter 5 – Evaluation of the fiber/matrix interfacial self-healing presents the methods and the experimental results to provide self-healing capability at the fiber/matrix interphase. Some of the experiments were conducted in collaboration with the University of Tampere, in Finland, during a two-month visiting period.

5.1 Continuous PCL film coating of glass fibers

Paper in preparation:
Simonini., L.; Kakkonen, M.; Dsouza, R; Kanerva, M.; Mahmood, H.; Dorigato, D.; Pegoretti, A. Tailoring the interfacial properties of glass fiber/epoxy microcomposites through the development of a multifunctional poly(ϵ-caprolactone) interphase

The aim of this study was the deposition of a polycaprolactone (PCL) coating on the surface of glass fibers, which acts like a self-healing medium when combined with epoxy matrix. PCL coating was obtained following the theory of *fluid coating*. Fluid coating is the operation of forcing a fluid to coat a solid while the solid is in movement [65]. When the velocity of the solid is zero, no film is formed because the coating is the result of a dynamic process. When the velocity is infinite, the same result is obtained since the film has not the enough time to form. Therefore, the thickness of the coating is velocity-dependent: the slower is the movement of the solid than the liquid, the thinner is the coating. A wide description of the phenomenon is explained by De Ryck et al. [66]. In this work, the coating procedure is schematized in Figure 5.1, where v is the velocity of uGF. The region where the film forms is called dynamic meniscus, having thickness h and length λ.

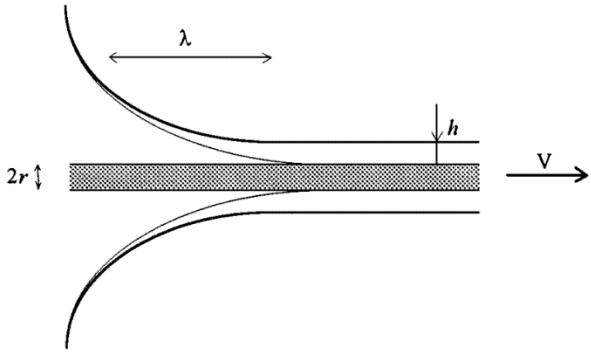

Figure 5.1 Schematization of the deposition of PCL film on uGF, adapted from [66].

The materials and the techniques utilized to prepare and to characterize the samples are presented in this section. Their detailed description have been already presented in Chapter 3.

5.1.1 Materials and methods

5.1.1.1 Materials

The materials employed for the preparation of the samples are listed in Table 5.1. A more detailed description can be found in Section 3.1.

Table 5.1 List of materials employed for the preparation of microcomposites.

Constituent	Label	Material
Matrix	EP-1	Epoxy matrix (EC 157, W 342)
Fiber	uGF	Unsized glass fiber (Windstrand®)
Coating material	PCL-2	Poly (ϵ-caprolactone)

Additionally, dimethylformamide (DMF) (density 0.94 g/cm^3 and purity of 99.8 %) and tetrahydrofuran (THF) (density 0.89 g/cm^3 and purity ≥ 99.9 %) were used in the preparation of PCL liquid solution.

They were purchased by Sigma Aldrich Co. (Saint Louis, Missouri, USA).

5.1.1.2 Sample preparation

Prior to fiber coating, PCL was dissolved in a mixture of dimethylformamide (DMF) and tetrahydrofuran (THF), at a DMF:THF weight ratio of 30:70, resulting in a solution containing 10 wt% of PCL [101]. The solution was stirred at room temperature for 4 hours at 300 rpm until the achievement of a complete dissolution. Subsequently, the solution was degassed for 10 minutes to eliminate air bubbles that formed during the stirring procedure. Then, both ends of a single uGF fiber were fixed to a custom metallic sample holder utilizing UV light-cured adhesive (Figure 5.2a). Simultaneously, a micropipette was utilized to dispense single droplets of the PCL solution onto a poly(methyl methacrylate) (PMMA) frame made of rectangular holes (Figure 5.2b). The metallic sample holder and PMMA frame were secured onto a Fibrobond® apparatus (Fibrobond Oy, Tampere, Finland), in order to allow the passage of the fiber through the PCL-filled holes on the PMMA frame.

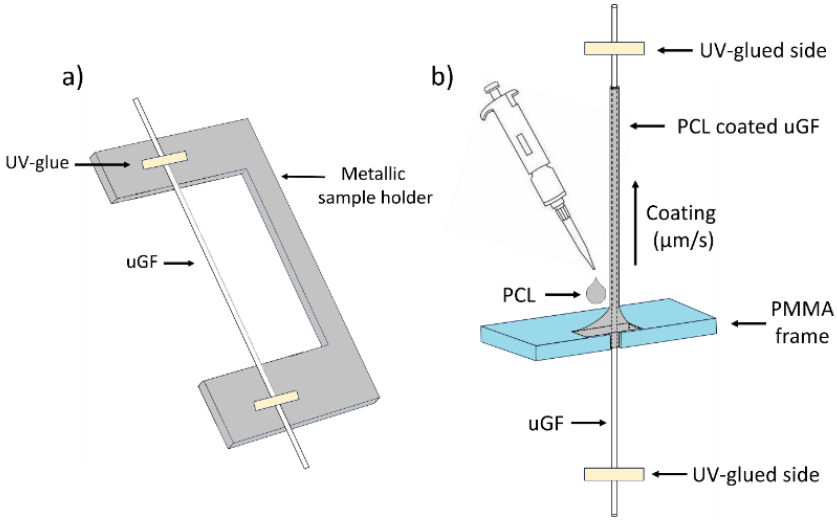

Figure 5.2 (a) Filament of uGF UV-glued on PMMA frame, (b) schematization of uGF coating.

Therefore, it was possible to control the velocity of the coating process along the fiber's length. Six distinct coating velocities were selected (500, 1000, 2000, 2500, 3000, 3500 μm/s). uGF fibers coated with PCL were denoted as "uGF", along with the corresponding coating velocity. For instance, "2500_uGF" designates unsized glass fibers coated with PCL deposited at 2500 μm/s.

5.1.1.3 Experimental techniques

The techniques used to characterize the prepared samples are listed in Table 5.2. A more detailed description can be found in Section 3.2.

Table 5.2 List of experimental techniques.

Technique	Parameters	Aim
Brookfiled viscosimetry	Section 3.2.3	To evaluate the rheological properties of PCL solution
SEM	Section 3.2.1.2	To analyze surface morphology of coated and uncoated fibers
TGA	Section 3.2.4	To determine the thermal properties of PCL upon repeated healing cycles
AFM	Section 3.2.1.3	To determine the surface topography and roughness of coated and uncoated fibers
Microdebonding	Section 3.2.5	To determine the interfacial shear strength (IFSS) and self-healing efficiency (H.E.) in microcomposites

5.1.2 Results and discussion

5.1.2.1 Rheological characterization

The viscosity of PCL solution plays a crucial role during uGF coating. The coating thickness is influenced by both the coating velocity and the viscosity of the coating medium. Consequently, to control the coating thickness, the viscosity has to be constant while the coating velocity can vary.

From Figure 5.3a, a slight increase in viscosity is observed over time due to solvent evaporation. At approximately 1 hour and 45 minutes, a significant increase in the solution viscosity is observed, indicating a transition from a liquid-like state to a more gel-like state. However, considering that the deposition process takes only 10 minutes, it is reasonable to consider that the solution viscosity is stable throughout the whole process. Additionally, the PCL liquid solution results to behave like a Newtonian fluid, as shown in Figure 5.3b.

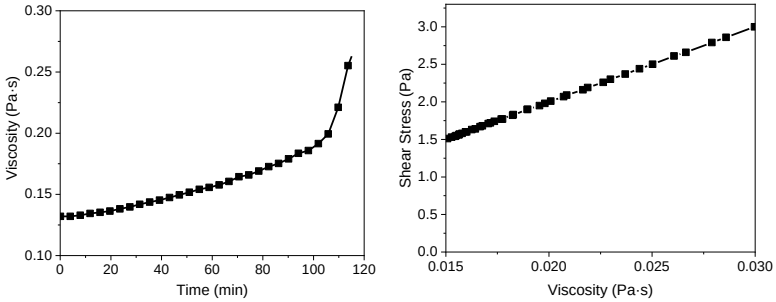

(a) (b)

Figure 5.3 (a) Evolution of the viscosity of PCL solution overtime at room temperature, (b) Newtonian behaviour of the PCL liquid solution.

5.1.2.2 Morphological characterization

In Figure 5.4, SEM images show the progressive deposition of the coating as a function of the coating velocity, resulting in a homogeneous and consistent appearance without substantial irregularities. Some dust particles are visible on the 2500_uGF sample, likely due to environmental contamination within the laboratory.

ImageJ 1.53a software was employed to quantify both the fiber diameter and coating thickness. The distribution of coating thickness (t) as a function of the coating velocity is reported in Figure 5.5. As anticipated, assuming constant viscosity of the polymeric solution during the coating process, a higher coating speed results in a thicker deposited coating. Notably, the mean thickness values range from 1.6 to 3.1 μm, considering the coating speed from 2500 to 3500 μm/s. Below 2500 μm/s, the PCL coating appears irregular and inconsistent. Coating speeds beyond 3500 μm/s were omitted as they led to the formation of PCL microdroplets instead of a homogenous film. This undesirable outcome is attributed to the Plateau-Rayleigh instability, a phenomenon explained by De Ryck et al. [66], which is

based on the surface tension of liquids that tends to minimise their surface area by forming droplets.

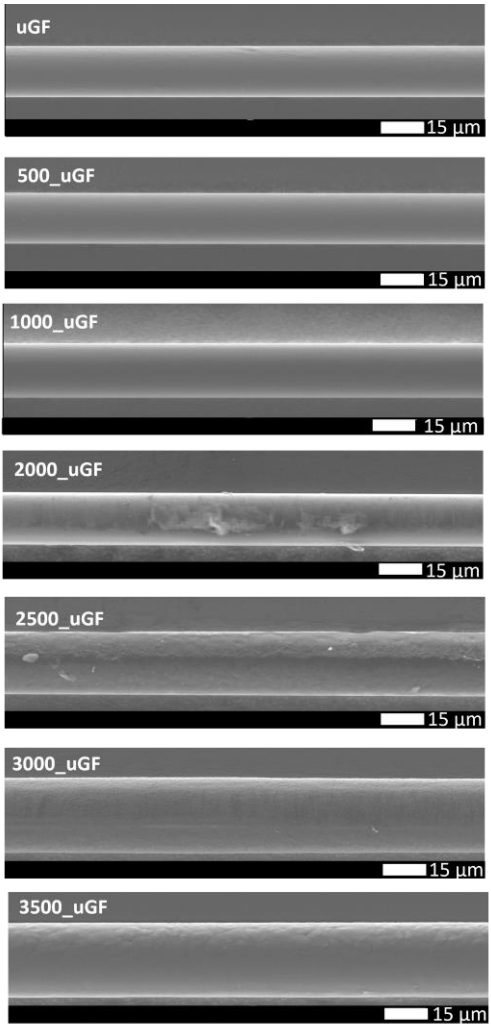

Figure 5.4 Morphological appearance of neat and PCL-coated uGF as a function of coating velocity.

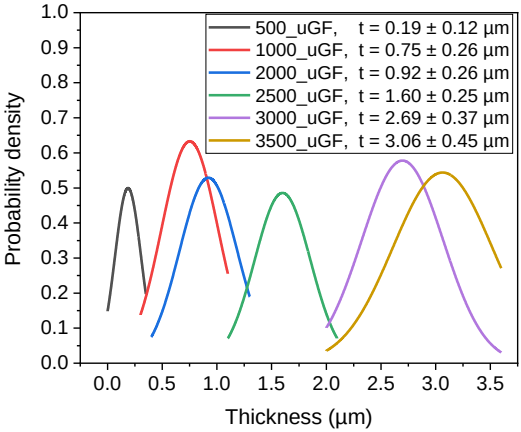

Figure 5.5 Normal distribution of the coating thickness as a function of the coating velocity.

5.1.2.3 Mechanical characterization

Evaluation of the IFSS

The apparent interfacial shear strength (IFSS) in epoxy-glass fibers was calculated by measuring the load necessary to debond 15-25 droplets per fiber, as expressed by Equation 3.9. Figure 5.6(a) shows the representative linear regression lines that relate the maximum load applied to individual droplets against the respective embedded areas, for a single filament. This graph includes the linear equations and R^2 values. Additionally, Figure 5.6(b) summarizes the mean IFSS values for each fiber sample.

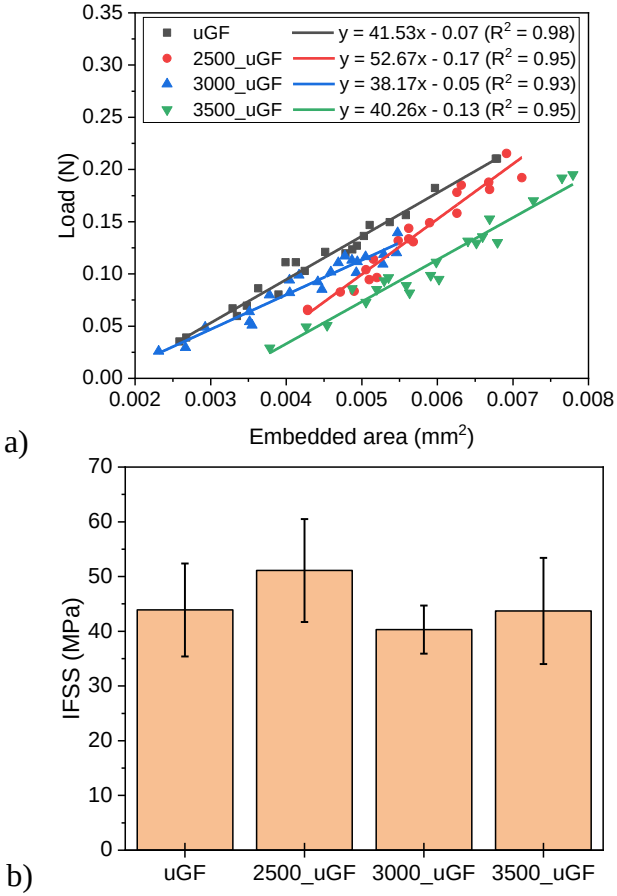

Figure 5.6 (a) Linear regression of the maximum load applied to individual droplets vs. embedded area per one single filament, (b) IFSS values obtained from the slopes of the linear regressions of each filament per fiber.

From Figure 5.6a, the data points have a linear fitting with R^2 of approximately 0.95, indicating a strong linear relationship. The observation of a high R^2 value implies that the fiber/matrix adhesion

remains consistent throughout the entire fiber length. This aspect is particularly important in the case of PCL-coated uGF, where high values of R^2 indicate the reliable and uniform deposition of the coating on uGF. On the other hand, the q values display a negative sign. Cai et al. [102] indicated that the thermal residual stresses, which arise from the thermal shrinkage mismatch between solid fiber and melt resin during thermal curing, are the primarily responsible for the negative intercepts. The values in Figure 5.6(a) range between - 0.05 and - 0.17 N, therefore indicating that a slight thermal stresses arise after the curing step.
Figure 5.6b shows the IFSS values for both neat and PCL-coated uGF. Specifically, uGF exhibits an interfacial adhesion strength of 43.9 ± 8.5 MPa with epoxy. Overall, the adhesion remains nearly constant even after the application of PCL, without showing an effect from the coating velocity. Notably, there is a slight 16% enhancement observed for 2500_uGF. This result confirms the favourable interaction of the PCL interphase within the glass/epoxy system.

Evaluation of the self-healing properties
Microdebonding curves for pristine and healed microcomposites, involving the same droplets taken from identical filaments for each fiber type, are depicted in Figure 5.7(a-d). These curves show the relationship between the load applied to individual droplets and the resultant interfacial displacement. The curves represent the typical behaviour of epoxy droplets under shear stress, starting from an initial linear region representing the elastic behaviour. Then, a peak of load indicates a localized interface damage, followed by a plateau that represents the frictional contributions along the fiber length.
After the healing process, the shape of the load-displacement curve remain consistent, which means that the healing occurred efficiently the frictional plateau has been recovered. However, in the case of neat uGF sample (Figure 5.7a), a minimal increase in the load is observed after healing, which is necessary to overcome the static and dynamic friction and set the microdrop in motion. After this

increase, the frictional plateau is reached again. Therefore, the absence of any load that exceeds the frictional plateau confirms the absence of healing in the uGF sample.

In Figure 5.8(a-c), the representative linear regression lines that relate the maximum load applied to individual droplets against the respective embedded areas are shown. Samples are designated accompanied by letters (I) H.E., (II) H.E., (III) H.E. that correspond to the multiple self-healing steps to which have been subjected. Figure 5.8d shows the mean healing efficiency values (H.E.) for each sample.

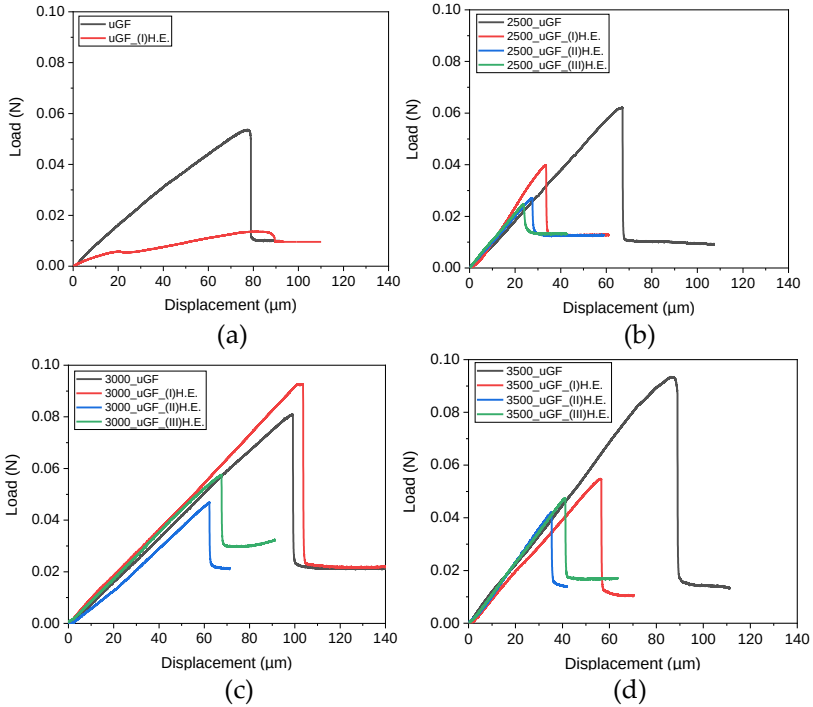

Figure 5.7 Representative load-displacement curves from microdebonding test for virgin and healed microcomposites: (a) uGF, (b) 2500_uGF, (c) 3000_uGF, (d) 3500_uGF.

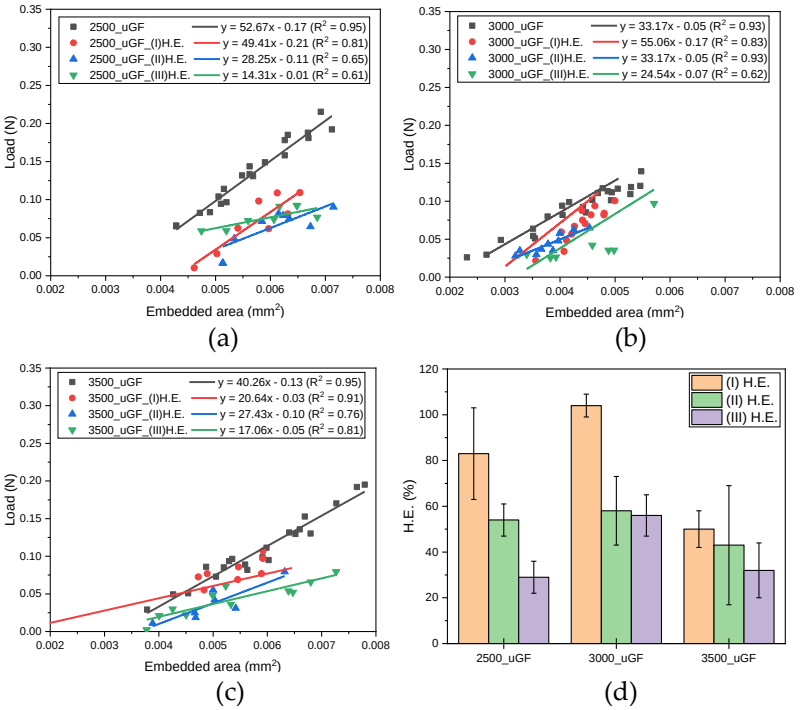

Figure 5.8 Linear regressions of the maximum force applied to individual droplets and the embedded areas from microdebonding tests, (a) 2500_uGF, (b) 3000_uGF, (c) 3500_uGF, (d) healing efficiency values for three consecutive debonding/healing cycles.

From Figure 5.8(a-c), it is possible to see that generally the data points have a linear fitting with R^2 values varying from approximatively 0.95 for the pristine interface (subjected to an initial debonding and no healing steps), to 0.70 for three time-debonded interface (subjected to four debondings alternated by three healings). The progressive decrease in R^2 values suggests that the adhesion is not consistent along the entire fiber length. The increased scatter is always one of the observed phenomena in microdebonding since various droplets and locations on the fiber could undergo slightly

different aging processes [103]. This is particularly true in the case of healed droplets that are subjected to multiple thermal treatments for self-healing. This phenomenon reflects also in the thermal components (expressed as q-values in Figure 5.8(a-c)) that are clearly altered, possibly due to the thermal healing. Therefore, these aspects can be the reasons of the observed decrease of the self-healing efficiency upon repeated healings (Figure 5.8d). Indeed, after one cycle of debonding/healing, the self-healing efficiency exhibited an impressive 100% in the case of sample 3000_uGF_(I)H.E., meaning that a complete restoration of to the original structural state has been reached. Lower, but still excellent, self-healing efficiencies are obtained for 2500_uGF_(I)H.E. (83%) and 3500_uGF_(I)H.E. (50%). However, when the interphase is subjected to subsequent debonding/healing cycles, the self-healing efficiency exhibits a gradual decrease, ultimately approaching about 30% after three cycles for the sample 2500_uGF_(III)H.E..

The SEM images of the polymeric coating taken before and after the first healing step (Figure 5.9) demonstrates that the morphological aspect of the coating is not subjected to substantial variation due to thermal mending, since PCL is thermoplastic.

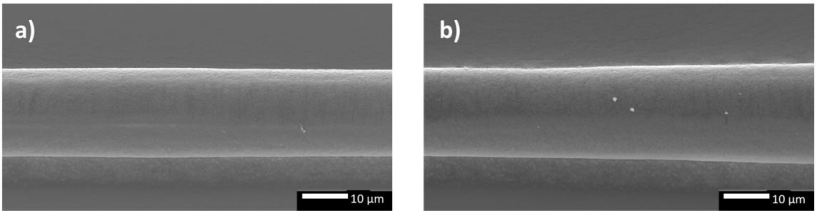

Figure 5.9 Morphological aspect of PCL coating on uGF: (a) 2500_uGF, (b) 2500_uGF_(I)H.E.

This was also verified by AFM (Figure 5.10) where no substantial alterations of the surface topography of coated fibers is observed as a function of the number of healing cycles.

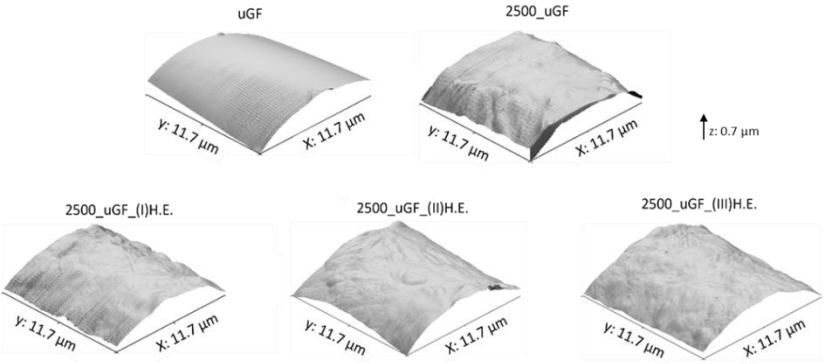

Figure 5.10 Example of 3D-AFM images for neat uGF and 2500_uGF subjected to three consecutive debonding/healing events.

The uGF surface appears clean and smooth, since no sizing and contaminations are present. The application of the PCL coating causes an evident increase of surface roughness, which is maintained after the consecutive thermal healing treatments. In Figure 5.11a, the values of arithmetical mean roughness (R_a) and root-mean-square roughness (R_q), measured in the axial direction of the fibers, are reported together with a comparison of the profile height of neat and 2500_uGF samples (Figure 5.11b). In Figure 5.12a, the values of R_a and R_q, measured in the orthogonal direction of the fibers, are reported together with a comparison of the profile height of neat and 2500_uGF samples (Figure 5.12b).

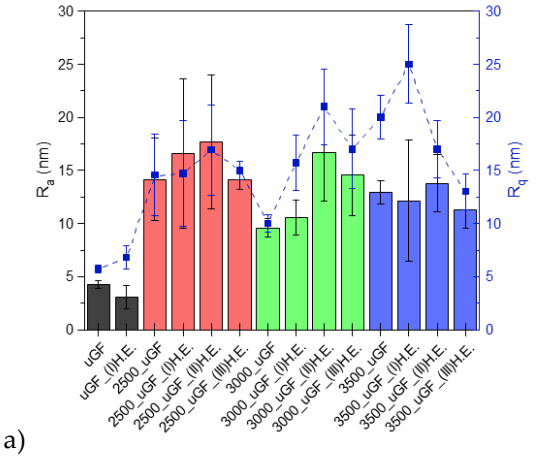

Figure 5.11 (a) Values of arithmetical mean roughness (R_a) and root-mean-square roughness (R_q), measured in the axial direction of the fibers, (b) example of the profile height for neat and 2500_uGF samples.

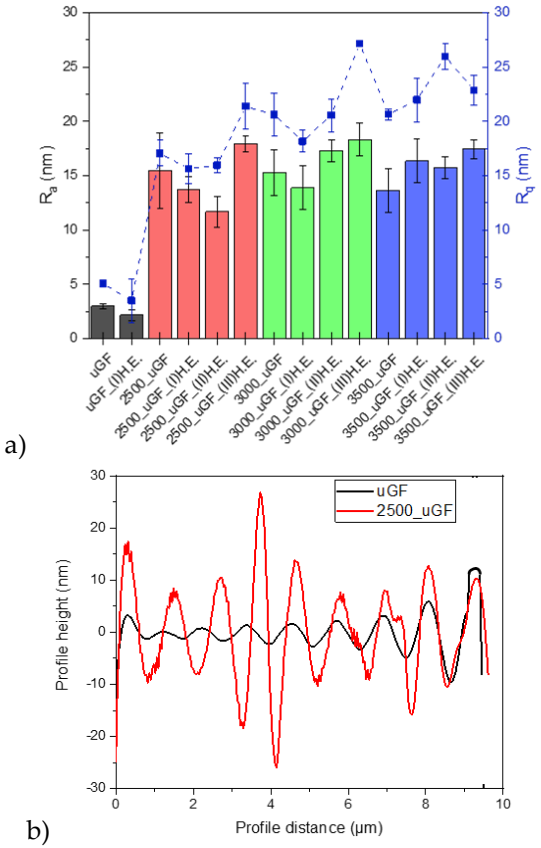

Figure 5.12 (a) Values of arithmetical mean roughness (R_a) and root-mean-square roughness (R_q), measured in the orthogonal direction of the fibers, (b) example of the profile height for neat and 2500_uGF samples.

Neat uGF shows mean R_a value equal to (4.2 ± 0.3) nm and mean R_q value equal to (5.7 ± 0.3) nm in axial direction. Similar results are obtained in the orthogonal direction, meaning that the roughness of the fiber surface is consistent independently from the measured direction. The application of the PCL coating improves the R_a value

to (14.1 ± 3.7) nm for 2500_uGF, to (9.5 ± 0.8) nm for 3000_uGF and to (12.0 ± 1.1)nm for 3500_uGF, and R_q values to (14.5 ± 3.8) nm for 2500_uGF, to (10.0 ± 0.8) nm for 3000_uGF and to (20.1 ± 1.1) nm for 3500_uGF. Again, similar results of R_a and R_q are obtained orthogonally, excluding a preferential dependence of the coating roughness from the direction of the coating process. The consecutive, thermally activated healing cycles do not significantly affect the R_a and R_q values in both test directions, which means that surface roughness is consistently maintained after consecutive thermal treatments. Furthermore, from Figure 5.11b and Figure 5.12b, it can be seen that the roughness profile of the coated fibres appears as a complex surface, with sharper peaks and reduced peak width, which slightly increase the area of contact between matrix and reinforcement. Therefore, the evolution of the roughness profile of the PCL coating after multiple cycles does not explain the decrease in multiple healing efficiency.

In addition, any thermal degradation of neat PCL was investigated via thermogravimetric analysis (TGA) (Figure 5.13), where three isothermal treatments at 80 °C for 30 min, as simulation of the thermal behaviour of the coating due to consecutive thermal healing cycles are reported.

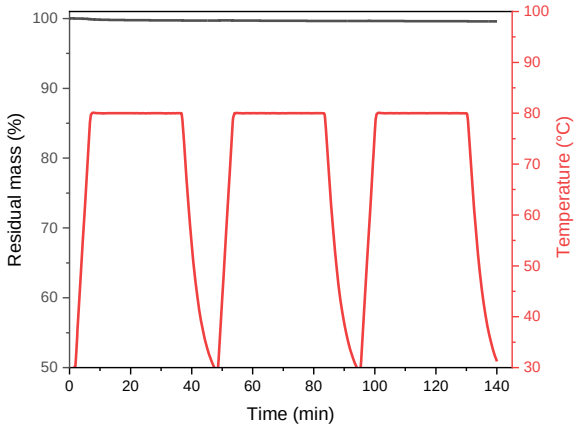

Figure 5.13 Thermogravimetric analysis (TGA) on neat PCL. Three isothermal treatments at 80 °C for 30 min, as simulation of the thermal behaviour of the coating due to consecutive thermal healings have been performed.

Therefore, the inconsistency of adhesion and healing efficiency was considered not to be related to the evolution (morphological and/or thermal) of the coating upon thermal healing.

Instead, a progressive modification of the matrix droplet shape is observed after multiple healing cycles, probably related to the decrease of healing efficiency. In Figure 5.14, the optical microscope images of the evolution of the shape of the epoxy droplets after 3 cycles of debonding and healing is reported.

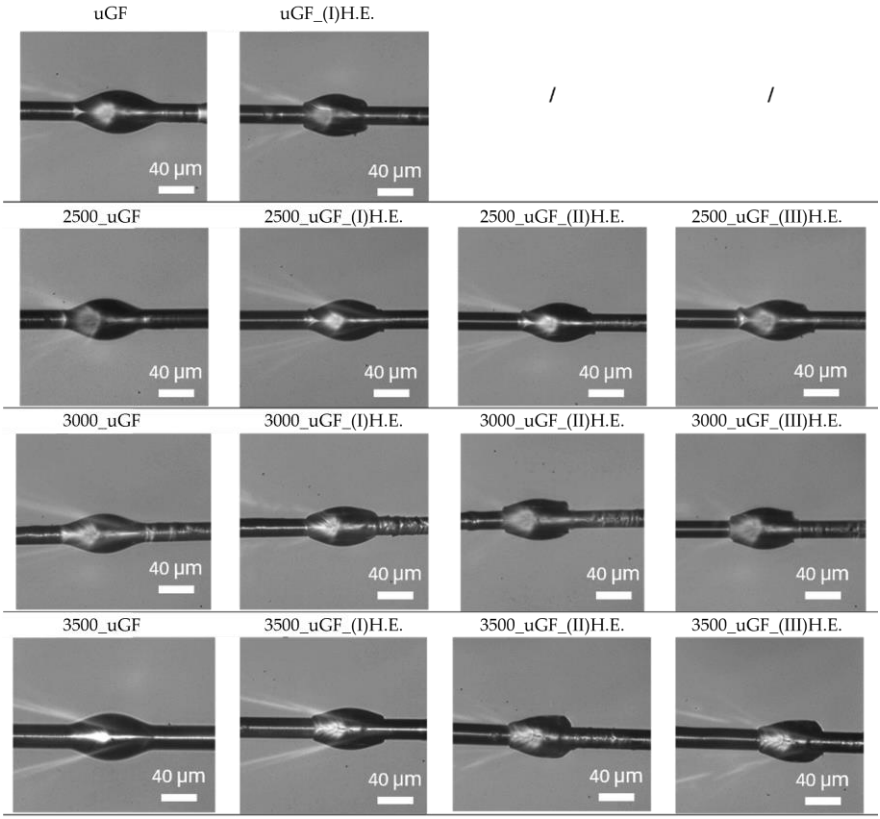

Figure 5.14 Optical images of the evolution of the shape of epoxy droplet after 3 cycles of debonding and healing.

It can be observed that the shape of the epoxy droplet is quite maintained after repeated thermal processes. However, the lack of the meniscus after first debonding is evident. As explained by Ash et al. [104], the meniscus is formed along the length of the fiber and it increases the embedded length. During microdebonding, meniscus failure can occur due to the contact with the blades, resulting in a portion of the polymer droplet remaining adhered to the fiber. This phenomenon may alter the stress state near the fiber/droplet contact

point and therefore the resulting values of IFSS. Hence, it is possible that a cumulative effect may arise, ultimately compromising adhesion values after multiple cycles.
Made all of these considerations, for the scope of this preliminary study of PCL self-healing interphase, adhesion values with R^2 higher than 0.70 were considered as representative. Indeed, the study demonstrates the intricate relation between the number of curing cycles and the extent to which a material can autonomously mend itself.
Therefore, a future finite element method (FEM) investigation will be extensively dedicated in a future work to the study of the role played by the meniscus on repeated debonding/healing cycles.

5.1.3 Conclusions

In this study, the deposition of a PCL continuous coating allowed to tailor the interphase properties in epoxy/glass microcomposites, to improve the potential of fiber-reinforced composites from a mechanical point of view. The fluid coating theory was followed to coat the surface of the fibers. Scanning electron microscopy and optical microscopy analyses revealed that a well-applied polymer coating was progressively was formed on the fiber surface as a function of the coating speed, with in a uniform and smooth appearance. The apparent interfacial shear strength (IFSS) was assessed by microdebonding tests from the linear regression of the maximum load applied to individual epoxy droplets vs. their corresponding embedded area. An increase up to 16% in matrix/fiber adhesion was obtained compared to neat interphase, confirming the positive interaction of the PCL with the epoxy/glass system. The healing efficiency was calculated as the ratio of IFSS before and after the thermal mending and up to three consecutive debonding/healing cycles.
After the first cycle of debonding/healing, the self-healing efficiency exhibited an impressive value of 100% in the case of sample 3000_uGF_(I)H.E., indicating a complete recovery of the original

structural state. Lower but still excellent self-healing efficiencies were obtained for 2500_uGF_(I)H.E. (83%) and 3500_uGF_(I)H.E. (50%) fibers. However, as the interphase was subjected to subsequent debonding/healing cycles, the self-healing efficiency exhibited a gradual decline, ultimately approaching about 30% after three cycles for the same sample. However, a progressive modification of the matrix droplet meniscus was observed after multiple healing cycles, and this phenomenon may have altered the stress state near the fiber/droplet contact point and therefore the resulting IFSS values. A future finite element method (FEM) investigation will be extensively dedicated to the study of the role played by the meniscus on repeated debonding/healing cycles.

5.2 Electrophoretic deposition of a PCL nanocoating on glass and carbon fibers

Published papers:

Simonini, L.; Mahmood, H.; Dorigato, A.; Pegoretti, A. Evaluation of self-healing capability of a polycaprolactone interphase in epoxy/glass composites. *Composites Part A: Applied Science and Manufacturing* **2023**, *169*, 107539-107548.

Simonini, L.; Canale, R.; Mahmood, H.; Dorigato, A.; Pegoretti, A. Multifunctional epoxy/carbon composites with a fully reparable interface. *Polymer Composites* **2024**, *45*, 2558-2568.

The aim of this study was to coat the glass and the carbon fibers with a self-healing polycaprolactone (PCL) coating in order to provide interfacial self-healing capability. In contrast to Chapter 5.1, where the PCL film was applied to individual fiber filaments, Chapter 5.2 focuses on a method involving the simultaneous coating of fiber bundles. At first, the fibers were dip-coated in the PCL liquid solution, resulting in a non-uniform PCL mass around the bundle, as observed through SEM analysis, which was not suitable for the intended application. Subsequently, a different approach was pursued, employing nanoparticles dispersed in a water solution, forming a continuous nanostructured layer. Initially, two coating techniques were compared: dip-coating and electrophoretic deposition (EPD). SEM analysis revealed that the dip-coating process required a higher concentration of nano-PCL in the solution compared to EPD. The application of an electrical field during EPD provided kinetic energy to the charged particles, forcing them to deposit on the fiber surface, while dip coating involved settling without energy. Furthermore, EPD allowed for better control over the amount of deposited PCL, resulting in higher deposition quality. Consequently, the deposition of PCL nanoparticles using EPD was

selected as the coating methodology for both glass and carbon fibers. For carbon fibers, both EPD and self-healing were facilitated by their electrical conductivity.
This section presents the materials and techniques used to prepare and characterize the samples. A detailed description of these methods has already been provided in Chapter 3.

5.2.1 Materials and methods

5.2.1.1 Materials

The materials employed for the preparation of the samples are listed in Table 5.3. A more detailed description can be found in Section 3.1.

Table 5.3 List of materials employed for the preparation of microcomposites.

Constituent	Label	Material
Matrix	EP-1	Epoxy matrix (EC 157, W 342)
Fiber	sGF and uGF	Sized and unsized glass fiber (Windstrand®)
	CF	Carbon fibers (GC 201 U TFX)
Coating material	PCL-1 and PCL-2	Poly (ϵ-caprolactone)

Additionally, poly(vinyl alcohol) (PVA) (density = 1.2 g/cm^3, M_w = 50000 g/mol) and Polysorbate 80 (Tween® 80) (density = 1.1 g/cm^3, pH = 5.5 – 7.5) were provided by Sigma Aldrich Co. (Saint Louis, Missouri, USA) as a powder and a viscous liquid, respectively, and were used as stabilizers in the preparation of PCL nanoparticles.

5.2.1.2 Sample preparation

Preparation of PCL nanoparticles in solution

A solvent displacement technique was employed to achieve a well-dispersed state of PCL nanoparticles within water [105]. PCL was dissolved in acetone for 40 minutes and stirred at 600 rpm at room temperature. In a separate container, PVA and Tween® 80 were

dissolved in water under identical experimental conditions. Subsequently, the PCL-acetone solution was carefully added drop by drop to the stabilizer-water solution employing a Harvard 11 Plus injector (Harvard Apparatus, USA) under continuous agitation. The resulting solution was then transferred to a rotating apparatus (Buchi R-114 rotavapor) equipped with a water bath (Buchi B-480) (Buchi, Switzerland), for acetone evaporation, maintained at 30 °C for 45 minutes under 200 mbar. This process led to the formation of a PCL nanoparticle dispersion in water, subsequently subjected to 15 minutes of ultrasonication at room temperature using a FALC (Shenzhen, China) ultrasonic bath to prevent any potential agglomeration. Various parameters such as PCL concentration, stabilizer concentration, water content, and injection rate were systematically adjusted to optimize the PCL nanoparticle morphology. In total, six distinct solutions were prepared, and their respective parameters are summarized in Table 5.4. For each solution, the progressive change of parameters is highlighted in yellow.

Table 5.4 Composition of the obtained PCL solutions (SOL1-6).

	SOL1	SOL2	SOL3	SOL4	SOL5	SOL6
PCL (mg/ml)	4.0	4.0	4.0	4.0	2.0	4.0
Acetone (ml)	12.5	12.5	12.5	12.5	12.5	12.5
Tween® 80 (mg/ml)	21.2	21.2	10.6	21.2	21.2	21.2
Milli-Q water (ml)	100	100	100	150	100	100
PVA (mg/ml)	2.5	5.0	2.5	2.5	2.5	2.5
Stirring speed (rpm)	600	600	600	600	600	600
Injection rate (ml/min)	2.5	2.5	2.5	2.5	2.5	1.0

The most effective configuration to achieve finely dispersed small PCL nanoparticles was found to be SOL1 for PCL-1 and SOL6 for

PCL-2. Consequently, SOL1 and SOL6 were chosen to prepare the self-healing coatings on glass and carbon fibers, respectively. PCL nanoparticles were diluted with deionized water to create three distinct solutions containing PCL nanoparticles at varying concentrations (i.e., 0.01 wt%, 0.03 wt%, 0.05 wt%).

Coating of fibers

A poly(methyl methacrylate) (PMMA) custom-built electrophoretic deposition (EPD) setup (Figure 5.15) was employed for depositing PCL nanoparticles onto the surface of GFs (Figure 5.15a) and CFs (Figure 5.15b).

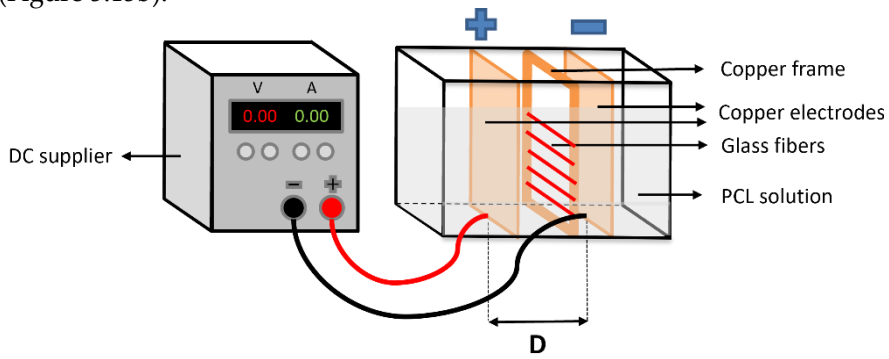

(a)

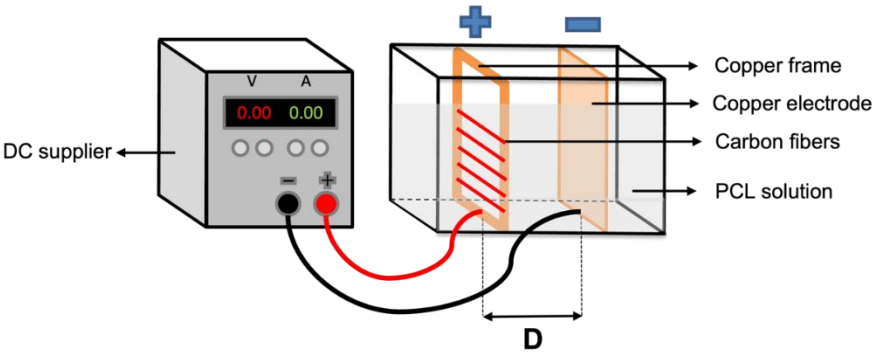

(b)

Figure 5.15 Schematic representation of EPD setup, (a) for GF and (b) for CF coating with PCL nanoparticles.

In the case of GFs, a DC power supplier (ISO-tech IPS303DD, Germany) was connected to two copper electrodes (anode and cathode), while GFs were fixed on a metallic support placed at 10 mm distance from both the electrodes. In the case of CFs, the DC power supplier was connected to a copper electrode (anode) and to a copper support to which bundles of CFs were fixed (acting like the cathode). PCL solutions at different concentrations were poured into the bath progressively. The application of different electric voltage values (5, 10, and 30 V) induced the negatively charged nanoparticles to migrate towards the positive electrode, facilitating their adhesion onto the fibers and the subsequent formation of a coating. The deposition duration was set at 30, 60 and 120 seconds, knowing that the deposition rate decreases for a constant applied electrical field over times, eventually reaching a plateau [106]. To ensure PCL deposition on both sides of the fiber bundles, the voltage heads were reversed and EPD was carried out for another same period of time. Note that the position of the fibers in the bundle during the deposition process may affected the homogeneity of the coating since the innermost fibers could be less coated than the outermost fibers. A possibility could be the use of bundles with low title.

Subsequently, the coated fibers were air-dried overnight at room temperature under vacuum.
The list of prepared sample is presented in Table 5.5.

Table 5.5 List of prepared coated fibers.

	PCL (wt%)	ΔV (V)	Time (s)
Glass fibers			
sGF / uGF	-	-	-
(s/u)GF_0.01_5_60	0.01	5	60
(s/u)GF_0.01_10_60	0.01	10	60
(s/u)GF_0.01_30_60	0.01	30	60
(s/u)GF_0.03_5_60	0.03	5	60
(s/u)GF_0.03_10_60	0.03	10	60
(s/u)GF_0.03_30_60	0.03	30	60
(s/u)GF_0.05_5_60	0.05	5	60
(s/u)GF_0.05_10_60	0.05	10	60
(s/u)GF_0.05_30_60	0.05	30	60
(s/u)GF_0.03_30_30	0.03	30	30
(s/u)GF_0.03_30_60	0.03	30	60
(s/u)GF_0.03_30_120	0.03	30	120
Carbon fibers			
U_CF	-	-	-
C_CF	0.03	30	60

5.2.1.3 Experimental techniques

The techniques used to characterized the prepared samples are listed in Table 5.6. A more detailed description can be found in Section 3.2.

Table 5.6 Experimental techniques.

Technique	Parameters	Aim
SEM	Section 3.2.1.2	To observe the morphology of nanoparticles and coated/uncoated Gf and CF
Zeta potential (ζ)	Beckman Coulter DelsaNano AT 0.1 M HCl	To analyze the electrical potential of nanoparticles
TGA	Section 3.2.4	To determine the amount of PCL deposited on fibers
Microdebonding	Section 3.2.5	To determine the interfacial shear strength (IFSS) and healing efficiency (H.E.)
Electrical conductivity	Section 3.2.6.2	To determine the self-healing temperature for CF

5.2.2 Results and discussion

5.2.2.1 Morphological characterization

Morphological characterization of PCL nanoparticles

The morphology of PCL nanoparticles derived from SOL1 to SOL6 are depicted in Figure 5.16. Additionally, their statistical size distribution, represented by a Gaussian relative frequency function, and the average nanoparticle diameter (d), are presented.

Figure 5.16 demonstrates that the solvent-displacement approach is a suitable method for the preparation of well-dispersed, uniform PCL nanoparticles. However, SOL3 and SOL4 setups exhibit unsatisfactory morphology due to high PCL nanoparticle agglomeration, likely attributed to the lower concentration of the stabilizer (Tween® 80) compared to PCL, and excessive dilution of the solution. For these experimental setups, the determination of a mean nanoparticle size is unfeasible. In comparison, from SOL1 (d = 333 ± 11 nm) and SOL2 (d = 457 ± 10 nm), it is evident that doubling the PVA content results in larger nanoparticles. This phenomenon is

explained by Badri et al. [105], who discovered that an elevated PVA content significantly increases particle size, as an excess of PVA tends to accumulate on the nanoparticle surface, therefore increasing their ultimate size. On the other hand, SOL5 displays a particle size comparable to SOL1, indicating that the PCL concentration in the solution does not significantly affect the final particle size. Further comparison between SOL1 and SOL6 setups suggests that a slower injection rate forms smaller particles, given that the PCL-acetone solution is gradually introduced to the stabilizers, allowing sufficient time for PCL to form individual particles. As explained by Besra et al. [106], larger particles have a propensity to settle during EPD due to gravitational sedimentation. Hence, it can be said that, for the purpose of this study, smaller particles are preferable to facilitate their movement within the solution during the EPD process, resulting in a higher quality coating. Consequently, the SOL6 setup, yielding PCL nanoparticles with a mean size of d = 233 ± 67 nm, has been identified as the optimal configuration. The Zeta Potential (ζ) values of SOL1 and SOL6 solutions at different concentrations are reported in Table 5.7.

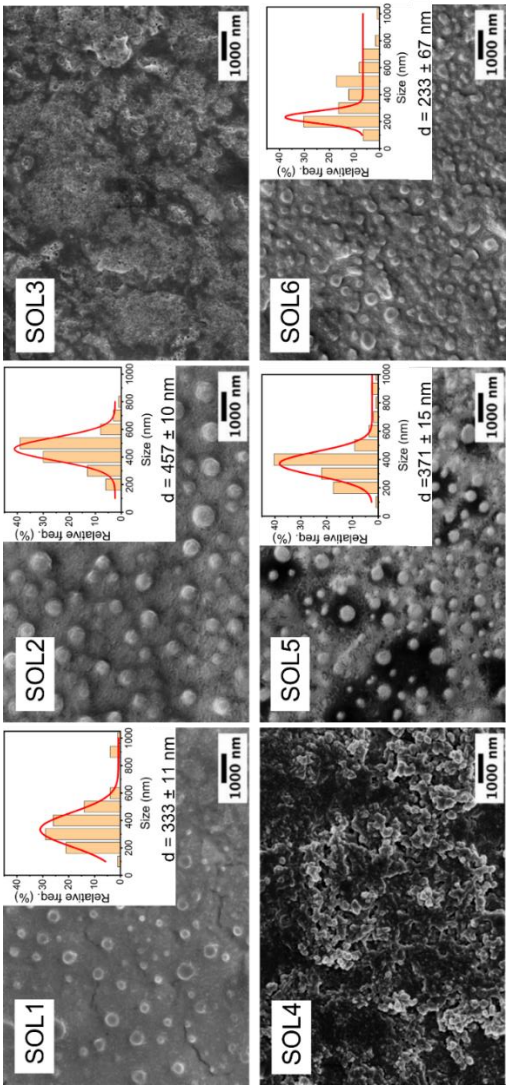

Figure 5.16 SEM images of PCL nanoparticles with the size frequency distribution and mean value of diameter (SOL1-6).

Table 5.7 Zeta potential values of SOL1 and SOL6.

PCL concentration (wt%)	ζ (mV)
SOL1	
0.01	-16.0 ± 0.5
0.03	-15.4 ± 1.7
0.05	-11.4 ± 1.4
SOL6	
0.01	-18.9 ± 1.1
0.03	-12.3 ± 1.9
0.05	-7.8 ± 0.8

The PCL nanoparticles exhibit a negative surface charge, for both SOL1 and SOL6, suggesting a potential particle instability [106,107]. A higher concentration reduces the stability, whose phenomenon is consistent with the literature [108]. The negative zeta potential indicates the direction of nanoparticle movement in the solution towards the positive electrode during electrophoretic deposition (EPD).

Morphological characterization of glass fibers

Figure 5.17 shows the SEM images of the coated and uncoated glass fibers (sGF and uGF). It can be seen that by increasing both the solution concentration and the applied voltage, the deposition of PCL nanoparticles on GF increases. The deposition results consistent and homogeneous by using a potential of 30 V and a solution concentration of 0.03 wt%. Figure 5.18 shows the effect of the deposition time on the morphology of the fibers. It can be noticed that the longer the deposition time, the worse the homogeneity of the PCL coating. The deposition results compact and homogeneous by setting a deposition time equal to 60 s for each bundles side (total deposition time = 120 s). Note that this value of time prevents the oxidation of the copper electrodes which was seen to begin after 150

s of deposition (at $\Delta V = 30$ V). The oxidation also promoted a change of the solution colour from matt white to green, because of the release of copper ions. This phenomenon is more evident by increasing the deposition duration.

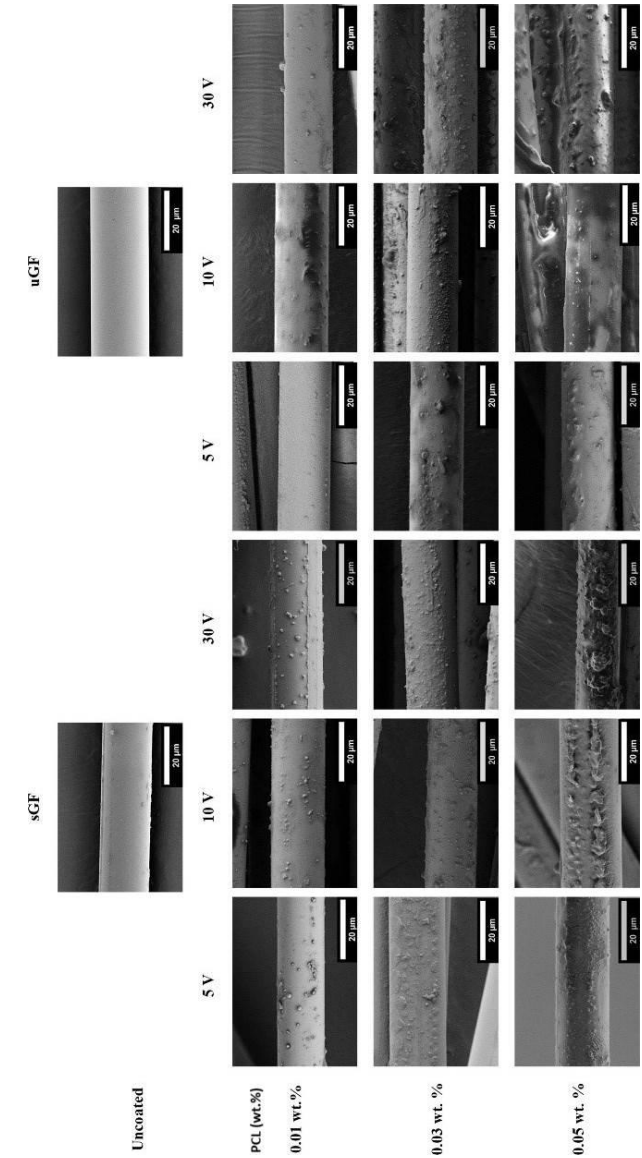

Figure 5.17 SEM images of uncoated and PCL GFs, by varying the PCL solution concentration and applied voltage.

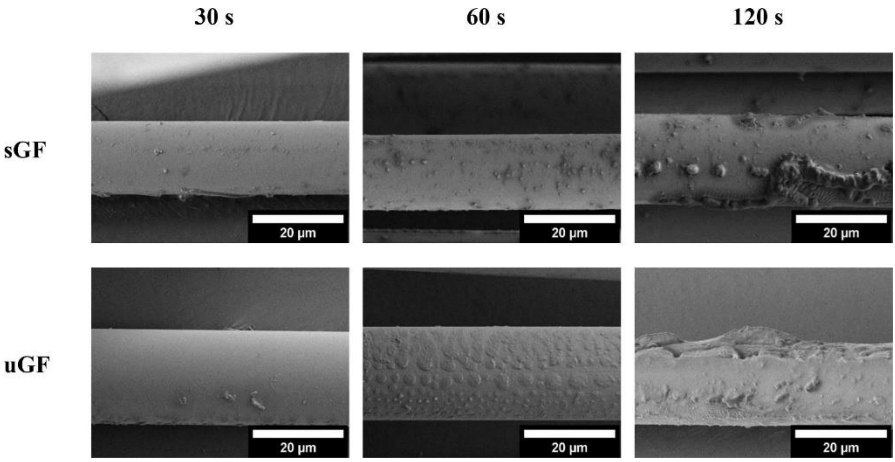

Figure 5.18 SEM images of uncoated and PCL GFs, by varying deposition time.

The amount of deposition was evaluated by a TGA analysis. In Figure 5.19(a,b) representative TGA thermograms for both sized and unsized GFs are reported.

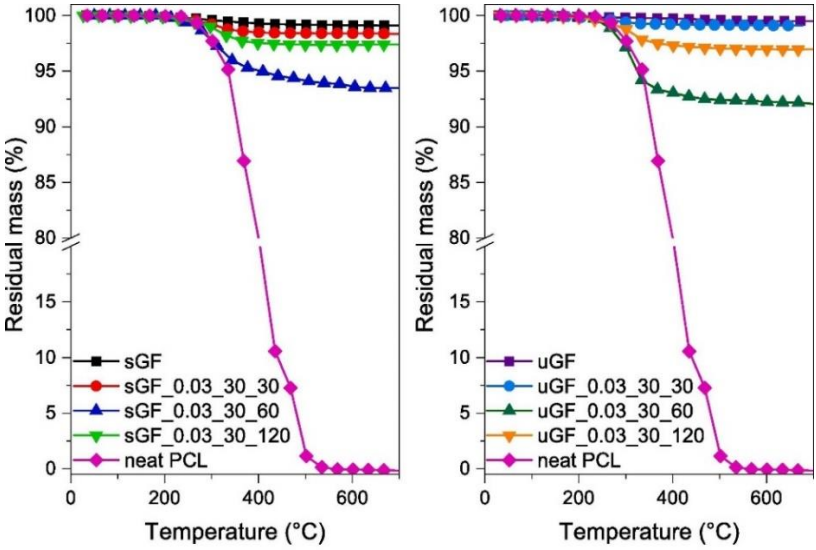

Figure 5.19 TGA thermograms of neat PCL, uncoated and PCL coated fibers as a function of the deposition time, (a) sGF fibers, (b) uGF fibers.

In Table 5.8, the values of residual mass at 700 °C for each sample are reported.

Table 5.8 Values of residual mass at 700 °C (m_{700}) from TGA tests on the prepared fibers.

Samples	m_{700} (%)	Samples	m_{700} (%)
sGF	99.1	sGF	99.5
sGF_0.03_30_30	98.4	sGF_0.03_30_30	99.1
sGF_0.03_30_60	93.5	sGF_0.03_30_60	92.1
sGF_0.03_30_120	97.4	sGF_0.03_30_120	97.0

A slight mass loss is measured for all the PCL coated fibers, which corresponds to the loss of the PCL coating, the silane coating (for the

sized fibers) and other superficial impurities. sGF_0.03_30_60 and uGF_0.03_30_60 have the highest mass loss (6.6 % and 7.9 % respectively). For longer EPD treatments (sGF_0.03_30_120 and uGF_0.03_30_120) a lower mass loss was obtained. This could be due to the fact that the longer the deposition time, the more nanoparticles are deposited on the fibers, hence forming a multilayer coating. The last layers may not be as well adherent to the fibers' surface as the first ones, causing their detachment.

Therefore, based on the SEM images and TGA analysis, a deposition time of 60 s (for both sides), a solution concentration of 0.03 wt% and an applied voltage of 30 V were selected as the best parameters to coat the glass fibers and to evaluate the interfacial self-healing capability of EP/GF composites through microdebonding tests.

Morphological characterization of carbon fibers

In Figure 5.20(a,b) the morphological aspect of the coated and uncoated CFs are presented, as a function of PCL weight concentration in solution (0.01, 0.03, and 0.05 wt%.) and the applied voltage (5, 10, and 30 V). A constant deposition time (of 60 s) was maintained for each bundle side. As it can be seen, the surface of uncoated CFs is rather smooth and regular. On the contrary, the surface of PCL-coated CFs is rough and irregular, due to the presence of the coating. The number of nanoparticles tends generally to increase with the PCL solution concentration, while it decreases with the applied voltage. As it can be observed, the highest PCL concentration (i.e., 0.05 wt%.) and the lowest applied voltage (i.e., 5 V) allow to obtain a rich deposition of nanoparticles. A possible reason could be that, at high voltage, the nanoparticles possess an elevated kinetic energy, that prevents them from efficiently anchoring on the CFs surface, thus affecting the integrity of the coating [106]. On the contrary, a lower voltage provides them the adequate speed to move in solution and to efficiently deposit on CFs, therefore forming a coating. Consequently, the optimized combination of PCL concentration (0.05 wt%.) and applied voltage (5

V) results in the best coating for the purpose of this work, i.e., an abundant PCL deposition on CFs to fully heal the debonded fiber/matrix interface. By using ImageJ 1.53a software, the coating thickness obtained in these conditions is estimated equal to 1.1 ± 0.5 μm.

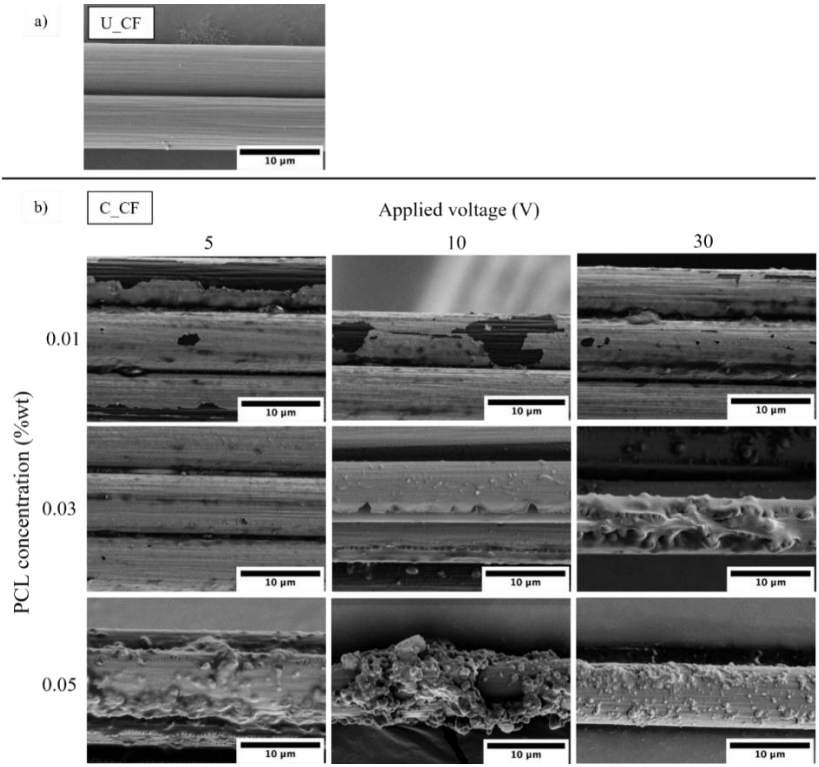

Figure 5.20 SEM images of (a) U_CF and (b) C_CF as a function of PCL solution concentration and the applied voltage (deposition time = 60 s).

5.2.2.2 Mechanical characterization

Evaluation of the IFSS and self-healing for glass fibers

In Figure 5.21(a,b), the representative load–displacement curves obtained from microdebonding tests on the uncoated and PCL coated glass fibers are reported and compared with the curves relative to the healed and control samples (denoted by terms "H" and "control" in the sample code, respectively). In Figure 5.21a, the epoxy drop on the uncoated sGF debonds at load of 0.50 N, then slides on the fiber with a frictional resistance of 0.15 N. This frictional plateau is important since confirms the debonding of the epoxy drop. After the thermal mending procedure, the same epoxy drop debonds at a force of approximately 0.20 N, which is lower than the debonding force for the virgin test. Partial recovery of the virgin debonding force is attributed to thermal mending of epoxy with the fiber on account of additional cross-linking via residual functionality within the epoxy matrix. In the case of sGF_0.03_30_60, the epoxy drop debonds at load even higher than uncoated sGF sample (approx. 0.58 N) which indicates a higher adhesion interfacial bonding between epoxy and the fiber. This is another positive aspect verified by the coating of PCL nanoparticles on the fibers.

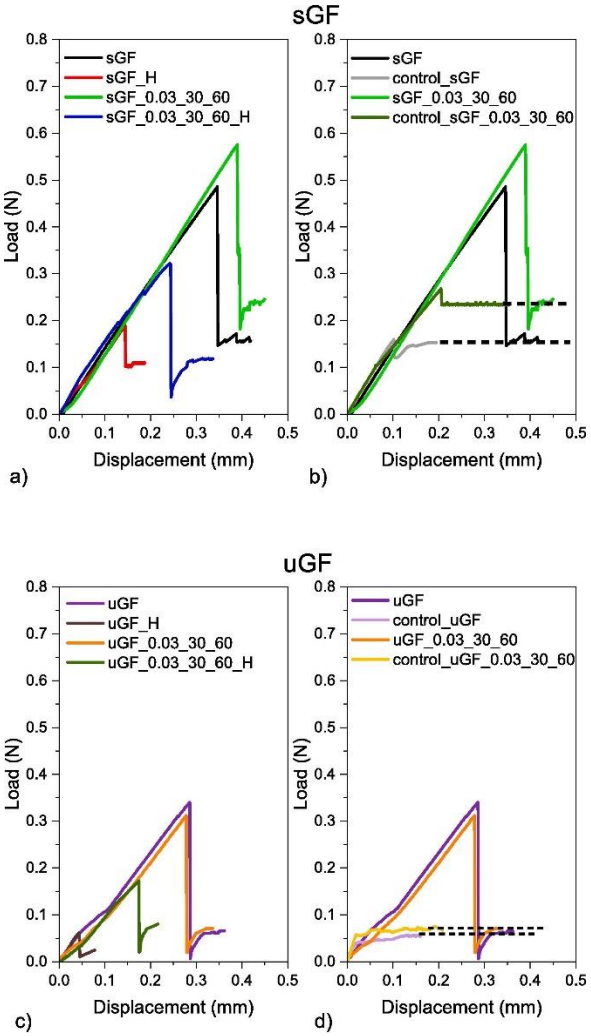

Figure 5.21 Comparison of load-displacement curves from microdebonding tests on the uncoated fibers, PCL coated fibers and the corresponding healed and control samples for (a, b) sGF and (c, d) uGF.

After healing, the load recovered is 0.32 N, which is higher compared to healed uncoated sGF fibers. The higher load recovery is clearly a verification of the healing capability at interfacial level by the PCL healing agent. Even after the confirmation of this damage recovery, it was worthwhile to confirm any healing mechanism that might be acting other than the thermal mending procedure employed. Hence the control tests of virgin specimens were also performed by post-debonding run at room temperature after a 60-minute waiting time. From Figure 5.21b, it can be observed that the control samples only exhibit the frictional force after 60 min from initial testing. Particularly, the control specimens of sGF-type of fibers show an initial peak of load corresponding to the static friction to move the microdrop. The same is true for fibers coated with PCL nanoparticles i.e., sGF_0.03_30_60. Hence the absence of any load higher than the frictional plateau confirms the absence of healing other than thermal mending performed on the samples.

On the other hand, in the case of samples involving uGF (Figure 5.21c), a similar behaviour of debonding/healing is found. The only difference is with the debonding force of virgin specimens involving PCL coating, which is similar to the uncoated uGF samples. Overall, also for uGF-type of fibers, the healing capability of PCL as an interphase between epoxy and GF is confirmed by microdebonding tests. The verification of the healing mechanism was also carried out by the post-debonding waiting time of 60 min. It can be seen from Figure 5.21d that the control samples of uGF-type fibers only show a frictional plateau with loads corresponding to the frictional plateau of the original virgin specimens. More importantly, there is no peak load related to the static friction of the microdrop on the fiber. It may be concluded that the presence of the silane coating implies greater compatibility with the matrix thus requiring a force to overcome the static friction at the interphase.

Carefully analysing the frictional plateau of the control samples and healed samples, it is also observed that for control samples the resulting frictional loads are higher compared to the healed samples.

This behaviour can be explained by the different morphology of the coating before and after the thermal treatment. An example of SEM images of the resulting morphology of the PCL coating is reported in Figure 5.22. As expected, PCL melted during healing, therefore, passing from a rougher morphology to a film-like one, implying a lower frictional force during debonding.

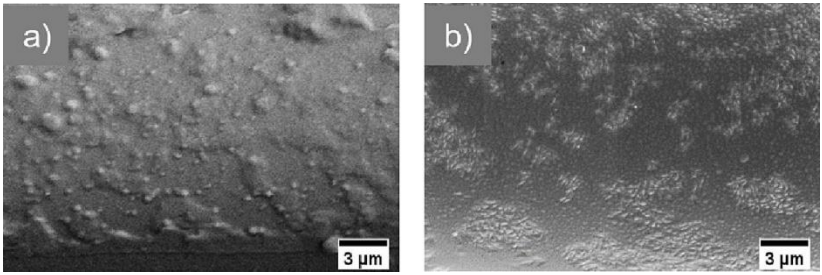

Figure 5.22 SEM morphology of PCL coating on fibers, (a) before healing and (b) after healing.

A comparison of the obtained IFSS values is reported in Figure 5.23a. These values were used for the calculation of the healing efficiency, according to the expressions reported in Equation 3.10 (see Figure 5.23b). For each sample, the mean and the standard deviation values are reported and calculated from ten tested specimens.

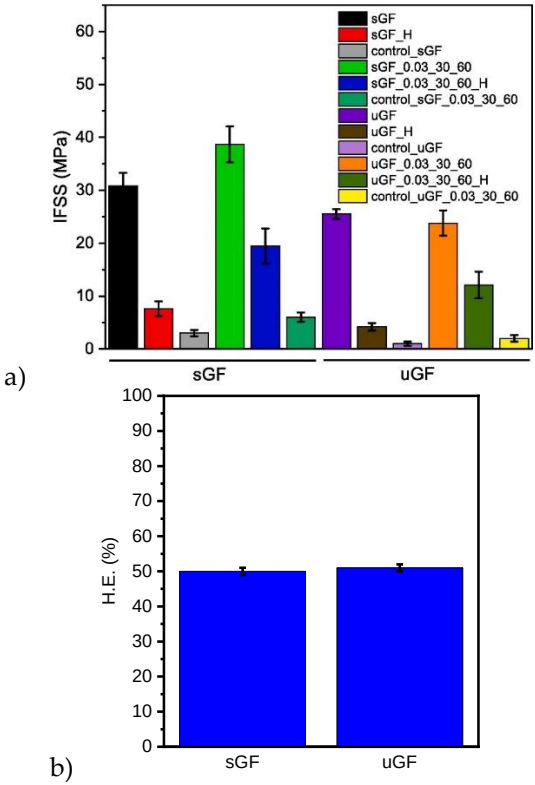

Figure 5.23 Results of microdebonding tests on uncoated fibers, PCL coated fibers and the corresponding healed and control samples. (a) IFSS values, (b) healing efficiency values (H.E.).

From Figure 5.23a, it is possible to see that the interfacial adhesion value of sGF is higher than uGF, due to the presence of the sizing agent. The IFSS values of the corresponding PCL coated samples (sGF_0.03_30_60 and uGF_0.03_30_60, respectively) demonstrate that the presence of the PCL interphase provides a positive effect in terms of interfacial shear strength in the case of sGF (+26 %), while no significant modifications can be noticed for uGF. This indicates that the PCL interphase has a positive interaction with the surface

sizing applied on GFs. As it could be expected, the IFSS values of sGF_H and uGF_H are rather low, indicating a limited interfacial strength recovery without the PCL interphase. Once PCL nanoparticles are deposited on the surface of GF (with or without the sizing agent), a substantial recovery of the IFSS can be observed. The calculation of the healing efficiency (see Figure 5.23b) demonstrates that the PCL interphase provides an IFSS recovery of 50 % upon thermal healing for sGF, and 51 % for uGF. In this case, the presence of the sizing agent does not seem to substantially influence the overall healing capability of these systems.
On the other hand, also the contribution played by the residual curing of the epoxy resin during the healing process should be considered. sGF_H and uGF_H samples showed respectively 24.7 % and 16.5 % recovery of the adhesion properties, indicating that also the residual curing of the matrix contributed to the interfacial healing process. This contribution is stronger in the case of sGF_H than uGF_H, probably because the sizing agent can physically (or chemically) interact with the epoxy resin.

Evaluation of the interfacial shear strength and self-healing for carbon fibers
Figure 5.24 shows the evolution of the surface temperature of a single CF during Joule heating as a function of time and voltage. Tests were chosen to last 15 seconds to efficiently heal the interface by Joule heating heating.

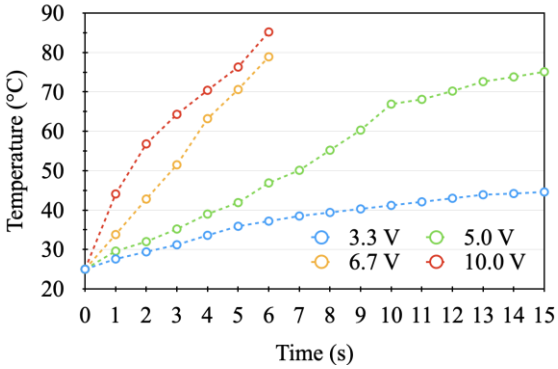

Figure 5.24 Evolution of the surface temperature of a single CF during Joule heating as a function of time and voltage.

From Figure 5.24 it is possible to notice that the temperature rises as the voltage and time increase. More specifically, at voltage levels of 6.7 V and 10.0 V a rapid increase in surface temperature leads to an undesired breakage of the filament after 6 seconds. On the other hand, for low values of voltage (3.3 V), a temperature equal to 45 °C is reached, not sufficient to trigger self-healing. In fact, it is reported in literature that the optimal temperature to activate self-healing in PCL must be close to 80 °C, in order to minimize the temperature difference between the glass transition of epoxy and the temperature of healing, therefore to maximize the healing efficiency, as explained by Karger-Kocsis [109] and by Wei et al. [110]. Therefore, 5.0 V is found to be an optimal voltage that allows to reach the desired healing temperature in the time frame necessary to activate the healing mechanism, without compromising the structural integrity of the fiber. An example of FESEM images of the resulting morphology of the PCL coating after healing is reported in Figure 5.25. As expected, PCL melted during healing, therefore, passing from a rougher morphology to a film-like one.

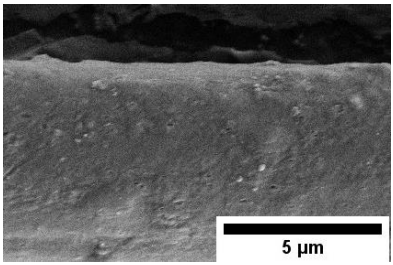

Figure 5.25 Morphology of the PCL coating after healing.

Micro-debonding tests allow to evaluate the interfacial shear strength (IFSS) of the uncoated CF (U_CF), PCL-coated (C_CF), and healed PCL-coated CF (H_CF), by using the expression reported in Equation 3.8. C_CF samples, after being tested, were healed applying a voltage of 5 V for about 15 seconds. In this way, H_CF samples were retested and the interfacial healing efficiency (H.E.) of the coating was calculated by using Equation 3.10. Moreover, the control tests were performed on virgin C_CF samples. Figure 5.26 shows a comparison of some representative load-displacement curves obtained from micro-debonding tests. The numerical results of IFSS, together with the healing efficiency values, are summarized in Table 5.9.

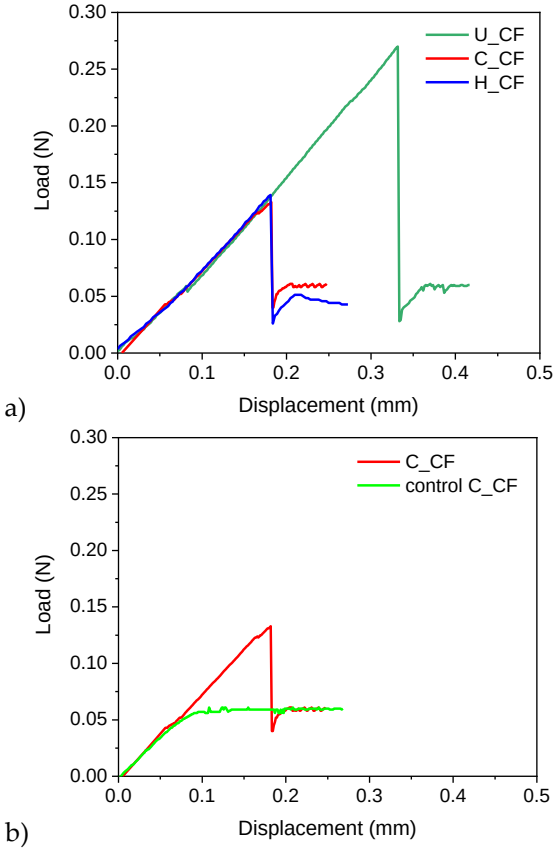

Figure 5.26 (a) Micro-debonding load-displacement curves of uncoated, coated and healed samples, and (b) post-damage responses for C_CF and its control sample.

U_CF samples are loaded till reaching the maximum value of force needed to have the full interfacial debonding. Then, they attain a frictional plateau of about 60 mN. C_CF shows a similar behaviour while testing, but a drastic reduction in maximum load is noticed (see Table 5.9). After the healing treatment, the samples are re-tested and full recovery of IFSS is achieved. As expected, the control C_CF

sample only recovers the frictional load of uncoated carbon fibers, without showing any recovery of initial adhesion properties. On the other hand, the H_CF sample shows a frictional recovery lower than control fibers (~ 40 mN).

A 60 % reduction of the IFSS value is observed for the PCL-coated CF with respect to the uncoated ones. This could be attributed to the relatively lower interfacial adhesion due to the abundant presence of the PCL coating [111,112]. However, an outstanding healing efficiency (about 100 %) can be reached thanks to the high quantity of PCL nanoparticles deposited on CFs, which efficiently provide a repair for the debonded interphase. In other words, the healing agent, deposited in the form of PCL nanoparticles coating on CFs, has been effectively and rapidly activated through the application of an electrical voltage to restore the pristine strength of the epoxy/CF interface.

Table 5.9 IFSS values of uncoated, coated, healed and control samples, with the healing efficiencies (HE(%)) values.

Sample	IFSS (MPa)	H.E. (%)
U_CF	56.0 ± 9.5	-
C_CF	21.0 ± 5.4	-
Control (C_CF)	8.8 ± 1.7	-
H_CF	25.3 ± 2.3	107.3 ± 10.0

Further efforts will be required in the future to balance the excellent efficiency of self-healing and the decrease of the fiber/matrix interfacial shear strength due to the presence of the PCL coating. A possible approach could be represented by a finer tuning of the amount of nanoparticles deposited, considering therefore other combinations of PCL concentration and applied voltage.

5.2.3 Conclusions

In this study, PCL nanoparticles were utilized to create a self-healing interphase between an epoxy matrix and glass or carbon fibers. The PCL nanoparticles were prepared using a solvent displacement technique and were dispersed in water at varying concentrations. The application of PCL nanoparticles on the fiber surface was achieved through Electrophoretic Deposition (EPD). Morphological analysis revealed that the quality of deposition heavily depended on process parameters such as deposition time, applied voltage, and PCL solution concentration. Optimal conditions were determined, resulting in a uniform PCL coating on the fibers. Microdebonding tests were conducted to evaluate the interfacial adhesion (IFSS) and self-healing, after thermal mending at 80 °C for 1 hour. Regardless glass fibers, +26% IFSS and approximately 50% H.E. were achieved. Regarding carbon fibers, -60% IFSS and approximately 100% H.E. were achieved. These findings suggest that a PCL nanoparticle coating on fibers holds promise for effectively mending the interface in epoxy/glass composites, but its amount affects the initial interfacial adhesion properties. Moreover, it could be possible that the thermal mending provided by Joule heating effect allowed a more efficient interfacial healing since the heat was directly given along fiber/matrix interphase. The overall results demonstrated the strong potentiality of PCL as self-healable interphase in epoxy/(glass or carbon) composites.

6 General conclusions

6.1 Summary

Advanced materials like fiber-reinforced composites (FRCs) are largely used in construction due to their improved properties. However, their structural integrity may degrade over time due to various factors, demanding an early detection of defects. Therefore, challenges like interfacial debonding need to be addressed for optimal performance. Robust interfacial adhesion and self-healing capabilities are of paramount importance to reduce defects and to extend the material's service-life. Hence, the aim of this Doctoral Thesis was to provide a significant contribution to this field and it was structured around two primary research topics: the enhancement of the interfacial adhesion and the development of self-healing interfacial capabilities. In both research topics, the key aspect was the investigation of the interfacial properties at the microscale level, involving the fabrication of microcomposites subjected to microdebonding tests.

Regarding the first research topic, methods such as triboelectrification and laser treatments have shown to be promising in improving bonding strength, discussed in Chapter 4. Glass fibers were rubbed against poly(tetrafluoroethylene) surface to generate surface charges by contact electrification. It was found that the electrical charge on GFs surface attracted GO nanosheets forming a compact and homogeneous coating, which contribute in the enhancement of interfacial shear strength of 45%. On the other hand, basalt fibers were treated by CO_2 laser at different power levels. Thanks to the treatment, the tensile strength as well as Young's modulus of the fibres increased, and the IFSS was improved up to 8%. Such improvement was provided mainly due to the presence of fiber surface defects induced by the laser radiation, as confirmed by SEM.

Regarding the second research topic, the deposition of a continuous film or of a nanostructured coating made of PCL have demonstrated potential for interfacial self-healing, discussed in Chapter 5. Scanning electron microscopy and optical microscopy analyses revealed that well-applied and homogeneous coatings were formed, with an increase in surface roughness as indicated by atomic force microscopy. For the PCL film, an increase up to 16% in IFSS was obtained compared to neat interphase, while for the nanostructured coating the IFSS varied between +26% for glass fibers and -60% for carbon fibers, since the amount of PCL deposited seemed to affect the interfacial adhesion properties. The healing efficiency was calculated as the ratio of IFSS before and after the thermal mending. An impressive self-healing efficiency of 100% was obtained for both types of coatings, with a gradual decline over several debonding/healing cycles. A possible explanation could arise from the progressive modification of the matrix meniscus region after several healing/debonding cycles, which may have altered the stress state near the fibre/drop contact point, thus underestimating the IFSS values.

6.2 Future perspectives

The future steps of this research activity will be extensively dedicated to the development of a finite element model (FEM) of the interfacial region to understand the role played by the droplet shape and meniscus on repeated debonding/healing cycles. The Cohesive Zone Model (CZM) will be employed at this purpose. CZM is a numerical modelling approach used to simulate the behaviour of interfaces within materials where crack initiation, propagation, and interaction occur. It is particularly applied to study fracture and delamination in composite materials, adhesive joints, and other situations that involve the separation of material layers. The FEM model will be based on force data outputs from experimental tests conducted by coupling the microcomposite samples with Fiber

Bragg Grating (FBG) optical fiber attached to a strain sensor, as illustrated in Figure 6.1 [103].

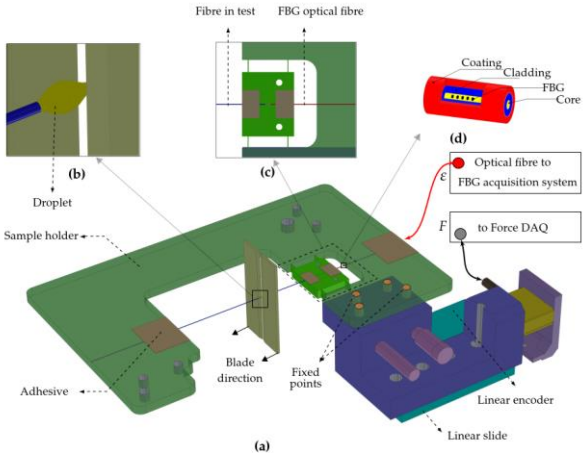

Figure 6.1 Strain measurement setup for microbond tests, (a) sample holder connected to the strain sensor, (b) blades in contact with the microcomposite, (c) strain sensor equipped with Fiber Bragg Grating (FBG) optical fiber, and (d) structure of FBG [103].

The simulation inputs will take into consideration the material characteristics of droplet, fiber, blades, adhesive and sample holder. The fiber will be assumed to behave as a linear-elastic material, while the droplet as an elastic-plastic one. The adhesive and the sample holder will be assumed to behave in linear-elastic manner. The blades will be considered rigid body with displacement as input during the simulation. The shape of the droplet will be determined based on optical microscope images taken before and after microdebonding and it will allow to understand the stress and strain distribution across the embedded length of the fiber droplet. The FEM model will utilize the mixed-mode quadratic nominal stress criterion for the damage onset (Equation 6.1) and the mixed-mode power law criterion for the damage evolution (Equation 6.2).

$$\max\left\{\frac{\tau_s}{\tau_{scr}}, \frac{\tau_t}{\tau_{tcr}} \frac{\tau_n}{\tau_{ncr}}\right\} = 1 \quad 6.1$$

Where τ_n, τ_s and τ_t are nominal stress when the deformation is either purely normal to the interface or purely in the first or the second shear direction, while τ_{ncr}, τ_{scr} and τ_{tcr} are the corresponding critical values.

$$\left(\frac{G_I}{G_{Icr}}\right)^{\alpha} + \left(\frac{G_{II}}{G_{IIcr}}\right)^{\alpha} + \left(\frac{G_{III}}{G_{IIIcr}}\right)^{\alpha} = 1 \quad 6.2$$

Where G_I, G_{II} and G_{III} are the work done by the tractions and their conjugate relative displacements in the normal, first, and second shear directions, while G_{Icr}, G_{IIcr} and G_{IIIcr} are the corresponding critical values.

FEM model will be developed by using Abaqus® 2022 software (Dassault Systemes, Co.). In Figure 6.2a, a representative image of a microdebonding specimen is shown, while in Figure 6.2b the evolution of the maximum principal stress at the interphase after microdebonding is displayed.

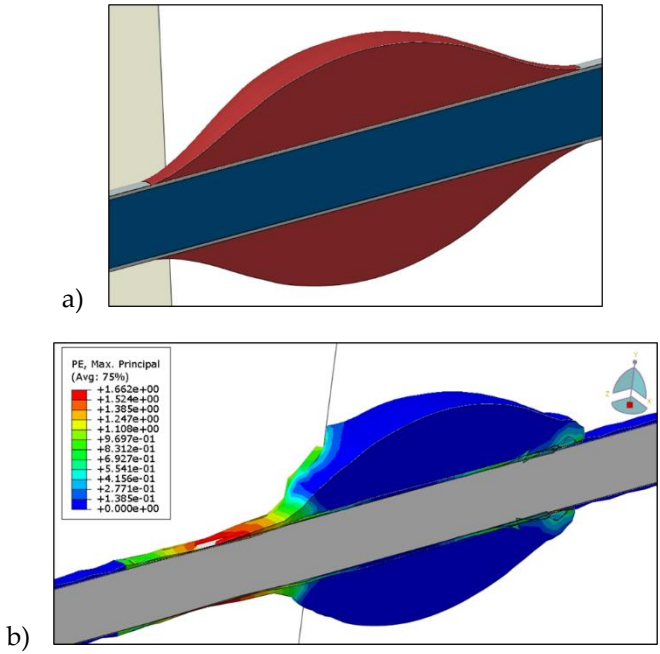

Figure 6.2 Examples of: (a) initial microdebonding specimen, (b) evolution of maximum principal stress after microdebonding. The model is generated using Abaqus® software, version 2022.

This part of future work will be accomplished in collaboration with Tampere University and Fibrobotics Oy (Tampere, Finland).

7 Other activities

7.1 Tailoring the physical properties of PLA through the addition of TPU and functionalized short CFs

Published Paper:
Simonini, L.; Mahmood, H.; Dorigato, A.; Pegoretti, A. Tailoring the physical properties of poly (lactic acid) through the addition of thermoplastic polyurethane and functionalized short carbon fibers. *Polymer Composites* **2023**, *44*, 4719-4733.

7.1.1 Introduction

The urge of replacing petroleum-based polymers is pushing materials engineers toward the development of new products based on natural resources, and biopolymers are therefore receiving growing interest in the scientific community [113-115]. Biopolymers are polymeric materials made starting from renewable resources and/or biodegradable [116-118], and among them, poly(lactic acid) (PLA) displays interesting physical and mechanical properties [119-122]. It is a bio-based and biodegradable aliphatic polyester derived from lactic acid. It is a relatively cheap polymer and offers excellent degradability and barrier properties [123]. It can be processed in many ways such as extrusion, spinning or injection moulding, with vast application perspectives in the future [120,124-127]. However, PLA is rather brittle, and this feature may limit its application in many industrial segments [128]. Therefore, there is a common interest to formulate new grades of PLA with improved ductility, while maintaining its tensile strength [129-132]. At this aim, different methods have been adopted, such as the use of plasticizers [133-135], incorporation of fillers [136-138] and blending with other polymers having elevated ductility [139-143]. In particular, the possibility of blending PLA with elastomers [144,145] and thermoplastic

polyurethanes (TPUs) [146-150] has been widely investigated in literature. TPU is a melt-processable thermoplastic elastomer characterized by high durability, flexibility, biocompatibility, and biostability [151,152]. However, elevated amounts of TPU (> 30 wt%.) must be added to PLA for a satisfactory toughening of PLA. The major drawback of adding large concentrations of TPU is the substantial decrease in strength and elastic modulus [153]. The addition of fillers may help to overcome this problem, thus obtaining a ternary material having better mechanical properties compared to the unfilled blends [154-157]. Recently, carbon fibers (CFs) have been considered as an ideal candidate to improve the mechanical properties of polymer blends, thanks to their outstanding strength and stiffness [115,158-160]. However, when CFs are used without any surface treatment, the resulting composites possessed low interfacial (IFSS) or interlaminar shear strength (ILSS). In order to overcome this limitation, surface treatments can increase the chemical compatibility of CFs with the matrix [161].
Therefore, the aim of the work was to investigate, for the first time, the effect of the oxidative acid treatment (H_2SO_4/HNO_3) of CFs surface on the mechanical performances of PLA/TPU/CF composites. The morphological and chemical properties of CFs before and after the surface modification were systematically investigated. Both untreated and acid-treated CFs were then added to PLA/TPU blends, and a comprehensive rheological, morphological, thermal and mechanical characterization of these ternary composites was performed. In this way, it could be possible to obtain PLA based composites with tailorable mechanical properties, that could overcome the actual technological limits of PLA and could extend the application fields of this material.

7.1.2 Materials and methods

7.1.2.1 Materials

Pellets of poly(lactic acid) (PLA) (density = 1.24 g/cm^3, MFI at 210 °C and 2.16 kg = 7 g/10 min, product code 4032D) were purchased by

NatureWorks LLC (Minnetonka, USA). Pellets of thermoplastic polyurethane (TPU) (density = 1.23 g/cm^3, melting temperature range 220 - 240 °C, product code 3059D) were supplied by Covestro Srl (Milano, Italy). Chopped carbon fibers Panex PX35 type 65 (density = 1.81 g/cm^3), having an average length of 6 mm and a mean diameter of 8 μm, were provided by Xenia Materials Srl (Vicenza, Italy). Sulfuric acid (H_2SO_4, purity 96 %, density 1.84 g/cm^3) and nitric acid (HNO_3, purity 69 %, density 1.06 g/cm^3) were provided by Sigma Aldrich Co. (Saint Louis, Missouri, USA).

7.1.2.2 Sample preparation

Functionalization of carbon fiber surface

Following the procedure described in [162], acid treatment of carbon fibers was performed by immersing them in a $H2SO_4/HNO_3$ acid mixture (relative weight ratio 3:1) under ultrasonic treatment. The treatment was performed for 15 minutes at 60 °C using a FALC (Shenzhen, China) ultrasonic bath. Then, the fibers were washed at room temperature under continuous stirring in deionized water to reach a neutral pH, and then dried at 80 °C for 24 hours under vacuum. In this work, untreated CFs were designed as uCF, while treated (functionalized) CFs were denoted as fCF.

Preparation of composite materials

Initially, both the polymers and the fibers were dried at 50 °C for at least 72 hours. PLA, TPU and CF were melt compounded in a Thermo Haake Rheomix® 600 (Thermo Fisher Scientific Inc, Waltham, USA) internal mixer at 220 °C for 5 min, setting a rotor speed of 50 rpm. Then, the resulting compounds were compression molded at 220 °C for 5 min at a pressure of 3.4 MPa, thus obtaining rectangular sheets with dimensions of 120 x 120 x 1 mm^3. The samples were prepared according to the formulations listed in Table 7.1.

Table 7.1 List of the prepared PLA/TPU/CF composites.

Sample	PLA (wt%)	TPU (wt%)	uCF (wt%)	fCF (wt%)
PLA	100.0	-	-	
PLA/10	90.0	10.0	-	
PLA/20	80.0	20.0	-	
PLA/30	70.0	30.0	-	
PLA/10/uCF	85.5	9.5	5.0	
PLA/20/uCF	76.0	19.0	5.0	
PLA/30/uCF	66.5	28.5	5.0	
PLA/10/fCF	85.5	9.5	-	5.0
PLA/20/fCF	76.0	19.0	-	5.0
PLA/30/fCF	66.5	28.5	-	5.0

7.1.2.3 Experimental techniques

Chemical characterization

Carbon fibers were characterized by Fourier transform infrared (FTIR) spectroscopy in attenuated total reflectance (ATR) mode with a Perkin Elmer Spectrum One FT-IR spectrometer (Perkin Elmer Inc, USA). A minimum of 16 scans with a resolution of 4 cm^{-1} were performed, between a scanning interval of 4000 and 650 cm^{-1}.

Rheological characterization

The dynamic rheological properties of the composite samples were analyzed through a Discovery Hybrid Rheometer (DHR-2) (TA Instruments Inc., Newcastle, USA), by adopting a plate-plate configuration. These tests were carried out at 220 °C, applying a strain amplitude of 1% on discoidal specimens with a diameter of 25 mm. The thickness of the gap was set at 1 mm. In this way, the trends of the storage modulus (G'), of the loss modulus (G'') and of the complex viscosity (η) were investigated in an angular frequency (ω) range between 0.1 and 100 rad/s.

Morphological characterization

The morphological observations were performed through a Zeiss Supra 40 field-emission scanning electron microscope (FESEM), operating at an acceleration voltage of 3.5 kV. Before the observation, the samples were coated with a Pt/Pd alloy (80:20) conductive layer having a thickness of about 5 nm.

Thermal characterization

Differential scanning calorimetry (DSC) was performed by using a Mettler DSC30 calorimeter (Mettler Toledo, Columbus, OH). The samples were heated from 0 to 200 °C and subsequently cooled from 200 to 0 °C. Finally, a second heating stage was applied from 0 to 200 °C. These thermal ramps were performed at a rate of 10 °C/min, under a nitrogen flux equal to 100mL/min. Only one specimen was tested for each composition. The relative degree of crystallinity (χ) of the PLA phase in the samples was calculated through Equation 7.1.

$$x = \frac{\Delta H_m - \Delta H_{cc}}{\varphi_{PLA} \Delta H_m^0} \times 100 \qquad 7.1$$

Where ΔH_m is the enthalpy of fusion of PLA, ΔH_{cc} is the enthalpy of cold crystallization of PLA, φ_{PLA} is the weight fraction of PLA in the composite and ΔH^0_m is the standard melting enthalpy of the fully crystalline PLA, taken as 93.7 J/g [163].

Thermogravimetric analysis (TGA) was carried out by using a TA-IQ5000 IR (New Castle, USA) thermobalance under an air flow of 100 mL/min in a temperature interval from 35 °C to 700 °C at a heating rate of 10 °C/min. The onset of degradation temperature (T_{onset}), the degradation temperature (T_d) corresponding to the temperature associated to the maximum mass loss rate, and the residual mass (m_{700}) at the end of the tests were determined.

Mechanical characterization

Dynamic mechanical analysis (DMA) was carried out in tensile mode by using a TA Q800DMA (TA Instruments Inc, Newcastle, USA) machine. Rectangular specimens (30 x 5 x 1 mm^3) with a gage length

of 10 mm were tested in a temperature range from 0 °C to 200 °C at a heating rate of 3 °C/min, a test frequency of 1 Hz, a strain amplitude of 0.05 %. In this way, the trends of the storage modulus (E'), of the loss modulus (E'') and of the loss tangent (tanδ) were investigated as a function of temperature. The glass transition temperature (T_g) of the PLA phase was estimated from the tanδ peak.
Quasi-static tensile tests were performed by using an Instron® 5969 (Instron, Norwood, USA) universal testing machine, equipped with a load cell of 1 kN, testing 1BA type dumbbell specimens according to the ISO 527 standard. Tensile tests for the evaluation of the elastic modulus (E) were performed at a crosshead speed of 0.25 mm/min, imposing a maximum axial deformation level of 1 %. The strain was recorded by using a dynamic extensometer Instron model 2620-601 (gauge length of 12.5 mm). According to ISO 527 standard, the elastic modulus was evaluated as a secant value between deformation levels of 0.05 % and 0.25 %. Tensile properties at break were evaluated at a crosshead speed of 1 mm/min, without using the extensometer. The maximum stress (σ_{max}) and the elongation at break ($\epsilon_{\%}$) were determined for each composition. At least five specimens were tested for each sample.

7.1.3 Results and discussion

7.1.3.1 Chemical and morphological characterization of carbon fibers

FTIR spectroscopy allowed to detect the functional groups introduced on the surface of the fibers by the acidic treatment. Figure 7.1 shows the FTIR spectra of carbon fibers before and after the acid treatment. Strong absorption bands of -OH groups appear at 3332 cm^{-1} after the chemical modification of CFs. The bands around 1300 cm^{-1} and 1700 cm^{-1} correspond to the stretching vibrations of -C=O group. Similar FTIR transmittance spectra of carbon fibers before and after an acidic treatment can be found in literature [164,165]. These observations confirm that the fiber surface activity was significantly enhanced by the acidic treatment, which introduced reactive functional groups on the CF surface.

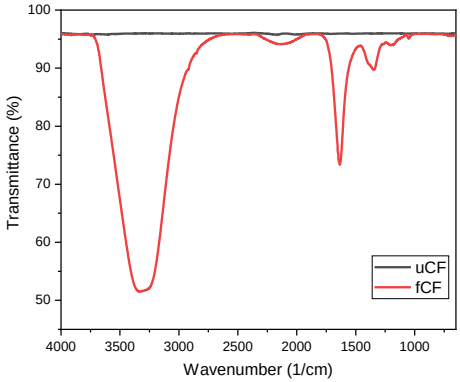

Figure 7.1 FTIR spectra of CFs before (uCF) and after (fCF) the acid treatment.

SEM micrographs of uCF and fCF are represented in Figure 7.2 (a, b), together with their optical appearance. The surface of the fibers results to be altered after the chemical modification, as the fCFs seem considerably rougher than uCFs. The presence of deeper groves increases the surface area of fCF, thus improving the number of active sites on the fiber surface. These sites could provide a better mechanical interlocking between CFs and the polymeric phases, ultimately increasing the interfacial adhesion [165,166]. Moreover, the chemical modification of CFs tends to separate the short fibers from the bundles, making their dispersion inside the matrix easier during melt compounding.

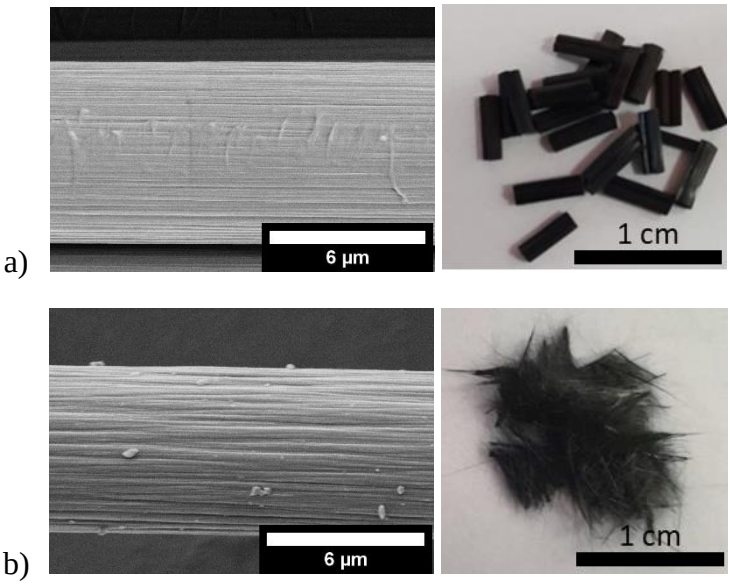

Figure 7.2 SEM micrographs of (a) uCF and (b) fCF, together with their optical appearance.

7.1.3.2 Rheological characterization of the composites

Figure 7.3, Figure 7.4 and Figure 7.5 show the dynamic rheological properties of neat PLA and TPU, of their blends and of the relative composites in terms of storage modulus (G′), loss modulus (G′′) and complex viscosity (η).

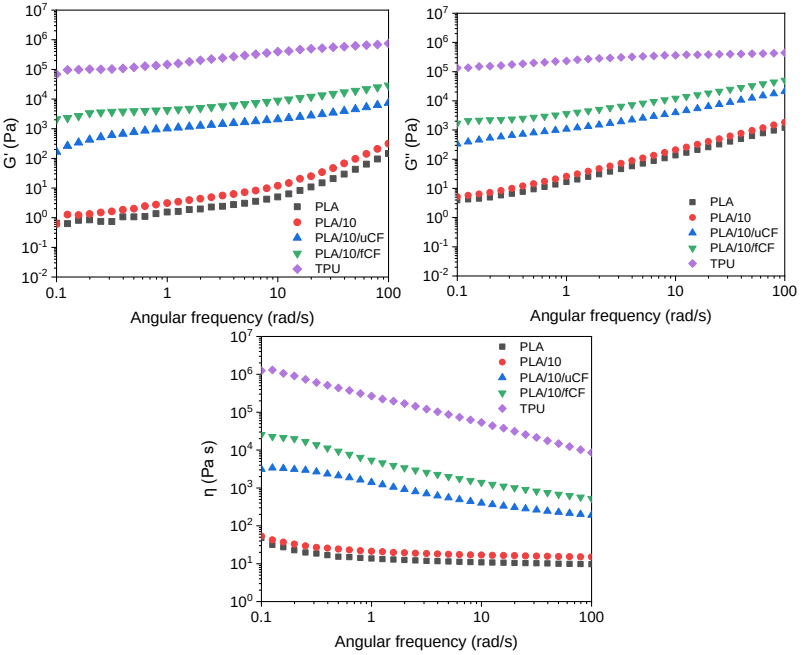

Figure 7.3 Storage modulus (G′), loss modulus (G″) and complex viscosity (η) of neat PLA and TPU, of the blends and of the relative composites. TPU content of 10 wt%.

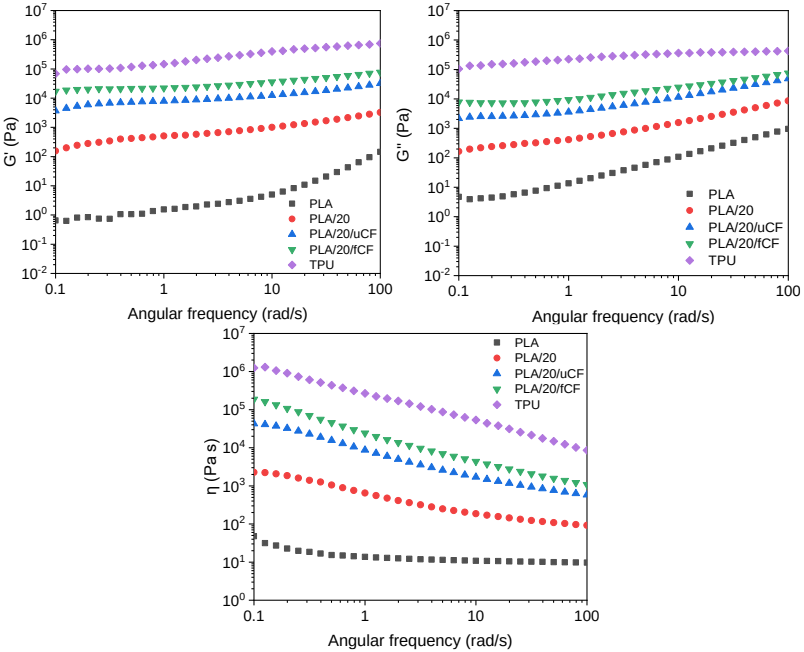

Figure 7.4 Storage modulus (G′), loss modulus (G′′) and complex viscosity (η) of neat PLA and TPU, of the blends and of the relative composites. TPU content of 20 wt%.

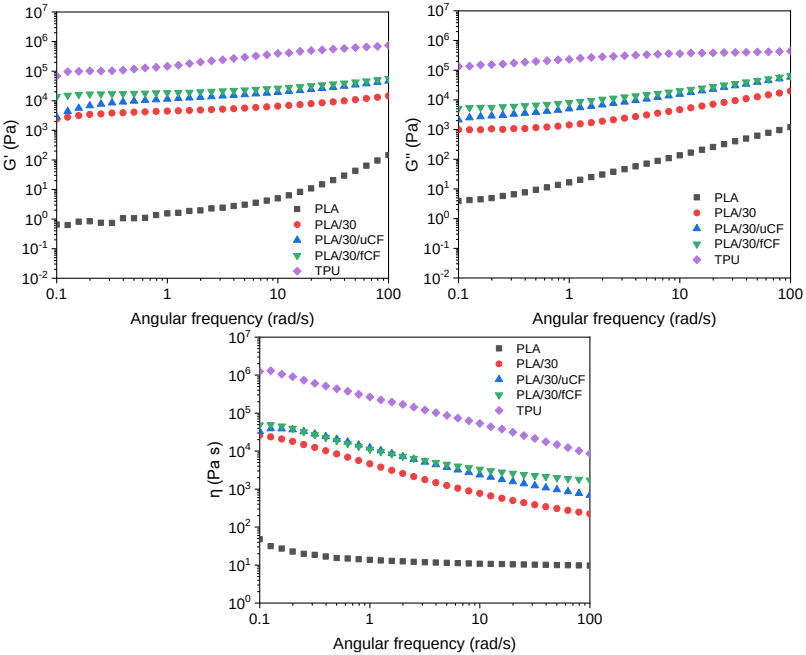

Figure 7.5 Storage modulus (G'), loss modulus (G'') and complex viscosity (η) of neat PLA and TPU, of the blends and of the relative composites. TPU content of 30 wt%.

At a general level, it can be noticed that all the samples present a pseudoplastic behavior, with a decrease of the complex viscosity as a function of the frequency. It can be also concluded that the TPU matrix has higher G', G'' and η values with respect to PLA. Therefore, the dynamic moduli and the viscosity of PLA/TPU blends increase with the TPU amount. This trend can be also partially due to the formation of hydrogen bonds between the carbonyl groups of TPU and the hydroxyl groups of PLA, and the sub-amide groups of TPU and the carboxyl group of PLA [167]. As it could be expected, regardless of the TPU content, the presence of CFs in the blends shifts the rheological parameters to higher values, because the chain mobility is restricted by the fibers. Considering the composites with

the same CF concentration, it can be noticed that the G', G'' and η values of fCFs filled samples are systematically higher than that of the samples containing uCFs. Higher viscosity implies a stronger fiber–matrix interaction, and this means that the acidic treatment on CFs probably leads to a stronger interfacial bonding with the PLA/TPU matrix.

7.1.3.3 Morphological characterization of the composites

SEM micrographs of neat PLA, PLA/TPU blends and the relative composites are represented in Figure 7.6. PLA exhibits a relatively smooth and clear surface, typical of a brittle polymer. In the micrographs of the blends, it is possible to notice that the TPU phase is well dispersed within the PLA matrix, and it assumes a spherical form. However, particle debonding denotes a poor interfacial adhesion between the two phases. By increasing the amount of TPU, their domains become larger in diameter, passing from 1.5 ± 0.5 μm for PLA/10 blend up to 3.9 ± 1.3 μm for the PLA/30 sample. Moreover, the interfacial adhesion with PLA seems to be better when the TPU content increases. Once again, this can be explained by the formation of H-bonds and dipolar interactions between ester and urethane fragments. A similar microstructural behaviour is reported in literature for PLA/TPU blends [168]. Analysing the microstructure of PLA/TPU blends reinforced with uCF, it can be noticed that crack propagation occurs at different planes of the matrix, with failure progressing along the fiber/matrix interface, hence a fiber pull-out phenomenon occurs in such composites. On the contrary, in the blends reinforced with fCF, the fracture plane is almost flat and shorter fiber length can be detected. This indicates a strong interfacial adhesion between the blends and the fibers, which results in the fracture of fibers rather than a fiber pull-out failure mechanism. The reactive groups introduced on the surface of fCFs by the acidic treatment react with the PLA/TPU matrix, thus improving the interfacial adhesion. Also, some residues of PLA/TPU matrix can be observed along the pulled fCFs, proving once again a

better interfacial compatibility with respect to uCFs filled composites.

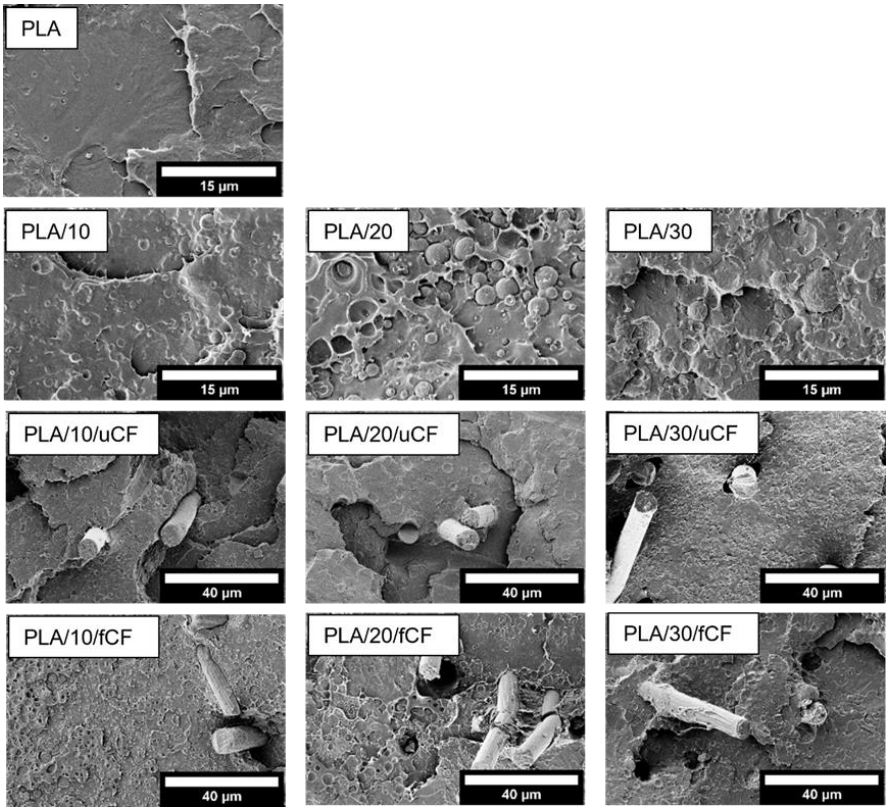

Figure 7.6 SEM micrographs of PLA, PLA/TPU blends and their relative composites.

7.1.3.4 Mechanical characterization of the composites

DMA thermograms of neat PLA and TPU, PLA/TPU blends and the relative composites are represented in Figure 7.7(a-c), while the most important parameters are summarized in Table 7.2.

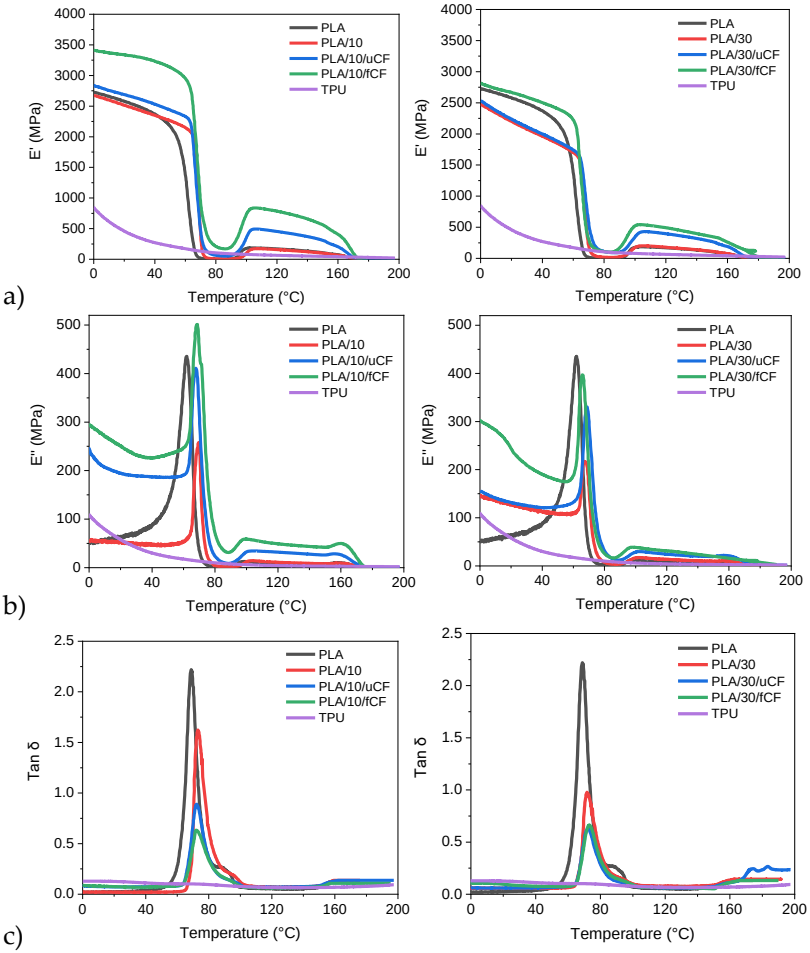

Figure 7.7 DMA tests on neat PLA and TPU, blends and on the relative composites. Trends of (a) storage modulus (E′), (b) loss modulus (E′′) and (c) tanδ at different TPU contents.

Table 7.2 Results of dynamic-mechanical analysis (DMA) on neat polymers, blends and on the relative composites.

Sample	E′ (0 °C) (MPa)	E′ (105 °C) (MPa)	tanδ peak intensity	T_g* (°C)
PLA	2726	185	2.2	68.4
TPU	844	75	-	-
PLA/10	2672	171	1.6	72.8
PLA/30	2475	202	1.0	73.9
PLA/10/uCF	2835	494	0.9	74.2
PLA/30/uCF	2534	428	0.7	75.7
PLA/10/fCF	3412	838	0.6	73.4
PLA/30/fCF	2814	540	0.6	72.7

*Evaluated as the temperature corresponding to the tanδ peak

The storage modulus (E′) of PLA at 0 °C is equal to 2726 MPa and it decreases significantly above its T_g (68.4 °C). Then, a slight increase of E′ up to 185 MPa can be detected between 100 °C and 160 °C, due to the cold crystallization of PLA during the test. TPU shows limited E′ values (844 MPa at 0 °C) in the temperature range analyzed, since it is above its T_g (-42 °C according to the datasheet). Regarding the blends, a slight positive shift in the T_g values is observed upon TPU addition, probably because DMA has a higher sensitivity than DSC in detecting the thermal transitions within the polymeric materials. Moreover, the E′ value of PLA decreases with TPU content and this phenomenon is more evident for sample PLA/30 that shows a decrease of E′ of 10% than neat PLA, at 0 °C. The introduction of uCFs causes a slight increment of E′ below T_g, while a more considerable enhancement can be detected in the case of fCFs (up to 25.2 % for PLA/10/fCF at 0 °C). Bind et al. [169] showed that this behavior is a clear indication of both a homogeneous dispersion of the reinforcement in the matrix and of the existence of a strong interfacial interaction. The tanδ peaks intensity is reduced in presence of fCF which is also an indication of the improved

interaction between the matrix and fCFs: this proofs once again the efficacy of the acid functionalization of CFs [170]. As explained by Chua et al. [171], the formation of strong bonds between fibers and matrix reduces the motion of the polymeric chains, thus resulting in lower tanδ peak values.

Representative stress-strain curves of neat PLA, PLA/TPU blends and the relative composites are reported in Figure 7.8, while the values of elastic modulus, stress at break and elongation at break are compared in Figure 7.9(a-c).

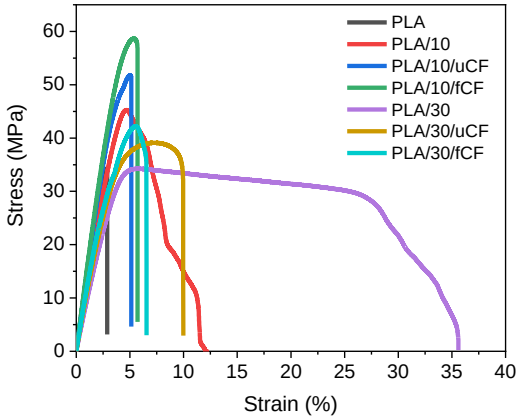

Figure 7.8 Representative stress-strain curves of neat PLA, PLA/TPU blends and the relative composites.

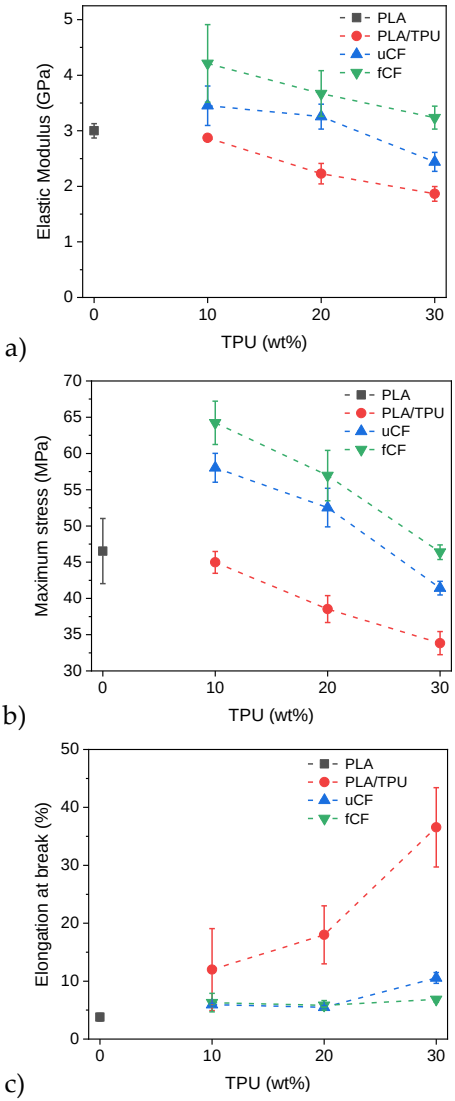

Figure 7.9 Values of (a) elastic modulus, (b) maximum stress and (c) elongation at break from tensile tests on neat PLA, PLA/TPU blends and the relative composites.

Neat PLA has an elastic modulus of 3 GPa, a maximum stress of 47 MPa and an elongation at break of 4 %. The addition of increasing amounts of TPU (from 10 % wt. to 30 % wt.) decreases the stiffness and the strength of PLA. In particular, when 30 % wt. TPU is added to PLA, the elastic modulus decreases by 38 % and the stress at break by 27 %. On the other hand, TPU addition leads to a noticeable increase in the elongation at break (up to 867 % with a TPU concentration of 30 % wt.), highlighting the role played by TPU as toughening agent inside the brittle PLA matrix. The loss of stiffness and maximum stress of PLA is efficiently recovered, and in some cases overcompensated, by the introduction of CFs inside the polymeric matrix, and this beneficial effect is more evident in the case of the fCFs. In particular, due to the addition of 5 % wt. fCFs to PLA/10 sample, the elastic modulus is increased by 47 % with respect to the corresponding blend, and only by 20 % in the case of uCFs. For PLA/20 blend, the addition of fCFs improves the elastic modulus by 65 % (46 % for uCF), while for PLA/30 blend by 74 % (31 % for uCF). Regarding the maximum stress, the introduction of 5 wt%. fCF in PLA/10, PLA/20 and PLA/30 samples improves the maximum stress of the corresponding blends by 43 %, 48 % and 37 % respectively (29 %, 36 % and 22 % for uCF). These results suggest that fCFs have a good interfacial compatibility with PLA/TPU matrix, due to the formation of a strengthened interphase upon the acid functionalization of CFs. Regarding the elongation at break, the strong increase given by the introduction of TPU in the PLA matrix is lost by adding both uCFs and fCFs. However, PLA/10/fCF, PLA/20/fCF and PLA/30/fCF still show higher elongation at break values than neat PLA, with a relative improvement of 66 %, 55 % and 81 %, respectively. For a given fiber content, the elongation at break values obtained with the introduction of fCF and uCF are quite similar, thus suggesting that the adopted chemical treatment does not substantially influence the elongation at break of the material. It can be therefore concluded that the adopted approach, based on a combination of TPU blending and the addition of functionalized

CFs, can lead to an improvement of the stiffness and of the maximum stress of the PLA, and also the ductility of the material is improved. This strategy could represent a valuable solution to extend the application fields of PLA.

7.1.4 Conclusions

In this work, a PLA matrix was melt compounded with different amounts of TPU and a fixed concentration of CFs, in order to increase the ductility of PLA and to retain its stiffness and strength, with the aim to extend the applicability of this material. Both untreated and functionalized CFs were utilized. Acid surface modification of chopped CFs was performed by dipping the CFs in solution of H_2SO_4 and HNO_3 and performing ultrasonication. Infrared spectroscopy revealed the formation of strong chemical functionalities on the surface of the fibers upon acid treatment. Morphological analysis showed that the fCFs had a rougher surface than uCFs, which allowed a better adhesion with the matrix. Rheological measurements on the composites demonstrated that the introduction of fCFs implied higher complex viscosity values with respect to the composites filled with uCFs, due to a stronger fiber–matrix interaction. DSC and TGA tests showed that the presence of modified fibers did not alter significantly the thermal properties of the PLA matrix. Dynamic-mechanical analysis showed the improved dynamic-tensile properties of composites made of fCFs below T_g and confirmed the enhanced interfacial adhesion between fibers and matrix (see the reduced intensity of tanδ peaks). Quasi-static tensile tests proved that composites made by fCFs showed higher tensile modulus and maximum stress than the corresponding blends, but the introduction of CFs resulted in a drastic reduction of elongation at break with respect to the corresponding blends. However, fCF filled composites still showed improved values of the elongation at break than neat PLA (+81 % in the case of PLA/30/fCF). The adopted approach could therefore represent a valuable solution to obtain PLA based composites with tailorable properties, in order to overcome

the actual technological limits of PLA and to extend the application fields of this emerging material.

7.2 Mechanical reprocessing of polyurethane and phenolic foams to increase the sustainability of thermal insulation materials

Paper under review to *Polymer Testing*:
Simonini, L.; Sorze, A.; Maddalena, L.; Carosio, F.; Dorigato, A.
Mechanical reprocessing of polyurethane and phenolic foams to increase the sustainability of thermal insulation materials

7.2.1 Introduction

Nowadays the increasing interest in sustainable practices and environmentally friendly construction methods is affecting also the field of thermal insulation materials. These aspects involve the minimization of the heat transfer, the reduction of energy consumption, and the simultaneous management of the waste [172-174]. In this scenario, polyurethane (PU) foams are widely recognized for their outstanding thermal insulating properties, and have emerged as a preferred choice for insulating applications in several sectors, such as residential and commercial buildings, transportations and military industry [175,176]. PUs are low density thermosetting polymers that are synthesized from the exothermic reaction between polyol and poly(isocyanate) [177,178]. The intensification of their use has led to their responsible end-of-life management, and recycling has been recognized as the most effective alternative to reduce landfilling and achieve sustainability [179,180]. The recycling methods for polyurethanes are divided in mechanical recycling, chemical recycling, and energy recovery. Mechanical recycling is the most widespread practice due to its low cost, high efficiency and applicability to all kinds of PU [181]. Mechanical recycling involves the physical reprocessing of polyurethane waste to create new products or materials. PU waste is shredded into granules and used as a filler or reinforcement in the production of new polyurethane products [182]. However, the main

challenge of mechanical recycling is to maintain a regular cell structure of the foam even at elevated PU recyclate amounts, in order to avoid a loss of the thermal insulation properties in the resulting foams. Therefore, one solution could be the incorporation of recycled insulation materials, having a higher insulating power, into the virgin polyurethane products, in order to compensate the negative effects on the cellular structure generated by the recyclate introduction. In this sense, phenolic foams (PFs) can be considered as a valuable option. PFs are thermosetting polymers synthesized from the exothermic condensation between phenol and formaldehyde [183,184]. PFs are known for their excellent thermal insulation, fire resistance, low smoke emission and high-temperature stability, which makes them suitable for applications in fire-resistant construction systems [185,186]. However, PFs usually exhibit low compressive and flexural strength, high brittleness and high friability, which restrict their application [187]. As per PU, the continuous growth in their use must be counteracted by an improved recycling technology [188,189].
Therefore, the aim of this work was to perform a comprehensive analysis of the potential of mechanical recycling of both PU and PF for the development eco-sustainable expanded polyurethane panels for thermal insulation applications. PU and PF were ground into two different particle sizes and incorporated into new PU foams at different weight concentrations. The resulting foamed materials were characterized from a morphological and thermo-mechanical point of view, with particular attention to their fire behaviour.

7.2.2 Materials and methods

7.2.2.1 Materials

Polyol (HDR R 150) and isocyanate (ISN 1), having viscosity of 1050 cPs and 200 cPs and density 1.10 g/cm^3 and 1.23 g/cm^3, respectively, were provided as liquids reagents by Kairos Srl (Verona, Italy) and used to prepare the virgin PU foam. Recycled polyurethane foam was obtained by discarded panels (RBF312-C) having dimensions of

80×100×10 cm^3, supplied by Giona Holding Srl (Santa Maria di Zevio, Italy). These panels had a geometrical density equal to 0.040 g/cm^3 and a thermal conductivity of 0.022 W/m·K at 10 °C, as reported in the datasheet. Recycled phenolic foam was obtained from ISO FEN - VIT VV thermal insulating panels, with dimension of 60×120×10 cm^3, provided by Isolmec Group Spa (Como, Italy). This material had a geometrical density equal to 0.035 g/cm^3 and thermal conductivity of 0.019 W/m·K at 10 °C, as reported in the datasheet.

7.2.2.2 Sample preparation

Neat polyurethane foam was prepared by mixing at ambient temperature the liquid reagents, i.e., polyol and isocyanate, at a constant weight ratio of 100:130, as suggested by the supplier. The mixing process was performed at 300 rpm for 20 seconds to achieve a homogeneous mixture, that was then poured into a preheated (40 °C) mold having dimensions 250×250×25 mm^3, and placed in an oven for 20 minutes at 40 °C to obtain a foamed material. For the first 15 minutes a weight was positioned above the mold to prevent the formation of uneven panels, then it was removed to allow the material to relax for 5 minutes.

Recycled foams were prepared by grinding the discarded panels of PU and PF for 10 minutes by using an Ika Werke M20 mill (Ika AG, Staufer, Germany). The ground material was then sieved to recover granules having dimension ≤ 100 μm and 100-200 μm (respectively denoted with letter "f" and "c", to indicate a fine and a coarse granulometry). The sieved material was dried at 40 °C overnight, then it was gradually added to the polyol and manually mixed for 20 seconds to achieve a homogeneous mixture. Isocyanate was then added to the mixture at the same relative weight ratio used for the production of neat PU foams, and stirred for additional 20 seconds. The mixture was then poured into the preheated mold (40 °C) and subjected to the foaming process previously described for neat PU panels. In this way, foams with a PF (or PU) recycled amount of 2.5 %wt, 5.0 %wt, and 7.5 %wt (with respect to the total weight of the

liquid PU precursors) were prepared. These weight concentrations corresponded to a recycled PU content respectively equal to 40.1 %vol, 58.3 %vol and 68.3 %vol, and a recycled PF concentration respectively equal to 50.9 %vol 73.3 %vol and 85.9 %vol (with respect to the total volume of the liquid PU precursors). The denomination of the prepared samples is summarized in Table 7.3. In this manuscript, the sample nomenclature has been chosen to indicate the weight content of the recycled material.

Table 7.3 List of prepared samples.

Sample	PU virgin (% wt)	Granulometry of recyclate (μm)	PU recyclate (% wt)	PF recyclate (% wt)
PU	100.0	-	-	-
PF	0.0	-	-	-
PU2.5fPU	97.5	≤ 100	2.5	-
PU5.0fPU	95.0	≤ 100	5.0	-
PU7.5fPU	92.5	≤ 100	7.5	-
PU2.5cPU	97.5	100-200	2.5	-
PU5.0cPU	95.0	100-200	5.0	-
PU7.5cPU	92.5	100-200	7.5	-
PU2.5fPF	97.5	≤ 100	-	2.5
PU5.0fPF	95.0	≤ 100	-	5.0
PU7.5fPF	92.5	≤ 100	-	7.5
PU2.5cPF	97.5	100-200	-	2.5
PU5.0cPF	95.0	100-200	-	5.0
PU7.5cPF	92.5	100-200	-	7.5

7.2.2.3 Experimental techniques

Morphological characterization

The morphological appearance of the prepared foams was observed by field emission scanning electron microscopy (FESEM) using a Carl Zeiss AG - SUPRA 40 (Carl Zeiss, Oberkochen, Germany) microscope operating at acceleration voltage of 3.5 kV. Before the observation, the samples were coated with platinum (Pt) and

palladium (Pd) in a ratio 80:20 for 20 seconds to make them conductive, by using a Quorum Q150T ES sputter coater (Quorum Technologies, Lewes, UK).

The porosity of the foams was evaluated through the calculation of the geometrical and the theoretical density of the samples. The geometrical density (ϱ_{geom}) is defined as the experimental density of a structure that includes defects and porosity. It was calculated according to Equation 7.2:

$$\rho_{geom} = \frac{m_{sample}}{V_{geom}} \quad 7.2$$

where m_{sample} is the weight (in grams) and V_{geom} is the geometrical volume (in g/cm^3) of cylindrical samples cut from the prepared foams. The theoretical density (ϱ_{th}) is defined as the density of a structure without defects and porosity. It is obtained from the Mixture Rule (Equation 7.3):

$$\rho_{th} = \sum_{i=1}^{n} \varphi_i \cdot \rho_i \quad 7.3$$

where φ_i is the volumetric fractions of each constituent (i.e. polyol, isocyanate and waste) and ϱ_i are the densities of the components.

The apparent density (ϱ_{app}) was measured with an Accupyc 1330 helium pycnometer (Micromeritics Instrument Corporation, Norcross, GA, USA) following ASTM D6226 standard. Measurements were conducted at constant temperature of 23 °C, using a 1 cm^3 cell and performing 30 cycles. The total porosity (P_{tot}) was calculated as reported in Equation 7.4:

$$\boldsymbol{P_{tot}} = \left(\mathbf{1} - \frac{\boldsymbol{\rho_{geom}}}{\boldsymbol{\rho_{th}}}\right) \quad 7.4$$

The open porosity (P_{open}) was calculated as reported in Equation 7.5:

$$P_{open} = \left(1 - \frac{\rho_{geom}}{\rho_{app}}\right) \quad 7.5$$

Therefore, the closed porosity (P_{closed}) was calculated as reported in Equation 7.6:

$$P_{closed} = P_{tot} - P_{open} \quad 7.6$$

Evaluation of the thermal conductivity

The thermal conductivity (λ) of the prepared foams was determined on specimens of 150x150x25 mm^3 using a Netzsch HFM 446 small lambda instrument (Netzsch-Gerätebau, Selb, Germany), at constant temperature of 10 °C and according to ASTM C518-21.

Mechanical characterization

Three-point bending tests were performed using an Instron 5969 machine (Instron® Mechanical Testing Systems, Norwood, MA, USA), equipped with a load cell of 1 kN, in order to determine the flexural modulus (E_f), the flexural strength (σ_f) and the flexural strain at break (ε_f) according to ISO 1209-2. Samples had dimensions of 230×30×15 mm^3, and a span-to-depth ratio of 12 was used. The tests were carried out at constant temperature of 24 °C at a speed of 20 mm/min, and at least 10 specimens for each composition were tested. Quasi-static compression tests were performed with the Instron 5969 machine (Instron® Mechanical Testing Systems, Norwood, MA, USA), equipped with a load cell of 1 kN, in order to determine the compressive modulus (E_c) and the compressive strength (σ_c), according to ASTM D1621-16 standard. Samples had dimensions 50×50×25 mm^3, tests were carried out at constant temperature of 24 °C, with a testing speed of 2 mm/min. At least 10 specimens for each composition were tested.

Forced combustion tests

Cone calorimetry measurements (Noselab, Milan, Italy) were conducted following ISO 5660-1 standard considering a 35 kW/m^2 radiative heat flux and setting a distance of 25 mm between the specimens and the radiation source. Specimens with dimensions 100×100×20 mm^3 were preliminarily conditioned at a temperature of 23 ± 0.1 °C and at a relative humidity of 50 ± 0.1 % for at least 48 hours in climatic chamber, and all formulations were tested in triplicate. Post combustion cone calorimetry residues were analysed by a Zeiss Evo 15 scanning electron microscope (Carl Zeiss,

Oberkochen, Germany) operating at 20 kV. Samples were positioned on conductive tapes and gold sputtered before the measurements.

7.2.3 Results and discussions

7.2.3.1 Morphological characterization

Representative SEM micrographs of the recycled PU and PF foams after the sieving process are reported in Figure 7.10.

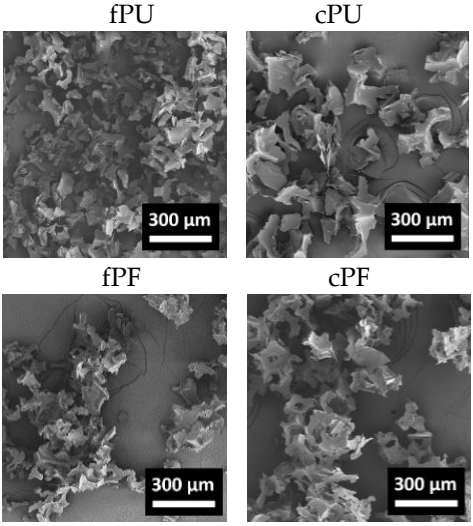

Figure 7.10 SEM micrographs of sieved recycled PU and PF particles.

The sieved materials appear as sharp particles with irregular morphology. Their normal size distribution is shown in Figure 7.11, while their mean value and standard deviation are specified in Table 7.4.

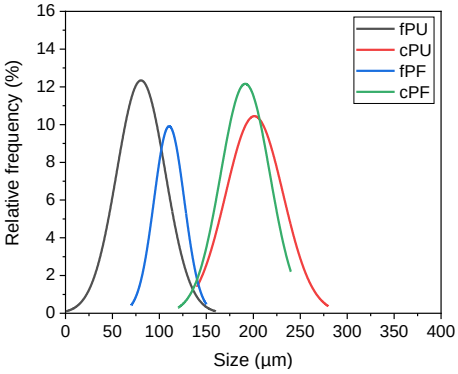

Figure 7.11 Normal distribution of recycled particle size after sieving.

Table 7.4 Mean values of the recycled particles size after sieving.

Samples	Size (µm)
fPU	80.4 ± 25.8
cPU	201.2 ± 30.5
fPF	110.4 ± 16.1
cPF	191.5 ± 26.2

The rather tight size distribution suggests that the materials have been efficiently ground and sieved, resulting in PU and PF foam recyclates with good morphological uniformity.

The morphology of prepared foams is displayed in SEM micrographs in Figure 7.12.

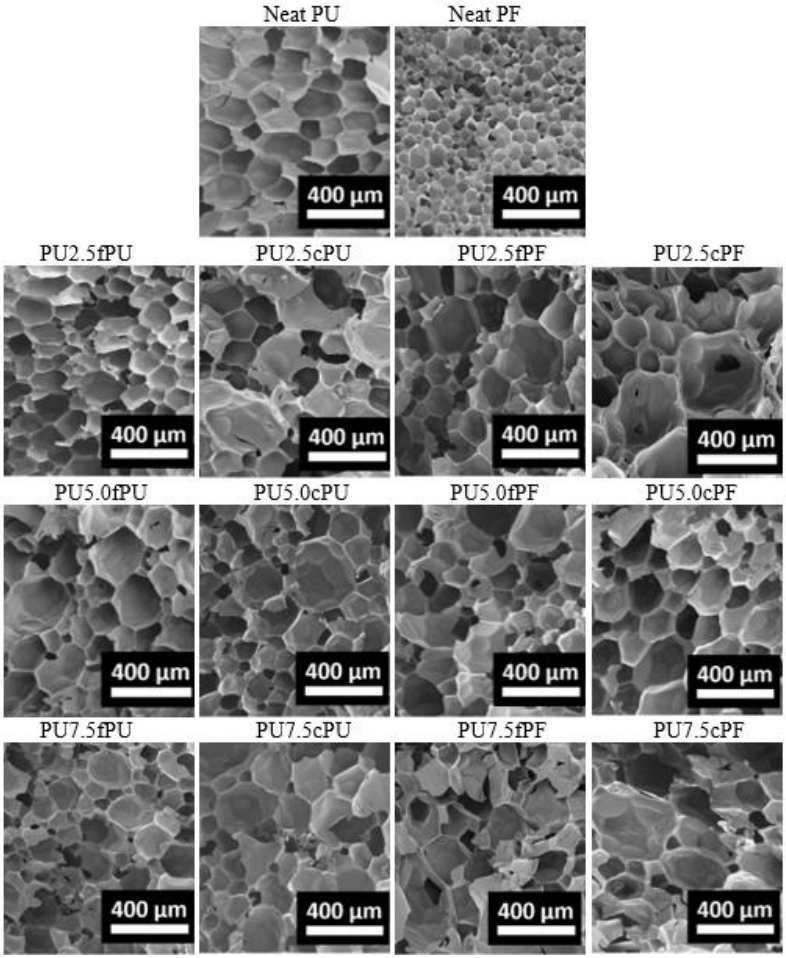

Figure 7.12 SEM micrographs of prepared foams.

Neat PU and PF foams show a regular cell structure with a uniform porosity and a clear definition of the cell walls. The progressive addition of the recycled foams allows to substantially maintain the regularity of the cell structure, but their presence is not clearly visible since they are embedded in the virgin PU foamed matrix.

This suggests that, despite the elevated volume fraction of recyclate present in the liquid mixture, the PU precursors adequately wet the recycled particles, ensuring a rapid and efficient foaming process. On the other hand, the addition of PU and PF recyclates at a concentration of 7.5 %wt determines the most significant morphological changes in the cellular structure. Even if in these foams the homogeneity of the cellular structure is not dramatically impaired, the increased viscosity of the liquid matrix due to recycled addition could have probably slowed down the crosslinking reaction within the PU matrix [190]. Moreover, from these micrographs it is evident that some interconnected porosity is created in the foams upon the introduction of the recycled particles, and this could potentially affect their thermal conductivity. In particular, the white parts in the micrographs correspond to the closed pores, whereas the dark sections are related to the open holes. A clear visualization of this phenomenon can be seen in Figure 7.13 where the presence of a recycled PF particle induces the formation of open porosity in the foam structure.

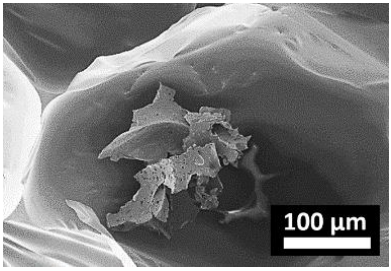

Figure 7.13 SEM image showing the formation of an open pore due to the presence of a recycled PF particle within the virgin PU foam (sample PU7.5cPF).

The normal distribution of the cell size in the prepared foams is represented in Figure 7.14(a,b), while mean values and standard deviation are specified in Table 7.5.

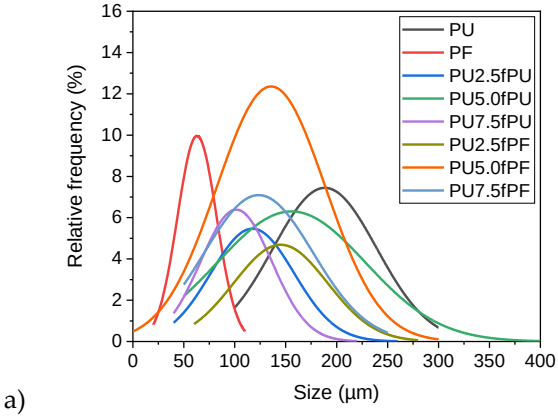

a)

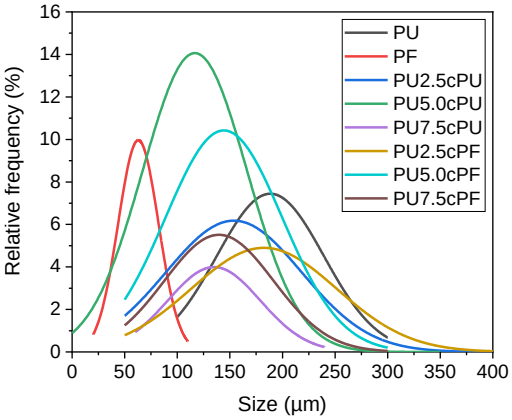

b)

Figure 7.14 Normal distribution of the cellular structure size of recycled PU and PF foams, deriving from (a) fine and (b) coarse recycled foams.

Table 7.5 Mean values of pore size from Normal distribution function.

Samples	Size (μm)
PU	188.5 ± 50.9
PF	62.9 ± 19.2
PU2.5fPU	117.4 ± 40.9
PU5.0fPU	155.6 ± 72.8
PU7.5fPU	101.4 ± 34.9
PU2.5cPU	153.7 ± 64.6
PU5.0cPU	116.7 ± 49.6
PU7.5cPU	134.9 ± 43.9
PU2.5fPF	145.1 ± 45.9
PU5.05fPF	135.6 ± 53.2
PU7.5fPF	123.4 ± 53.4
PU2.5cPF	182.4 ± 69.2
PU5.0cPF	144.3 ± 55.5
PU7.5cPF	143.2 ± 83.2

The rather narrow distribution of cell size indicates that the foams exhibit overall homogeneous cellular structure. Neat PU has pores of 188.5 μm, while neat PF has pores of 62.9 μm. The lower pore size of PF foam could explain its lower thermal conductivity value with respect to PU sample. The introduction of the recycled foams considerably reduces the mean pore dimension, with a reduction up to 46 % in the case of PU7.5fPU sample. However, there is not a clear trend related to the granulometry and type of waste.

The values of theoretical density, geometrical density, apparent density, total and closed porosity are summarized in Table 7.6.

Table 7.6 Values of density and porosity of the prepared foams.

Samples	ϱ_{th} (g/cm³)	ϱ_{geom} (g/cm³)	ϱ_{app} (g/cm³)	P_{tot} (%)	P_{closed} (%)
PU	1.174 ± 0.003	0.044 ± 0.003	0.086 ± 0.009	96.3 ± 2.0	47.4 ± 2.0
PF	-	0.035 ± 0.003	-	-	-
PU2.5fPU	0.686 ± 0.004	0.057 ± 0.006	0.167 ± 0.002	92.1 ± 4.5	25.8 ± 2.5
PU5.0fPU	0.485 ± 0.003	0.062 ± 0.015	0.220 ± 0.007	87.5 ± 4.1	15.4 ± 0.2
PU7.5fPU	0.375 ± 0.012	0.059 ± 0.001	0.208 ± 0.013	84.0 ± 3.2	12.6 ± 1.5
PU2.5cPU	0.686 ± 0.004	0.049 ± 0.001	0.154 ± 0.007	92.2 ± 2.5	24.9 ± 1.1
PU5.0cPU	0.485 ± 0.003	0.048 ± 0.004	0.162 ± 0.010	90.1 ± 3.6	19.7 ± 1.1
PU7.5cPU	0.375 ± 0.012	0.058 ± 0.009	0.114 ± 0.040	85.7 ± 1.4	35.4 ± 1.1
PU2.5fPF	0.646 ± 0.011	0.055 ± 0.010	0.571 ± 0.024	92.3 ± 1.1	1.2 ± 1.1
PU5.0fPF	0.446 ± 0.007	0.048 ± 0.003	0.359 ± 0.013	89.3 ± 2.1	2.6 ± 0.2
PU7.5fPF	0.341 ± 0.003	0.050 ± 0.002	0.316 ± 0.008	87.1 ± 2.6	1.1 ± 0.2
PU2.5cPF	0.646 ± 0.011	0.052 ± 0.007	0.337 ± 0.026	92.6 ± 3.4	7.4 ± 0.1
PU5.0cPF	0.446 ± 0.007	0.055 ± 0.001	0.246 ± 0.002	88.9 ± 3.0	10.1 ± 0.1
PU7.5cPF	0.341 ± 0.003	0.059 ± 0.013	0.305 ± 0.039	93.6 ± 2.4	2.1 ± 1.5

Neat PU foam exhibits a theoretical density of 1.174 g/cm³. The introduction of both PU and PF recyclates, regardless of their granulometry, results in a reduction of the theoretical density. This is attributed to the substitution of the liquid precursors with a foamed filler, which has lower density values. Regarding the geometrical density, neat PU foam has density of 0.044 g/cm³, and the addition of the recycled foam leads to a slight increase in the geometrical density, without a clear dependency on the concentration, type and size of recyclate. A similar observation can be performed analyzing the apparent density values: the neat PU foam shows a ϱ_{app} value of 0.086 g/cm³, which increases upon the recyclate introduction. However, the addition of PF involves a stronger increase in ϱ_{app}, which can be due to a higher tendency of PF particles to form open

pores. In fact, their high polarity can cause a partial agglomeration of the particles and renders more difficult the foaming process [183]. Consequently, also the total porosity results to be slightly affected by the presence of the recycled foam particles. In particular, the addition of recycled filler, regardless of the type and size, lead to a reduction of total porosity, from 96.3% (neat PU) up to 84.0% (PU7.5fPU). Neat PU shows 47.4 % of closed porosity, which is strongly reduced upon the addition of fillers due to the partial breakage of the cell walls. It is important to underline that, closed porosity is more suitable for thermal insulation application, while open porosity is desirable when elevated acoustic insulation properties are required [191]. The incorporation of recycle PU particles involves a reduction of closed porosity from 47.4% up to 12.6% (see PU7.5fPU sample), whereas the addition of PF particles results in a P_{closed} reduction up to 1.1% (see PU7.5fPF foam). In general, also for closed porosity, there is no a clear influence of size of granulometry of both PU and PF recycled particles added to the foams.

7.2.3.2 Thermal conductivity analysis

Figure 7.15 shows the thermal conductivity (λ) values of the prepared foams at 10 °C.

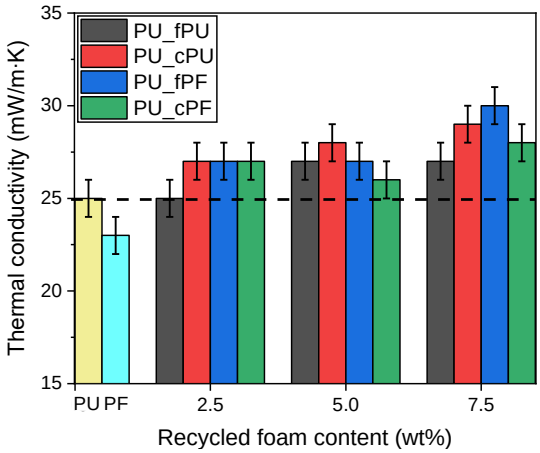

Figure 7.15 Thermal conductivity values at 10 °C of the prepared foams.

Neat PU has a λ value equal to 0.025 W/m·K, while neat PF has a λ value equal to 0.023 W/m·K, and these values are slightly higher than those reported in the datasheet of the producer. This is probably due to the non-optimal condition of the foaming process, that was performed by using a lab-made device. At a general level, the introduction of the PU and PF recyclates leads to a slight increase of the λ values of the foams. This fact is probably related to the lower values of closed porosity and also to the slight decrease of the total porosity induced by the recycled foam addition. Nevertheless, considering also the standard deviation values associated to the results, it can be clearly seen that this increase is very low, especially up to a recyclate amount of 5 wt%. The most remarkable λ enhancement can be observed in the case of PU7.5fPF foam, where an increase of 16% (0.030 W/m·K) is registered compared to the neat PU foam. However, this value of thermal conductivity still remains within the λ range of the most common thermal insulating foams diffused on the market [192]. In particular, it is interesting to observe how the insulating capacity of the PU foams containing recycled PF

particles is almost retained up to recyclate amount of 7.5 wt%, despite they experience a stronger reduction in the closed porosity. This suggests that the superior thermal insulation power of PF efficiently counteracts the P_{closed} reduction due to recycled PF addition. There is not a distinct trend associated with the recyclate content up to 5 wt%, and the most promising results come from the PU2.5fPU and PU5.0cPF foams, which practically show the same λ values of neat PU. In general, there is no clear influence of the particle size of both PU and PF recyclates on the final thermal conductivity of the foams.

7.2.3.3 Mechanical characterization

In Figure 7.16(a,b), representative stress-strain curves related to the flexural tests on the prepared foams are reported. In particular, Figure 7.16a shows the flexural behaviour of samples produced by using fPU and fPF recyclates, while in Figure 7.16b the flexural properties of samples obtained introducing cPU and cPF recycled foams are shown.

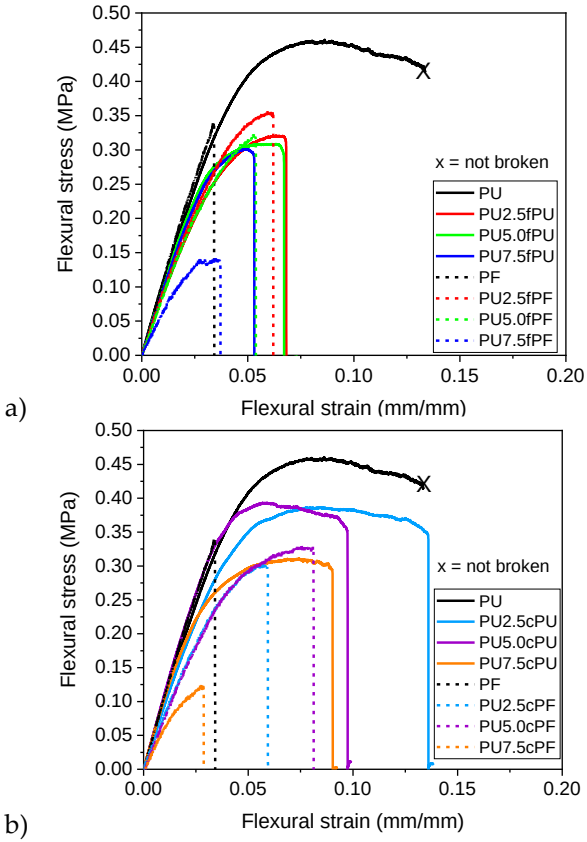

Figure 7.16 Representative stress-strain curves from flexural tests on the prepared foams. Neat PU, neat PF and foams prepared with different amounts of (a) fPU and fPF, (b) cPU and cPF recyclates.

In Table 7.7 the values of specific flexural modulus, flexural strength and strain at break are summarized.

Table 7.7 Flexural properties of the prepared foams.

Samples	E_f /ϱ (MPa/(g/cm³))	σ_f /ϱ (MPa/(g/cm³))	ϵ_f (mm/mm)
PU	216.4 ± 22.7	9.5 ± 1.6	-
PF	267.1 ± 97.3	10.0 ± 3.1	0.03 ± 0.01
PU2.5fPU	148.9 ± 24.1	5.8 ± 0.8	0.07 ± 0.01
PU5.0fPU	154.5 ± 44.2	4.7 ± 1.5	0.07 ± 0.02
PU7.5fPU	162.0 ± 9.2	5.1 ± 0.6	0.05 ± 0.01
PU2.5cPU	192.0 ± 10.9	8.2 ± 1.8	0.15 ± 0.04
PU5.0cPU	189.8 ± 20.6	7.9 ± 0.9	0.11 ± 0.03
PU7.5cPU	159.1 ± 37.5	6.0 ± 2.1	0.10 ± 0.04
PU2.5fPF	150.4 ± 31.9	6.4 ± 1.9	0.07 ± 0.03
PU5.0fPF	182.3 ± 30.4	6.7 ± 0.8	0.05 ± 0.02
PU7.5fPF	157.2 ± 32.3	3.0 ± 0.3	0.04 ± 0.02
PU2.5cPF	158.8 ± 28.3	6.0 ± 1.2	0.07 ± 0.02
PU5.0cPF	169.3 ± 18.4	7.8 ± 1.4	0.09 ± 0.04
PU7.5cPF	137.6 ± 60.5	3.1 ± 1.7	0.06 ± 0.01

Neat PU foam behaves as a ductile material under flexural conditions, and it does not break in the strain interval considered. On the other hand, PF foam shows a brittle behaviour, with a catastrophic failure at limited strain levels. Neat PU shows a specific flexural modulus of 216.4 MPa/(g/cm³) and a specific flexural strength of 9.5 MPa/(g/cm³), while neat PF shows an E_f/ϱ value of 267.1 MPa/(g/cm³) and a σ_f/ϱ value of 10.0 MPa/(g/cm³). The introduction of increasing amounts of PU in fine granulometry leads to a reduction in modulus and in strength (up to 28.7% and 50.5% for the PU5.0fPU sample, respectively), and to a general embrittlement, with a strong reduction of ϵf values. On the other hand, the introduction of PF in fine granulometry has a stronger effect on flexural modulus and strength, with an even more evident degradation of both the properties. In fact, the flexural modulus of the PU7.5fPF foam is 157.2 MPa/(g/cm³) (-27.4% than PU) and the

flexural strength is 3.0 MPa/(g/cm^3) (-68.4% than PU). Regarding the samples containing recyclates with coarse granulometry, it can be noticed that the addition of 7.5 %wt of cPU and 7.5 %wt cPF leads to the reduction of the flexural modulus of 26.5 % and 36.4 %, respectively, and to the reduction of the flexural strength of 36.8 % and 67.4 %, respectively. The general decline in properties may be attributed to a poor adhesion between the polyurethane matrix and the recyclates and a non-uniform distribution of the fillers in the matrix that may compromise mechanical properties and overall durability. Additionally, the presence of open porosity within the material can contribute to decreased structural integrity and susceptibility to moisture absorption or other environmental factors, further compromising its performance.

In Figure 7.17(a,b) representative stress-strain curves related to the compression tests on the prepared foams are reported. In particular, Figure 7.17a shows the compressive behaviour of samples produced by using fPU and fPF recyclates, while in Figure 7.17b the compression properties of samples obtained introducing cPU and cPF recycled foams are shown.

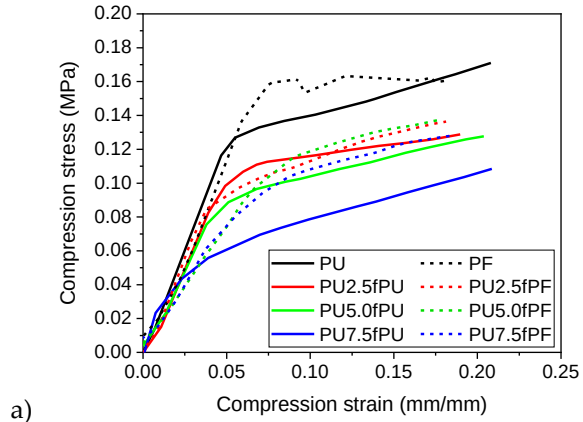

a)

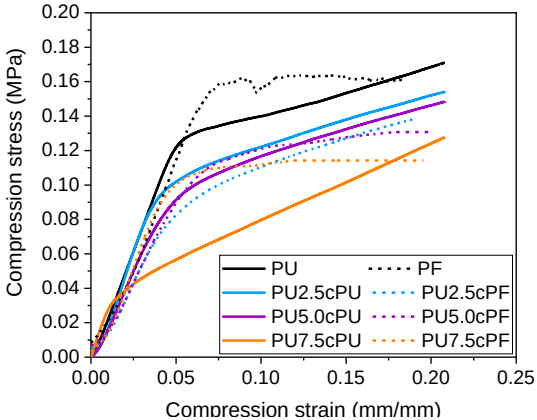

b)

Figure 7.17 Representative stress-strain curves from compression tests on the prepared foams. Neat PU, neat PF and foams prepared with different amounts of (a) fPU and fPF, (b) cPU and cPF recyclates.

In Table 7.8 the results of compression tests, expressed in terms of specific compressive modulus and strength, are numerically summarized.

Table 7.8 Results of quasi-static compressive tests on the prepared foams.

Samples	E_c/ϱ (MPa/(g/cm^3))	σ_c/ϱ (MPa/(g/cm^3))
PU	75.9 ± 20.6	3.2 ± 0.7
PF	81.4 ± 20.1	4.3 ± 0.5
PU2.5fPU	59.6 ± 12.9	1.9 ± 0.9
PU5.0fPU	37.6 ± 18.2	1.5 ± 0.7
PU7.5fPU	55.3 ± 13.3	1.2 ± 0.5
PU2.5cPU	71.6 ± 6.2	2.7 ± 0.5
PU5.0cPU	54.6 ± 12.5	2.5 ± 0.6
PU7.5cPU	48.3 ± 23.2	1.0 ± 0.5
PU2.5fPF	51.8 ± 12.7	2.7 ± 0.9
PU5.0fPF	61.0 ± 5.5	2.7 ± 0.4
PU7.5fPF	57.4 ± 8.3	2.8 ± 0.7
PU2.5cPF	53.7 ± 9.7	2.1 ± 0.5
PU5.0cPF	36.4 ± 3.4	2.5 ± 0.6
PU7.5cPF	45.9 ± 15.7	2.9 ± 0.9

The introduction of increasing amounts of PU particles in fine granulometry leads to a slight reduction in the compressive modulus and a stronger reduction in compressive strength. In particular, neat PU shows compressive modulus of 75.9 MPa/(g/cm^3) and a compressive strength of 3.2 MPa/(g/cm^3), while PU7.5fPU sample show a compressive modulus of 55.3 MPa/(g/cm^3) (-27.1 % than PU) and compressive strength of 1.2 MPa/(g/cm^3) (-62.5 % than PU). On the other hand, the introduction of PF in fine granulometry has a milder effect on the compressive strength and a stronger effect on the compressive modulus. In fact, by introducing 7.5%wt of fPF, the compressive strength results 2.8 MPa/(g/cm^3), but the modulus is reduced of about 24.4%. The use of a recyclate with a coarser granulometry seems to have a stronger effect in the compressive properties than those exhibited in flexural mode. In fact, the

introduction of 7.5 %wt of cPU and cPF leads to a reduction of the compressive modulus of 36.4 % and 39.5 %, respectively, and a reduction of the compressive strength of 68.7 % and 9.3 %, respectively. Even in compression, the overall decrease in properties can be attributed to poor adhesion between the polyurethane matrix and recycled materials, irregularities in morphology, such as uneven filler distribution or the formation of an inconsistent structure, and the existence of open porosity within the material. In future work, a compatibility agent could be used to improve the compatibility between the matrix and the fillers at interfacial level.
At the end of the morphological and thermo-mechanical characterization, the following samples were selected as the most promising for subsequent reaction to resistance to fire characterization: PU, PF, PU5.0cPU, PU5.0fPF, PU5.0cPF, PU7.5cPF.

7.2.3.4 Forced combustion tests

On the basis of the results of the morphological and thermo-mechanical characterization, the most promising compositions, showing the best balance of physical properties, were identified and utilized in forced combustion tests. In particular, the reaction to fire of the neat PU and PF foams and of the PU5.0cPU, PU5.0fPF, PU5.0cPF, PU7.5cPF samples has been investigated by cone calorimetry measurements. The aim is to evaluate whether the inclusion of recycled PU and PF particles had a negative impact on the foam burning behavior. The tests have been performed under an irradiative heat flux of 35 kW/m^2, which is normally related to the early stages of a developing fire [193]. When exposed to the selected heat flux, the sample releases combustible volatiles that, upon reaching the flammability limits, lead to the flaming combustion of the specimen. The instrument then evaluates the heat release rate (HRR) and the smoke production rate (SPR) as a function of time. Figure 7.18(a-f) reports the collected plots and integral values (THR and TSR for heat and fumes, respectively) as well as histograms

related to the peak of heat release rate and final residue. Table 7.9 collects all the measured parameters.

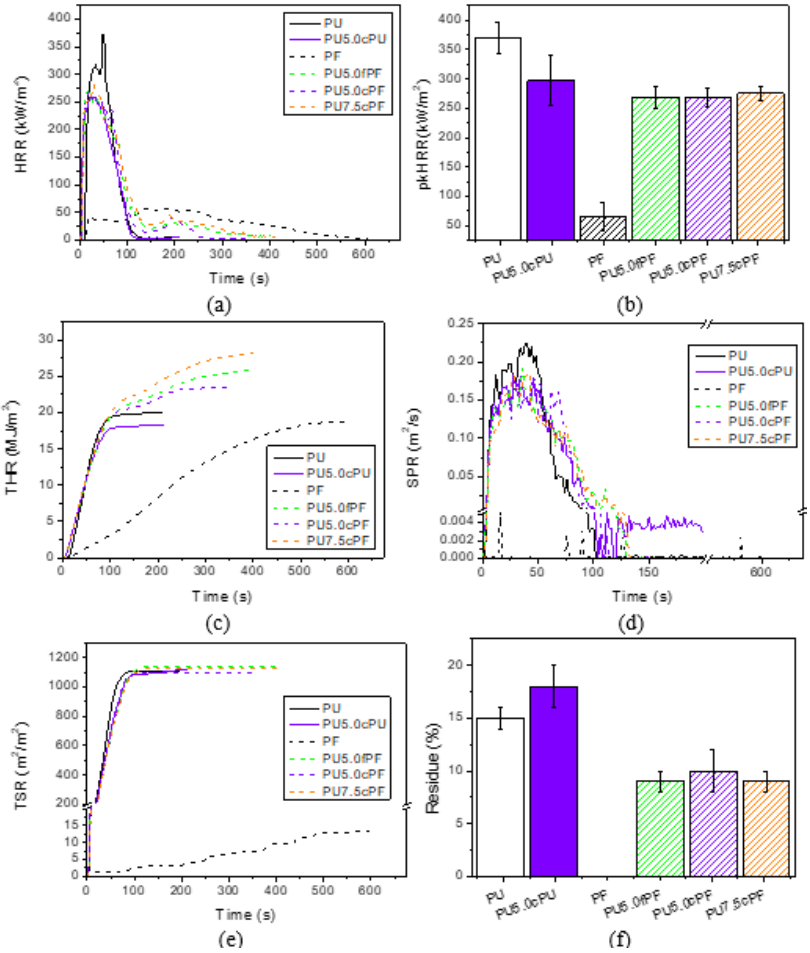

Figure 7.18 Cone calorimetry tests of neat PU, neat PF and recycled foams, (a) heat release rate (HRR), (b) peak heat release rate (pkHRR), (c) total heat release (THR), (d) smoke production rate (SPR), (e) total smoke release (TSR), (f) residue at the end of cone calorimetry.

Table 7.9 Results of cone calorimetry tests of neat PU, neat PF and the foams with optimized composition.

Sample	TTI (s)	HRR (kW/m²)	pkHRR (kW/m²)	THR (MJ/m²)	TSR (m²/m²)	Residue (%)
PU	4 ± 1	96 ± 8	370 ± 26	20.0 ± 0.1	1160 ± 100	15 ± 1
PF	10 ± 2	29 ± 3	52 ± 6	19.1 ± 0.3	9 ± 4	<1
PU5.0cPU	2 ± 1	91 ± 8	297 ± 43	19.3 ± 2.1	1164 ± 55	18 ± 2
PU5.0fPF	3 ± 1	70 ± 9	269 ± 19	25.8 ± 2.0	1141± 130	9 ±1
PU5.0cPF	3 ± 1	68 ± 8	268 ± 16	25.0 ± 3.6	1163 ± 143	10 ± 2
PU7.5cPF	3 ± 1	71 ± 3	275 ± 11	26.4 ± 2.0	1121 ± 17	9 ± 1

Figure 7.19 and Figure 7.20 collect pictures and SEM micrographs of residues of neat and recycled foams after cone calorimetry test.

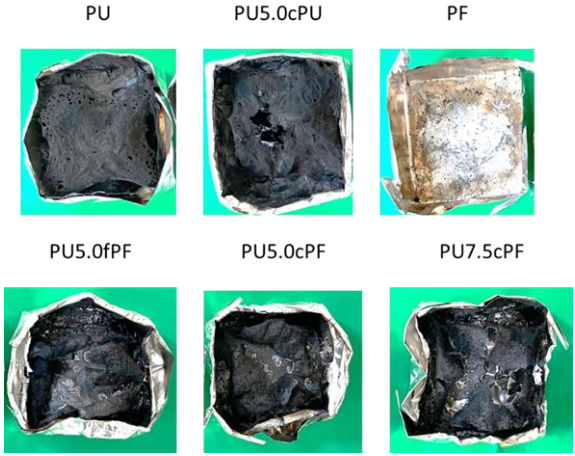

Figure 7.19 Pictures of residues of neat and recycled foams after cone calorimetry test.

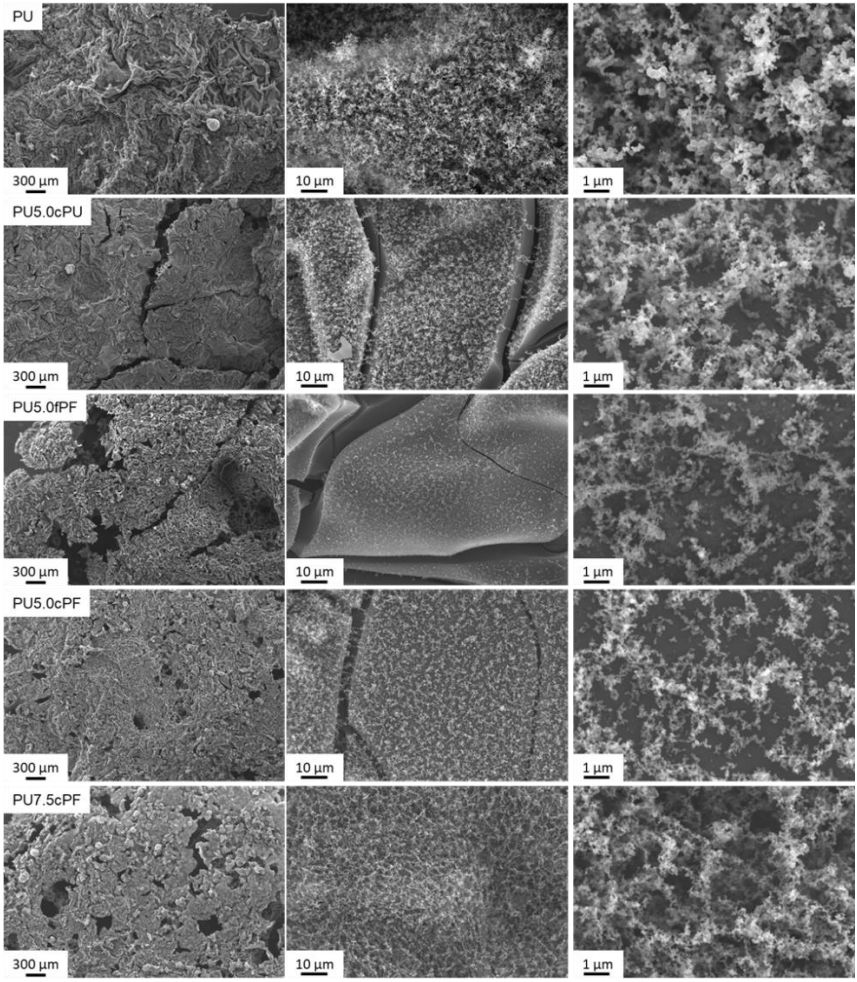

Figure 7.20 SEM micrographs of residues of the prepared foams collected after cone calorimetry test.

Upon exposure to the cone heat flux, the PU quickly ignites and burns with vigorous flames. The HRR plots steeply increases reaching a pkHRR at 370 ± 26 kW/m^2. During combustion, the foam

structure is gradually consumed leaving a thin and dense charred residue, which accounts for 15% of the original weight. By contrast, the neat PF shows extensive char formation that results in limited HRR values (pkHRR 52 ± 6 kW/m^2) as well as reduced amount of smoke released. After the flame extinguishes, the charred residue is completely consumed by smoldering combustion (i.e. flameless combustion characterized by low HRR values). This behaviour is a well-known characteristic of PF and extends the overall testing time [194,195].

As far as the recycled samples are concerned, the inclusion of cPU particles does not modify the burning behaviour of the neat PU but produces a reduction in pkHRR (-20%) and a slight increase in the final residue (+20%). The other parameters remain mostly unchanged and within the experimental error. Similarly, during flaming combustion, the good char forming ability and low HRR of PF particles produces a substantial reduction in the pkHRR (up to -28% for PU5.0cPF). As the flame extinguishes, as already observed for the neat PF, the characteristic smoldering behaviour of this latter is also displayed by the recycled foams. This is apparent from the low and prolonged HRR signal collected for samples PU5.0cPF, PU5.0fPF and PU7.5cPF after flame out. The smoldering duration seems to be directly related to the PF concentration. Interestingly, despite a different PF concentration, PU5.0fPF and PU7.5cPF show a similar behaviour thus suggesting an effect of the granulometry where the higher surface exposed of the fine particles likely compensates for their reduced amount in the recycled foam with respect to the coarse ones. The occurrence of a smoldering combustion produces an increase in the THR and a subsequent reduction of the final residue. Smoke parameters remain unchanged with respect to the neat PU. The post combustion residues have been investigated by SEM (Figure 7.20). The performed micrographs point out no substantial differences between the neat PU and the PU5.0cPU highlighting the formation of a dense and compact char layer for both samples. Conversely, PF containing samples yield partially damaged

structures characterized by holes that are likely ascribed to the observed smoldering behaviour. From an overall point of view the inclusion of mechanically recycled particles results in a positive effect by reducing the pkHRR that is often considered as one of the main fire safety parameters [196].

7.2.3.5 General comparison of properties

A general comparison between the most important physical properties of the investigated foams is shown in Figure 7.21 as radar plot. This comparative analysis has been performed in terms of thermal conductivity (λ), specific flexural modulus (E_f/ϱ) and strength (σ_f/ϱ), specific compression modulus (E_c/ϱ) and strength (σ_c/ϱ), and peak heat release rate (pkHRR).

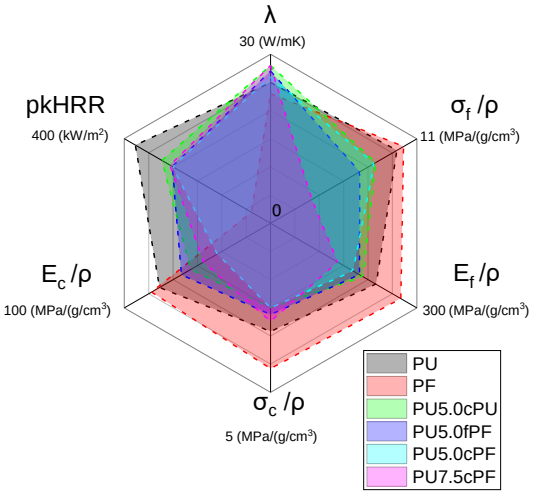

Figure 7.21 Radar plot of the main physical properties of the investigated foams, specifically thermal conductivity (λ), specific flexural modulus (E_f/ϱ) and strength (σ_f/ϱ), specific compression modulus (E_c/ϱ) and strength (σ_c/ϱ), and peak heat release rate (pkHRR).

From the radar plots, it is evident the difference in properties between the samples that incorporate PU or PF recyclates compared to neat PU foam. PU foam shows a balanced distribution of properties from both mechanical and thermal point of view. However, its reaction to fire, expressed by the peak heat release rate (pkHRR), is significantly high, reaching a value of 370 ± 26 kW/m^2. This implies a higher heat release during combustion and faster burning, increasing the risk of fire spread. On the other hand, neat PF foam exhibits slightly superior mechanical properties, although the material is inherently more brittle compared to PU. Additionally, PF foam shows lower thermal conductivity than PU, making it more effective as a thermal insulator. The main advantage of PF foam is the significant decrease in pkHRR, which is around 52 ± 6 kW/m^2, compared to neat PU foam. This value is particularly important in terms of fire safety, as it indicates lower heat release and slower burning, thus reducing the risk of fire spread and providing more time for evacuation. However, it should be noted that the introduction of recycled foams compromises, albeit not drastically, the flexural and compressive properties if compared with neat PF foam. In particular, both samples with the highest PU and PF recyclate content shows the greatest reduction in mechanical properties, especially under bending conditions. On the other hand, the thermal conductivity is not substantially compromised by the addition of recycled foams. In the case of recycled PF particles, their higher thermal insulating performance counterbalances the negative effects on the foam morphology. Among the samples tested, the most promising results emerge for the PU5.0fPF foam, as it highlights a suitable combination of mechanical strength, thermal insulating performance, and fire behaviour.

7.2.4 Conclusions

In this work, a comprehensive analysis of the mechanical recycling process of polyurethane (PU) and phenolic foam (PF) was conducted, to provide a sustainable solution for the management of

their end-of-life. PU and PF panels were ground into two different particle sizes and gradually incorporated into expanded PU at increasing weight concentrations, to progressively reduce the use on virgin materials and to promote a more extensive use of recycled materials. The new formulations were characterized by a morphological and thermo-mechanical point of view. Field emission scanning electron microscopy revealed a consistent cell structure in the new formulations, due to an efficient wetting by the PU liquid precursors which allowed an effective foaming process. The incorporation of the recyclates led to a slight increase in foam densities, thus resulting in reduced closed porosity. This contributed to a slight rise in thermal conductivity of up to 16% than neat PU. However, this minor increase did not compromise the excellent thermal insulating properties of the new formulations, particularly at recyclate levels below 5% by weight. On the other hand, although the addition of recyclates marginally improved thermal stability, it adversely affected the flexural and compression properties possibly due to poor adhesion between fillers and PU matrix and the presence of open porosity. Nonetheless, according to cone calorimetry tests, the inclusion of particles notably reduced the peak heat release rate by 28% compared to neat PU, improving fire safety. Overall, the properties studied remained unaffected by the recycled particle size, which, in a practical application, would allow for a simpler recycling methodology, without the need for a specific recycled particle size to achieve good performance.

8 Bibliography

1. Sanjay, M.R.; Arpitha, G.R.; Yogesha, B. Study on Mechanical Properties of Natural - Glass Fibre Reinforced Polymer Hybrid Composites: A Review. *Materials Today: Proceedings* **2015**, *2*, 2959-2967.
2. Ashok, N.S.; Kumbar, R.; Madhusudhan, T. Investigation on Mechanical and Tribological Properties of 6061 Aluminium–SiC Alloy Fabricated by Stir Casting Method and Equal Channel Angular Extrusion: The Review. *International Research Journal of Engineering and Technology* **2016**, *3*, 1-4.
3. Yang, Y.; Boom, R.; Irion, B.; Van Heerden, D.J.; Kuiper, P.; De Wit, H. Recycling of composite materials. *Chemical Engineering and Processing: Process Intensification* **2012**, *51*, 53-68.
4. Park, S.J.; Seo, M.K. Composite Characterization. In *Interface Science and Technology*; Ed.; Series in; Elsevier: Amsterdam (Netherlands), **2011**; pp. 631-738.
5. CKN. Composite properties: Micro-Mechanics. Available online: https://compositeskn.org (accessed on July 2023).
6. Eager, T.W. Whither advanced materials? *Advance Material Processes* **1991**, *1*, 25-29.
7. Kim, S.J.; Shin, E.S. A thermoviscoplastic theory for composite materials by using a matrix-partitioned unmixing-mixing scheme. *Journal of Composite Materials* **1996**, *30*, 1647-1669.
8. Callister, W.; Rethwisch, D. *Scienza e Ingegneria dei Materiali*. Edises: Napoli (Italy) **2019**, 43-46.
9. Vuksanovic, M.; Tomic, N.; Medjo, B.; Jancic Heinemann, R.; Rakin, M.; Volkov Husovic, T. Modeling of the mechanical behavior of fiber-reinforced ceramic composites using finite element method (FEM). *Science of Sintering* **2014**, *46*, 385–390.

10. Abouelleil, H.; Pradelle, N.; Villat, C.; Attik, N.; Colon, P.; Grosgogeat, B. Comparison of mechanical properties of a new fiber reinforced composite and bulk filling composites. *Restorative dentistry & endodontics* **2015**, *40*, 262-270.
11. Silu, H.; Bo, W.; Libo, Y. Interphase and Interfacial Properties of Composite Materials. In *Composite Materials: Manufacturing, Properties and Applications*; Ed.; Series in; Elsevier: Amsterdam (Netherlands), **2021**; pp. 151-177.
12. Mazov, I.; Burmistrov, I.; Il'inykh, I.; Stepashkin, A.; Kuznetsov, D.; Issi, J.P. Anisotropic thermal conductivity of polypropylene composites filled with carbon fibers and multiwall carbon nanotube. *Polymer Composites* **2015**, *36*, 1951-1957.
13. Bishay, I.K.; Abd-El-Messieh, S.L.; Mansour, S.H. Electrical, mechanical and thermal properties of polyvinyl chloride composites filled with aluminum powder. *Materials & Design* **2011**, *32*, 62-68.
14. Shen, D.; Zhan, Z.; Liu, Z.; Cao, Y.; Zhou, L.; Liu, Y.; Dai, W.; Nishimura, K.; Li, C.; Lin, C.T. Enhanced thermal conductivity of epoxy composites filled with silicon carbide nanowires. *Scientific Reports* **2017**, *7*, 2606-2617.
15. Rahman, M.Z.; Jayaraman, K.; Mace, B.R. Vibration damping of flax fibre-reinforced polypropylene composites. *Fibers and Polymers* **2017**, *18*, 2187-2195.
16. Lee, H.P.; Ng, B.M.P.; Rammohan, A.V.; Tran, L.Q. An investigation of the sound absorption properties of flax/epoxy composites compared with glass/epoxy composites. *Journal of Natural Fibers* **2017**, *14*, 71-77.
17. Singh, K.K.; Shinde, M. Low Velocity Impact on Fibre Reinforced Polymer Composite Laminates. *Impact Behavior of Fibre Reinforced Laminates* **2022**, *1*, 83-105.
18. Lamotte, E.D.; Perry, A.J. Diameter and strain-rate dependence of the ultimate tensile strength and Young's modulus of carbon fibres. *Fibre Science and Technology* **1970**, *3*, 157-166.

19. Bakir, B.; Hashem, H. Effect of fiber orientation for fiber glass reinforced composite material on mechanical properties. *International Journal of Mining, Metallurgy and Mechanical Engineering* **2013**, *1*, 341-345.
20. Sathishkumar, T.P.; Satheeshkumar, S.; Naveen, J. Glass iber-reinforced polymer composites–a review. *Journal of Reinforced Plastics and Composites* **2014**, *33*, 1258-1275.
21. Li, H.; Charpentier, T.; Du, J.; Vennam, S. Composite reinforcement: Recent development of continuous glass fibers. *International Journal of Applied Glass Science* **2017**, *8*, 23-36.
22. Li, R.X.; Zhang, Y. Magnetic Fibers. In *Magnetic sensors-development trends and applications*; Ed.; Series in; Intech: Rijeka (Croatia), **2017**; pp. 3-13.
23. Malkin, A.Y.; Isayev, A.I. Applications of Rheology. In *Rheology Concepts, Methods, and Applications*; Elsevier, Ed.; Series in, **2012**; pp. 365 – 420.
24. Zhang, D. *Advances in Filament Yarn Spinning of Textiles and Polymers*. Elsevier: Amsterdam (Netherlands) **2014**, 56-65.
25. Newcomb, B.A. Processing, structure, and properties of carbon fibers. *Composites Part A: Applied Science and Manufacturing* **2016**, *91*, 262-282.
26. Tang, S.; Hu, C. Design, Preparation and Properties of Carbon Fiber Reinforced Ultra-High Temperature Ceramic Composites for Aerospace Applications: A Review. *Journal of Materials Science & Technology* **2017**, *33*, 117-130.
27. Ahmad, H.; Markina, A.A.; V., P.M.; Ahmad, F. A review of carbon fiber materials in automotive industry. *Materials Science and Engineering* **2020**, *971*, 1-11.
28. Zhang, J.; Lin, G.; Vaidya, U.; Wang, H. Past, present and future prospective of global carbon fibre composite developments and applications. *Composites Part B: Engineering* **2023**, *250*, 1-19.
29. Hassan, M.F.; Sabri, M.A.; Fazal, H.; Hafeez, A.; Shezad, N.; Hussain, M. Recent trends in activated carbon fibers

production from various precursors and applications—A comparative review. *Journal of Analytical and Applied Pyrolysis* **2020**, *145*, 1-22.

30. Huang, X. Fabrication and Properties of Carbon Fibers. *Materials* **2009**, *2*, 2369-2403.
31. Naskar, M. Polymer nanocomposites for structure and construction applications. *Properties and Applications of Polymer Nanocomposites: Clay and Carbon Based Polymer Nanocomposites* **2017**, *1*, 37-57.
32. Jamshaid, H.; Mishra, R. A green material from rock: basalt fiber – a review. *The Journal of The Textile Institute* **2015**, *107*, 923-037.
33. Dhand, V.; Mittal, M.; Rhee, K.Y.; Park, S.J.; Hui, D. A short review on basalt fiber reinforced polymer composites. *Composites Part B: Engineering* **2015**, *73*, 166-180.
34. JKumbhar, V.P. An overview: basalt rock fibers-new construction material. *Acta Engineering International* **2014**, *2*, 11-18.
35. Chowdhury, I.R.; Pemberton, R.; Summerscales, J. Developments and Industrial Applications of Basalt Fibre Reinforced Composite Materials. *Journal of Composites Science* **2022**, *6*, 367-393.
36. Nulkar, S. Are There Chemical Limits To Recycling Everything? Available online: https://www.scienceabc.com/ (accessed on July 2023).
37. Huang, S.; Bo, W.; Libo, Y. Interphase and interfacial properties of composite materials. *Composite Materials* **2021**, *1*, 151-177.
38. Pratibha, D.; Sreekara Reddy, M.B.S. Aramid fibre as potential reinforcement for polymer matrix composites: a review. *Emergent Materials* **2022**, *5*, 1561-1578.
39. Jin, F.L.; Li, X.; Park, S.J. Synthesis and application of epoxy resins: A review. *Journal of Industrial and Engineering Chemistry* **2015**, *29*, 1-11.
40. May, C. Epoxy Resins: Chemistry and Technology. *Taylor and Francis* **1987**, *1*, 1-10.

41. Moosburger-Will, J.; Greisel, M.; Sause, M.G.; Horny, R.; Horn, S. Influence of partial cross-linking degree on basic physical properties of RTM6 epoxy resin. *Journal of Applied Polymer Science* **2013**, *130*, 4338-4346.
42. Casati, R.; Vedani, M. Metal matrix composites reinforced by nano-particles—a review. *Metals* **2014**, *4*, 65-83.
43. Ramnath, B.V.; Elanchezhian, C.; Annamalai, R.M.; Aravind, S.; Atreya, T.S.; Vignesh, V.; Subramanian, C. Aluminium metal matrix composites–a review. *Reviews on Advanced Materials Science* **2014**, *38*, 55-60.
44. Rawal, S.P. Metal-matrix composites for space applications. *Journal of The Minerals, Metals & Materials Society* **2001**, *53*, 14-17.
45. Arai, Y.; Inoue, R.; Goto, K.; Kogo, Y. Carbon fiber reinforced ultra-high temperature ceramic matrix composites: A review. *Ceramics International* **2019**, *45*, 14481-14489.
46. Hu, C.; Li, F.; Qu, D.; Wang, Q.; Xie, R.; Zhang, H.; Peng, S.; Bao, Y.; Zhou, Y. Developments in hot pressing (HP) and hot isostatic pressing (HIP) of ceramic matrix composites. In *Advances in Ceramic Matrix Composites* Woodhead, Ed.; Series in, **2014**; pp. 177-202.
47. Schmidt, S.; Beyer, S.; Knabe, H.; Immich, H.; Meistring, R.; Gessler, A. Advanced ceramic matrix composite materials for current and future propulsion technology applications. *Acta Astronautica* **2004**, *55*, 409-420.
48. Karger-Kocsis, J.; Mahmood, H.; A., P. Recent advances in fiber/matrix interphase engineering for polymer composites. *Progress in Materials Science* **2015**, *73*, 1-43.
49. Hao Zheng, H.; Zhang, W.; Li, B.; Zhu, J.; Wang, C.; Song, G.; Wu, G.; Yang, X.; Huang, Y.; Ma, L. Recent advances of interphases in carbon fiber-reinforced polymer composites: A review. *Composites Part B: Engineering* **2022**, *233*, 109639-109658.
50. Xu, Z.; Sun, X.; Xiong, K.; Chen, Z.; Shang, Y.; Guo, R.; Cai, S.; Zheng, C. A review of the research progress on the

interface between oxide fiber and oxide ceramic matrix. *Ceramics International* **2021**, *47*, 5896-5908.

51. Schadler, L. The Elusive Interphase/Interface in Polymer Nanocomposites. In *Comprehensive Composite Materials*; Ed.; Series in; Elsevier: Amsterdam (Netherlands), **2018**; pp. 52-72.
52. Da Silva, L.; Ochsner, A.; Adams, R. *Handbook of Adhesion Technology*. Springer: Berlin (Germany) **2011**, 126-135.
53. Romanowic, P.; Muc, A. Estimation of Notched Composite Plates Fatigue Life Using Residual Strength Model Calibrated by Step-Wise Tests. *Materials* **2018**, *11*, 2180-2199.
54. Ramesch, T. Assessment of the fundamentals of failure theories for composite materials. *Composites Science and Technology* **2014**, *105*, 190-201.
55. Wu, Q.; Wan, Q.; Yang, X.; Wang, F.; Zhu, F. Effects of chain length of polyether amine on interfacial adhesion of carbon fiber/epoxy composite in the absence or presence of polydopamine bridging platform. *Applied Surface Science* **2021**, *547*, 1-9.
56. Li, H.; Wang, Y.; Zhang, C.; Zhang, B. Effects of thermal histories on interfacial properties of carbon fiber/polyamide 6 composites: Thickness, modulus, adhesion and shear strength. *Composites Part A: Applied Science and Manufacturing* **2016**, *85*, 31-39.
57. Pearson, A.; Liao, W.; Kazemi, Y.; Duncan, M.; Slingerland, E.; Kakroodi, A.; Heydrich, M.; Hammami, A.; Naguib, H.E. Fiber-matrix adhesion between high-density polyethylene and carbon fiber. *Polymer Testing* **2022**, *105*, 107423-107431.
58. Thomason, J.L.; Yang, L. Temperature dependence of the interfacial shear strength in glass–fibre epoxy composites. *Composites Science and Technology* **2014**, *96*, 7-12.
59. Pisanova, E.; Dutschk, V.; Lauke, B. Work of adhesion and local bond strength in glass fibre-thermoplastic polymer

systems. *Journal of Adhesion Science and Technology* **2012**, *12*, 305-322.

60. Pearson, A.; Duncan, M.; Hammami, A.; Naguib, H.E. Effect of temperature on the fiber-matrix adhesion in glass fiber reinforced thermoplastics. *Composites Science and Technology* **2022**, *230*, 1-9.
61. Khandelwal, S.; Rhee, K.Y. Recent advances in basalt-fiber-reinforced composites: Tailoring the fiber-matrix interface. *Composites Part B: Engineering* **2020**, *192*, 1-13.
62. Yua, S.; Oh, K.H.; Hwangc, J.Y.; Honga, S.H. The effect of amino-silane coupling agents having different molecular structures on the mechanical properties of basalt fiber-reinforced polyamide 6,6 composites. *Composites Part B: Engineering* **2019**, *163*, 511-521.
63. Valadez-Gonzalez, A.; Cervantes-Uc, J.M.; Olayo, R.; P., H.-F.J. Effect of fiber surface treatment on the fiber–matrix bond strength of natural fiber reinforced composites. *Composites Part B: Engineering* **1999**, *30*, 309-320.
64. Ali Kandemir, A.; Pozegic, T.R.; Hamerton, I.; Eichhorn, S.J.; Longana, M.L. Characterisation of Natural Fibres for Sustainable Discontinuous Fibre Composite Materials. *Materials* **2020**, *13*, 1-17.
65. Goucher, F.S.; Ward, H. A problem in viscosity. *Philosofical Megazine* **1922**, *44*, 675-684.
66. De Ryck, A.; Quéré, D. Inertial coating of a fibre. *Journal of Fluid Mechanics* **1996**, *311*, 219-237.
67. Simonini, L.; Mahmood, H.; Dorigato, A.; Pegoretti, A. Evaluation of self-healing capability of a polycaprolactone interphase in epoxy/glass composites. *Composites Part A: Applied Science and Manufacturing* **2023**, *169*, 107539-107548.
68. Bryce, D.; Thomason, J.L.; Yang, L. Thermoset droplet performance in the microbond test. *Composites Interfaces* **2023**, *1*, 1-10.
69. Thomason, J.; Yang, L. The influence of thermal stress on the interface strength of a fibre-reinforced thermoplastic

investigated by a novel single fibre technique. In Proceedings of the ECCM10, Brugge (Belgium), June 3-7, **2010**, 1-14.

70. Fibrobotics, O. Short fibre characterization and manipulation platform. Available online: https://fibrobotics.com (accessed on October 2023).
71. Sharma, M.; Gao, S.; Mader, E.; H., S.; Wei, L.Y.; Bijwe, J. Carbon fiber surfaces. *Carbon Fiber Surfaces and Composite Interphases* **2014**, *102*, 35-50.
72. Xu, L.; Drzal, L.T. Improvement of adhesion between vinyl ester resin and carbon fibers. In Proceedings of the ICCM13, Beijing (China), June 25-29, **2013**, 1-10.
73. Hossain, M.K.; Chowdhury, M.M.R.; Salam, M.B.; Malone, J.; Hosur, M.V.; Jeelani, S. Improved thermomechanical properties of carbon fiber reinforced epoxy composite using amino functionalized XDCNT. *Journal of Applied Polymer Science* **2014**, *131*, 1-12.
74. Czigan, T.; Poloskei, K.; Karger-Kocsis, J. Fracture and failure behavior of basalt fiber mat-reinforced vinylester/epoxy hybrid resins as a function of resin composition and fiber surface treatment. *Journal of Materials Science and Technology* **2005**, *40*, 5609-5618.
75. Mahmood, H.; Vanzetti, L.; Bersani, M.; Pegoretti, A. Mechanical properties and strain monitoring of glass-epoxy composites with graphene-coated fibers. *Composites Part A: Applied Science and Manufacturing* **2018**, *107*, 112-123.
76. Jones, A.R.; Blaiszik, B.J.; White, S.R.; Sottos, N.R. Full recovery of fiber/matrix interfacial bond strength using a microencapsulated solvent-based healing system. *Composites Science and Technology* **2013**, *79*, 1-7.
77. Bleay, S.M.; Loader, C.B.; Hawyes, V.J.; Humberstone, L.; Curtis, P.T. A smart repair system for polymer matrix composites. *Composites Part A: Applied Science and Manufacturing* **2001**, *32*, 1767-1776.
78. Norris, C.J.; Meadway, G.J.; O'Sullivan, M.J.; Bond, I.P.; Trask, R.S. Self-healing fibre reinforced composites via a

bioinspired vasculature. *Advanced Functional Materials* **2011**, *21*, 3624-3633.

79. Zhang, W.; Duchet, J.; Gerard, J.F. Self-healable interfaces based on thermo-reversible Diels–Alder reactions in carbon fiber reinforced composites. *Journal of Colloid and Interface Science* **2014**, *430*, 61-68.
80. Zhang, H.; Lamnawar, K.; Maazouz, A. Rheological modeling of the diffusion process and the interphase of symmetrical bilayers based on PVDF and PMMA with varying molecular weights. *Rheologica Acta* **2012**, *51*, 691-711.
81. Wu, D.Y.; Meure, S.; Solomon, D. Self-healing polymeric materials: A review of recent developments. *Progress in polymer science* **2008**, *33*, 479-522.
82. Wu, D.Y.; Sam Meure, S.; Solomon, D. Self-healing polymeric materials: A review of recent developments. *Progress in Polymer Science* **2008**, *33*, 479-522.
83. Islam, S.; Bhat, G. Progress and challenges in self-healing composite materials. *Materials Advances* **2012**, *2*, 1896-1926.
84. Chandra, R.; Singh, S.P.; Gupta, K. Damping studies in fiber-reinforced composites–a review. *Composites Structure* **1999**, *46*, 41-51.
85. Rao, V.; Herrera-Franco, P.; Ozzello, A.D.; Drzal, L.T. A direct comparison of the fragmentation test and the microbond pull-out test for determining the interfacial shear strength. *Journal of Adhesion* **1991**, *34*, 65-77.
86. Zinck, P.; Wagner, H.D.; Salmon, L.; Gerard, J.F. Are microcomposites realistic models of the fiber/matrix interface? II: Physico-chemical approach. *Polymer* **2000**, *42*, 6641-6650.
87. Wagner, H.D. Interfaces in microcomposites and macrocomposites: the issue of thermal residual stresses. *Composite Interfaces* **1994**, *2*, 312-336.
88. Gaur, U.; Miller, B. Microbond method for determination of the shear strength of a fiber/resin interface: Evaluation of

experimental parameters. *Composites Science and Technology* **1989**, *34*, 35-51.

89. Gurvich, M.R.; Dibenedetto, A.; Pegoretti, A. Evaluation of the statistical parameters of a Weibull distribution. *Journal of Materials Science* **1997**, *32*, 3711-3716.
90. R'Mili, M.; Bouchaour, T.; Merle, P. Estimation of Weibull parameters from loose-bundle tests. *Composites Science and Technology* **1996**, *56*, 831-834.
91. Andersons, J.; Joffe, R.; Hojo, M.; Ochiai, S. Glass fibre strength distribution determined by common experimental methods. *Composites Science and Technology* **2002**, *62*, 131-145.
92. Galembeck, F.; Burgo, T.A.; Balestrin, L.B.; Gouveia, R.F.; Silva, C.A.; Galembeck, A. Friction, tribochemistry and triboelectricity: recent progress and perspectives. *Royale Society of Chemistry* **2014**, *4*, 64280-64298.
93. Thomas, S.W.; Vella, S.J.; Kaufman, G.K.; Whiteside, G.M. Patterns of electrostatic charge and discharge in contact electrification. *Angewandte Chemie International Edition* **2008**, *47*, 6654-6656.
94. Mahmood, H.; Dorigato, A.; Pegoretti, A. Temperature dependent strain/damage monitoring of glass/epoxy composites with graphene as a piezoresistive interphase. *Fibers* **2019**, *7*, 1-15.
95. Tripathi, M.; Mahmood, H.; Novel, D.; Iacob, L.; Vanzetti, L.; Bartali, R.; Speranza, G.; Pegoretti, A.; Pugno, N. Nanoscale friction of graphene oxide over glass-fibre and polystyrene. *Composites Part B: Engineering* **2018**, *148*, 272-280.
96. Mahmood, H.; Tripathi, M.; Pugno, N.; Pegoretti, A. Enhancement of interfacial adhesion in glass fiber/epoxy composites with graphene-coated fibers. *Composites Science and Technology* **2016**, *126*, 149-157.
97. Lu, Z.; Xian, G.; Li, H. Effects of elevated temperatures of the mechanical properties of basalt fibers and BFRP plates. *Construction and Builiding Materials* **2016**, *127*, 1029-1036.

98. Morova, N. Investigation of usability of basalt fibers in hot mix asphalt concrete. *Construction and Builiding Materials* **2013**, *47*, 175-180.
99. Foster, T.; Mader, E. Performance of modified basalt fibres. In Proceedings of the Proceedings of the 18th International Conference on Composite Materials (ICCM18), Jeju, Korea, **2011**.
100. Turkey, J.W. *Exploratory Data Analysis*. **1977**, 131-160.
101. Cescato, R.; Rigotti, D.; Mahmood, H.; Dorigato, A. Thermal mending of electroactive carbon/epoxy laminates using a porous poly (ε-caprolactone) electrospun mesh. *Polymers* **2021**, *13*, 2723-2744.
102. Cai G.; Wada M.; Ohsawa I.; Kitaoka S.; J., T. Influence of treatment with superheated steam on tensile properties of carbon fiber. *Composites Part A: Applied Science and Manufacturing* **2018**, *107*, 555-560.
103. Dsouza, R.; Antunes, P.; Kakkonen, M.; Tanhuanpaa, O.; Laurikainen, P.; KJavanshour, F.; Kallio, P.; Kanerva, M. Microscale sensor solution for data collection from fibre-matrix interfaces. *Scientific Reports* **2021**, *11*, 8346-8358.
104. Ash, J.T.; Cross, W.M.; Svalstad, D.; Kellar, J.J.; Kjerengtroen, L. Finite element evaluation of the microbond test: meniscus effect, interphase region, and vise angle. *Composites Science and Technology* **2003**, *63*, 641-651.
105. Badri, W.; Miladi, K.; Nazari, Q.A.; Fessi, H.; Elaissari, A. Effect of process and formulation parameters on polycaprolactone nanoparticles prepared by solvent displacement. *Colloids and Surfaces A: Physicochemical and Engineering Aspects* **2017**, *561*, 238-244.
106. Besra, L.; Liu, M. A review on fundamentals and applications of electrophoretic deposition (EPD). *Progress in Materials Science* **2007**, *52*, 1-61.
107. Loss J.; Khachatryan A.; Ogawa M.; Godber J.; F., S. Random centroid optimization of phosphatidylglycerol stabilized lutein-enriched oil-in-water emulsions at acidic pH. *Food Chemistry* **2005**, *92*, 737-744.

108. Medrzycka, K.B. The effect of particle concentration on zeta potential in extremely dilute solutions. *Colloid & Polymer Science* **1991**, *269*, 85-90.
109. Karger-Kocsis, J. Self-healing properties of epoxy resins with poly(ε-caprolactone) healing agent. *Polymer Bulletin* **2016**, *73*, 3081-3093.
110. Wei, H.; Yao, Y.; Liu, Y.; Leng, J. A dual-functional polymeric system combining shape memory with self-healing properties. *Composites Part B: Engineering* **2015**, *83*, 7-13.
111. Wang, B.; Lee, T.; Chang, E.; Yang, C. The shear strength and the failure mode of plasma-sprayed hydroxyapatite coating to bone: The effect of coating thickness. *Journal of biomedical materials research* **1993**, *27*, 1315-1327.
112. Greving, D.J.; Shadley, J.R.; Rybicki, E.F. Effects of Coating Thickness and Residual Stresses on the Bond Strength of ASTM C633-79 Thermal Spray Coating Test Specimens *ASM International* **1994**, *3*, 371-378.
113. K. Van de Velde, P.K. Biopolymers: overview of several properties and consequences on their applications. *Polymer Testing* **2002**, *21*, 433-442.
114. Schnepp, Z. Biopolymers as a flexible resource for nanochemistry. *Angewandte Chemie International Edition* **2013**, *52*, 1096-1108.
115. Dong, K.; Panahi-Sarmad, M.; Cui, Z.; Huang, X.; Xiao, X. Electro-induced shape memory effect of 4D printed auxetic composite using PLA/TPU/CNT filament embedded synergistically with continuous carbon fiber: A theoretical & experimental analysis. *Composites Part B: Engineering* **2021**, *220*, 108994-109005.
116. Hall, A.R.; Geoghegan, M. Polymers and biopolymers at interfaces. *Reports on Progress in Physics* **2018**, *81*, 1-37.
117. Dintcheva, N.T.; D'Anna, F. Anti-/Pro-Oxidant Behavior of Naturally Occurring Molecules in Polymers and Biopolymers: A Brief Review. *ACS Sustainable Chemistry & Engineering* **2019**, *7*, 12656-12670.

118. Lee, N.-K. Dynamics and Kinetics of Polymers and Biopolymers. *Journal of the Korean Physical Society* **2018**, *73*, 488-503.
119. Murariu, M.; Dubois, P. PLA composites: From production to properties. *Advanced Drug Delivery Reviews* **2016**, *107*, 17-46.
120. Ilyas, R.A.; Sapuan, S.M.; Harussani, M.M.; Hakimi, M.; Haziq, M.Z.M.; Atikah, M.S.N.; Asyraf, M.R.M.; Ishak, M.R.; Razman, M.R.; Nurazzi, N.M. Polylactic Acid (PLA) Biocomposite: Processing, Additive Manufacturing and Advanced Applications. *Polymers* **2021**, *13*, 1326.
121. McKeown, P.; Jones, M.D. The Chemical Recycling of PLA: A Review. *Sustainable Chemistry* **2020**, *1*, 1-22.
122. Rigotti, D.; Checchetto, R.; Tarter, S.; Caretti, D.; Rizzuto, M.; Fambri, L.; Pegoretti, A. Polylactic acid-lauryl functionalized nanocellulose nanocomposites: Microstructural, thermo-mechanical and gas transport properties. *Express Polymer Letters* **2019**, *13*, 858-876.
123. Rigotti, D.; Fambri, L.; Pegoretti, A. Bio-composites for fused filament fabrication: effects of maleic anhydride grafting on poly(lactic acid) and microcellulose. *Progress in Additive Manufacturing* **2022**, *7*, 765-783.
124. Fredi, G.; Karimi Jafari, M.; Dorigato, A.; Bikiaris, D.N.; Checchetto, R.; Favaro, M.; Brusa, R.S.; Pegoretti, A. Multifunctionality of Reduced Graphene Oxide in Bioderived Polylactide/Poly(Dodecylene Furanoate) Nanocomposite Films. *Molecules* **2021**, *26*, 2938-2965.
125. Fredi, G.; Dorigato, A.; Bikiaris, D.N.; Checchetto, R.; Pegoretti, A. Furanoate Polyesters/Polylactide/Reduced Graphene Oxide Nanocomposite Films: Thermomechanical and Gas Permeation Properties. *Macromolecular Symposia* **2022**, *405*, 2100208-2100212.
126. Fredi, G.; Dorigato, A.; Dussin, A.; Xanthopoulou, E.; Bikiaris, D.N.; Botta, L.; Fiore, V.; Pegoretti, A. Compatibilization of Polylactide/Poly(ethylene 2,5-

furanoate) (PLA/PEF) Blends for Sustainable and Bioderived Packaging. *Molecules* **2022**, *27*, 6371-6393.
127. Rigotti, D.; Soccio, M.; Dorigato, A.; Gazzano, M.; Siracusa, V.; Fredi, G.; Lotti, N. Novel Biobased Polylactic Acid/Poly(pentamethylene 2,5-furanoate) Blends for Sustainable Food Packaging. *ACS Sustainable Chemistry & Engineering* **2021**, *9*, 13742-13750.
128. Liu, H.; Zhang, J. Research progress in toughening modification of poly(lactic acid). *Journal of Polymer Science Part B: Polymer Physics* **2011**, *49*, 1051-1083.
129. Azadi, M.; Dadashi, A.; Dezianian, S.; Kianifar, M.; Torkaman, S.; Chiyani, M. High-cycle bending fatigue properties of additive-manufactured ABS and PLA polymers fabricated by fused deposition modeling 3D-printing. *Forces in Mechanics* **2021**, *3*, 100016-100027.
130. da Silva Barbosa Ferreira, E.; Luna, C.B.B.; Siqueira, D.D.; Araújo, E.M.; de França, D.C.; Wellen, R.M.R. Annealing Effect on Pla/Eva Blends Performance. *Journal of Polymers and the Environment* **2021**, *30*, 541-554.
131. Gigante, V.; Canesi, I.; Cinelli, P.; Coltelli, M.B.; Lazzeri, A. Rubber Toughening of Polylactic Acid (PLA) with Poly(butylene adipate-co-terephthalate) (PBAT): Mechanical Properties, Fracture Mechanics and Analysis of Ductile-to-Brittle Behavior while Varying Temperature and Test Speed. *European Polymer Journal* **2019**, *115*, 125-137.
132. Koh, J.J.; Zhang, X.; He, C. Fully biodegradable Poly(lactic acid)/Starch blends: A review of toughening strategies. *International Journal of Biological Macromolecules* **2018**, *109*, 99-113.
133. Tee, Y.B.; Talib, R.A.; Abdan, K.; Chin, N.L.; Basha, R.K.; Yunos, K.F.M. Toughening Poly(Lactic Acid) and Aiding the Melt-compounding with Bio-sourced Plasticizers. *Agriculture and Agricultural Science Procedia* **2014**, *2*, 289-295.
134. Meesorn, W.; Calvino, C.; Natterodt, J.C.; Zoppe, J.O.; Weder, C. Bio-Inspired, Self-Toughening Polymers Enabled

by Plasticizer-Releasing Microcapsules. *Advanced Materials* **2019**, *31*, 1807212-1807220.

135. Yang, Y.; Zhang, L.; Xiong, Z.; Tang, Z.; Zhang, R.; Zhu, J. Research progress in the heat resistance, toughening and filling modification of PLA. *Science China Chemistry* **2016**, *59*, 1355-1368.
136. Aliotta, L.; Cinelli, P.; Coltelli, M.B.; Lazzeri, A. Rigid filler toughening in PLA-Calcium Carbonate composites: Effect of particle surface treatment and matrix plasticization. *European Polymer Journal* **2019**, *113*, 78-88.
137. Qian, S.; Sheng, K. PLA toughened by bamboo cellulose nanowhiskers: Role of silane compatibilization on the PLA bionanocomposite properties. *Composites Science and Technology* **2017**, *148*, 59-69.
138. Petchwattana, N.; Naknaen, P.; Narupai, B. Combination effects of reinforcing filler and impact modifier on the crystallization and toughening performances of poly(lactic acid). *Express Polymer Letters* **2020**, *14*, 848-859.
139. Krishnan, S.; Pandey, P.; Mohanty, S.; Nayak, S.K. Toughening of Polylactic Acid: An Overview of Research Progress. *Polymer-Plastics Technology and Engineering* **2015**, *55*, 1623-1652.
140. Fekete, I.; Ronkay, F.; Lendvai, L. Highly toughened blends of poly(lactic acid) (PLA) and natural rubber (NR) for FDM-based 3D printing applications: The effect of composition and infill pattern. *Polymer Testing* **2021**, *99*, 107205-107215.
141. Mehrabi Mazidi, M.; Edalat, A.; Berahman, R.; Hosseini, F.S. Highly-Toughened Polylactide- (PLA-) Based Ternary Blends with Significantly Enhanced Glass Transition and Melt Strength: Tailoring the Interfacial Interactions, Phase Morphology, and Performance. *Macromolecules* **2018**, *51*, 4298-4314.
142. Chen, H.; Yu, X.; Zhou, W.; Peng, S.; Zhao, X. Highly toughened polylactide (PLA) by reactive blending with novel polycaprolactone-based polyurethane (PCLU) blends. *Polymer Testing* **2018**, *70*, 275-280.

143. Sanchez-Safont, E.L.; Arrillaga, A.; Anakabe, J.; Cabedo, L.; Gamez-Perez, J. Toughness Enhancement of PHBV/TPU/Cellulose Compounds with Reactive Additives for Compostable Injected Parts in Industrial Applications. *International Journal of Molecular Sciences* **2018**, *19*, 2102-2112.
144. Jiang, J.; Su, L.; Zhang, K.; Wu, G. Rubber-toughened PLA blends with low thermal expansion. *Journal of Applied Polymer Science* **2013**, *128*, 3993-4000.
145. Yeo, J.C.C.; Lin, T.T.; Koh, J.J.; Low, L.W.; Tan, B.H.; Li, Z.; He, C. Insights into the nucleation and crystallization analysis of PHB-rubber toughened PLA biocomposites. *Composites Communications* **2021**, *27*, 100894-100900.
146. Dogan, S.K.; Reyes, E.A.; Rastogi, S.; Ozkoc, G. Reactive compatibilization of PLA/TPU blends with a diisocyanate. *Journal of Applied Polymer Science* **2014**, *131*, 40251-40260.
147. Kilic, N.T.; Can, B.N.; Kodal, M.; Özkoç, G. Reactive compatibilization of biodegradable PLA/TPU blends via hybrid nanoparticle. *Progress in Rubber, Plastics and Recycling Technology* **2021**, *37*, 301-326.
148. Pandey, K.; Antil, R.; Saha, S.; Jacob, J.; Balavairavan, B. Poly(lactic acid)/thermoplastic polyurethane/wood flour composites: evaluation of morphology, thermal, mechanical and biodegradation properties. *Materials Research Express* **2019**, *6*, 125306-125318.
149. Azadi, F.; Jafari, S.H.; Khonakdar, H.A.; Arjmand, M.; Wagenknecht, U.; Altstädt, V. Influence of Graphene Oxide on Thermally Induced Shape Memory Behavior of PLA/TPU Blends: Correlation with Morphology, Creep Behavior, Crystallinity, and Dynamic Mechanical Properties. *Macromolecular Materials and Engineering* **2020**, *306*, 2000576-2000588.
150. Dogan, S.K.; Boyacioglu, S.; Kodal, M.; Gokce, O.; Ozkoc, G. Thermally induced shape memory behavior, enzymatic degradation and biocompatibility of PLA/TPU blends:

"Effects of compatibilization". *Journal of the Mechanical Behavior of Biomedical Materials* **2017**, *71*, 349-361.

151. Datta, J.; Kasprzyk, P. Thermoplastic polyurethanes derived from petrochemical or renewable resources: A comprehensive review. *Polymer Engineering & Science* **2018**, *58*, 14-35.
152. Yao, Y.; Xiao, M.; Liu, W. A Short Review on Self-Healing Thermoplastic Polyurethanes. *Macromolecular Chemistry and Physics* **2021**, *222*, 2100002-2100012.
153. Han, J.-J.; Huang, H.-X. Preparation and characterization of biodegradable polylactide/thermoplastic polyurethane elastomer blends. *Journal of Applied Polymer Science* **2011**, *120*, 3217-3223.
154. Liu, Z.-W.; Chou, H.-C.; Chen, S.-H.; Tsao, C.-T.; Chuang, C.-N.; Cheng, L.-C.; Yang, C.-H.; Wang, C.-K.; Hsieh, K.-H. Mechanical and thermal properties of thermoplastic polyurethane-toughened polylactide-based nanocomposites. *Polymer Composites* **2014**, *35*, 1744-1757.
155. Dorigato, A.; Sebastiani, M.; Pegoretti, A.; Fambri, L. Effect of Silica Nanoparticles on the Mechanical Performances of Poly(Lactic Acid). *Journal of Polymers and the Environment* **2012**, *20*, 713-725.
156. Fambri, L.; Dorigato, A.; Pegoretti, A. Role of Surface-Treated Silica Nanoparticles on the Thermo-Mechanical Behavior of Poly(Lactide). *Applied Sciences* **2020**, *10*, 6731.
157. Tait, M.; Pegoretti, A.; Dorigato, A.; Kalaitzidou, K. The effect of filler type and content and the manufacturing process on the performance of multifunctional carbon/poly-lactide composites. *Carbon* **2011**, *49*, 4280-4290.
158. Ye, W.; Dou, H.; Cheng, Y.; Zhang, D. Self-sensing properties of 3D printed continuous carbon fiber-reinforced PLA/TPU honeycomb structures during cyclic compression. *Materials Letters* **2022**, *317*, 132077-132081.
159. Lin, M.-C.; Lin, J.-H.; Bao, L. Applying TPU blends and composite carbon fibers to flexible electromagnetic-shielding fabrics: Long-fiber-reinforced thermoplastics

technique. *Composites Part A: Applied Science and Manufacturing* **2020**, *138*, 106022-106031.

160. Huang, J.; Liu, H.; Lu, X.; Qu, J. Thermal and mechanical properties of TPU/PBT reinforced by carbon fiber. *AIP Publishing* **2016**, *1713*, 120003-112009.
161. Raphael, N.; Namratha, K.; Chandrashekar, B.N.; Sadasivuni, K.K.; Ponnamma, D.; Smitha, A.S.; Krishnaveni, S.; Cheng, C.; Byrappa, K. Surface modification and grafting of carbon fibers: A route to better interface. *Progress in Crystal Growth and Characterization of Materials* **2018**, *64*, 75-101.
162. Zhang, G.; Sun, S.; Yang, D.; Dodelet, J.-P.; Sacher, E. The surface analytical characterization of carbon fibers functionalized by H2SO4/HNO3 treatment. *Carbon* **2008**, *46*, 196-205.
163. Davachi, S.M.; Kaffashi, B. Preparation and Characterization of Poly L-Lactide/Triclosan Nanoparticles for Specific Antibacterial and Medical Applications. *International Journal of Polymeric Materials and Polymeric Biomaterials* **2015**, *64*, 497-508.
164. Rahmanian, S.; Suraya, A.R.; Zahari, R.; Zainudin, E.S. Synthesis of vertically aligned carbon nanotubes on carbon fiber. *Applied Surface Science* **2013**, *271*, 424-428.
165. Zhang, Y.; Zhu, S.; Liu, Y.; Yang, B.; Wang, X. The mechanical and tribological properties of nitric acid-treated carbon fiber-reinforced polyoxymethylene composites. *Journal of Applied Polymer Science* **2015**, *15*, 132-140.
166. Tiwari, S.; Bijwe, J.; Panier, S. Tribological studies on polyetherimide composites based on carbon fabric with optimized oxidation treatment. *Wear* **2011**, *271*, 2252-2260.
167. Hong, H.; Yang, L.; Yuan, Y.; Qu, X.; Chen, F.; Wei, J.; Liu, C. Preparation, rheological properties and primary cytocompatibility of TPU/PLA blends as biomedical materials. *Journal of Wuhan University of Technology-Mater* **2016**, *31*, 211-218.

168. Yin, X.; Wang, L.; Li, S.; He, G.; Yang, Z.; Feng, Y.; Qu, J. Preparation and characterization of carbon fiber/polylactic acid/thermoplastic polyurethane (CF/PLA/TPU) composites prepared by a vane mixer. *Journal of Polymer Engineering* **2017**, *37*, 355-364.
169. Bindu, P.; Thomas, S. Viscoelastic behavior and reinforcement mechanism in rubber nanocomposites in the vicinity of spherical nanoparticles. *Journal of Physical Chemistry B* **2013**, *117*, 12632-12648.
170. Pistor, V.; Ornaghi, H.L.; Ferreira, C.A.; Zattera, A.J. Performance of poly(ethylene-co-vinyl acetate) nanocomposites using distinct clays. *Journal of Applied Polymer Science* **2012**, *125*, 462-470.
171. Chua, P.S. Dynamic mechanical analysis studies of the interphase. *Polymer composites* **1987**, *8*, 308-313.
172. Abu-Jdayil, B.; Mourad, A.H.; Hittini, W.; Hassan, M.; Hameedi, S. Traditional, state-of-the-art and renewable thermal building insulation materials. *Construction and Building Materials* **2019**, *214*, 709-735.
173. Vasilache, M.; Pruteanu, M.; Avram, C. Use of waste materials for thermal insulation in buildings. *Environmental Engineering and Management Journal* **2010**, *9*, 1275-1280.
174. Massoudinejad, M.; Amanidaz, N.; Santos, R.M.; Bakhshoodeh, R. Use of municipal, agricultural, industrial, construction and demolition waste in thermal and sound building insulation materials: A review article. *Journal of Environmental Health Science and Engineering* **2019**, *17*, 1227-1242.
175. Gama, N.V.; Ferreira, A.; Barros-Timmons, A. Polyurethane foams: Past, present, and future. *Materials* **2018**, *11*, 1841-1876.
176. Ates, M.; Karadag, S.; Eker, A.A.; Eker, B. Polyurethane foam materials and their industrial applications. *Polymer International* **2022**, *71*, 1157-1163.
177. Saint-Michel F; Chazeau L; Cavaillé JY; E, C. Mechanical properties of high density polyurethane foams: I. Effect of

the density. *Composites Science and Technology* **2006**, *66*, 2700-2708.
178. Zhang, H.; Fang, W.Z.; Li, Y.M.; Tao, W.Q. Experimental study of the thermal conductivity of polyurethane foams. *Applied Thermal Engineering* **2017**, *115*, 528-538.
179. Quadrini, F.; Bellisario, D.; Santo, L. Recycling of thermoset polyurethane foams. *Polymer Engineering & Science* **2013**, *53*, 1357-1363.
180. Magnin, A.; Entzmann, L.; Bazin, A.; Pollet, E.; Avérous, L. Green Recycling Process for Polyurethane Foams by a Chem-Biotech Approach. *Chemistry Europe* **2021**, *14*, 4234-4241.
181. Zhang L; Liang S; Z, C. Influence of particle size and addition of recycling phenolic foam on mechanical and flame retardant properties of wood-phenolic composites. *Construction and Building Materials* **2018**, *168*, 1-10.
182. Kemona, A.; Piotrowska, M. Polyurethane recycling and disposal: Methods and prospects. *Polymers* **2020**, *12*, 1752-1787.
183. Mougel, C.; Garnier, T.; Cassagnau, P.; Sintes-Zydowicz, N. Phenolic foams: A review of mechanical properties, fire resistance and new trends in phenol substitution. *Polymer* **2019**, *164*, 86-117.
184. Song, S.A.; Chung, Y.S.; Kim, S.S. The mechanical and thermal characteristics of phenolic foams reinforced with carbon nanoparticles. *Composites Science and Technology* **2014**, *103*, 85-93.
185. Sarika, P.R.; Nancarrow, P.; Khansaheb, A.; Ibrahim, T. Progress in Bio-Based Phenolic Foams: Synthesis, Properties, and Applications. *Chemical and Biomolecular Engineering* **2021**, *8*, 612-632.
186. Auad, M.L.; Zhao, L.; Shen, H.; Nutt, S.R.; Sorathia, U. Flammability properties and mechanical performance of epoxy modified phenolic foams. *Journal of Applied Polymer Science* **2007**, *104*, 1399-1407.

187. Del Saz-Orozco, B.; Alonso, M.V.; Oliet, M.; Domínguez, J.C.; Rodriguez, F. Mechanical, thermal and morphological characterization of cellulose fiber-reinforced phenolic foams. *Composites Part B: Engineering* **2015**, *75*, 367-372.
188. Yang, C.; Zhuang, Z.H.; Yang, Z.G. Pulverized polyurethane foam particles reinforced rigid polyurethane foam and phenolic foam. *Journal of Applied Polymer Science* **2014**, *131*, 1-7.
189. Ebaid, R.; Wang, Q.; Faisal, S.; Li, L.; Abomohra, A. Valorization of floral foam waste via pyrolysis optimization for enhanced phenols recovery. *Chemosphere* **2023**, *310*, 136758-136768.
190. Beran, R.; Zarybnicka, L.; Machova, D. Recycling of rigid polyurethane foam: Micro-milled powder used as active filler in polyurethane adhesives. *Journal of Applied Polymer Science* **2020**, *137*, 49095-49106.
191. Drozdov, A.; Claville, C. The effect of porosity on elastic moduli of polymer foams. *Journal of Applied Polymer Science* **2020**, *137*, 1-10.
192. Papadopoulos, A.M. State of the art in thermal insulation materials and aims for future developments. *Energy and buildings* **2005**, *37*, 77-86.
193. Schartel, B.; Hull, T.R. Development of fire-retarded materials. Interpretation of cone calorimeter data. *Fire and Materials* **2007**, *31*, 327-354.
194. Hidalgo, J.P.; Torero, J.L.; Welch, S. Fire performance of charring closed-cell polymeric insulation materials: Polyisocyanurate and phenolic foam. *Fire and Materials* **2018**, *41*, 358-373.
195. Tang, K.; He, X.; Xu, G.; Tang, X.; Ge, T.; Zhang, A. Effect of formaldehyde to phenol molar ratio on combustion behavior of phenolic foam. *Polymer Testing* **2022**, *111*, 107626-107634.
196. Babrauskas, V.; Peacock, R.D. Heat release rate: the single most important variable in fire hazard. *Fire safety journal* **1992**, *18*, 255-272.

Scientific production

(Updated to June 28th, 2024)

Published

- Mahmood, H.; Simonini, L.; Dorigato, A.; Pegoretti, A. Graphene deposition on glass fibers by triboelectrification. *Applied Sciences* **2021**, *11*, 3123-3135.
- Simonini, L.; Mahmood, H.; Dorigato, A.; Pegoretti, A. Tailoring the physical properties of poly (lactic acid) through the addition of thermoplastic polyurethane and functionalized short carbon fibers. *Polymer Composites* **2023**, *44*, 4719-33.
- Simonini, L.; Mahmood, H.; Dorigato, A.; Pegoretti, A. Evaluation of self-healing capability of a polycaprolactone interphase in epoxy/glass composites. *Composites Part A: Applied Science and Manufacturing* **2023**, *169*, 107539-107548.
- Simonini, L.; Canale, R.; Mahmood, H.; Dorigato, A.; Pegoretti, A. Multifunctional epoxy/carbon composites with a fully reparable interface. *Polymer Composites* **2024**, 45, 2558-2568.

In press

- Pozueco, S.; Simonini, L.; Mahmood, H.; Kakkonen, M.; Riveiro, A.; Comesaña, A.; Pou, J.; Tanhuanpää, O.; Kanerva, M.; Sarlin, E.; Kallio, P.; Pegoretti, A. Influence of CO_2 laser surface treatment of basalt fibres on the mechanical properties of epoxy/basalt composites. To *Polymer Composites.*

Under review

- Simonini, L.; Sorze, A.; Maddalena, L.; Carosio, F.; Dorigato, A. Mechanical reprocessing of polyurethane and phenolic foams to increase the sustainability of thermal insulation materials. To *Polymer Testing..*

In preparation

- Simonini, L.; Kakkonen, M.; Dsouza, R.; Kanerva, M; Mahmood, H.; Dorigato, A.; Pegoretti, A. Tailoring the interfacial properties of glass fiber/epoxy microcomposites through the development of a multifunctional poly (ϵ-caprolactone) interphase.

Awards

(Updated to June 28th, 2024)

National awards

- **SCI/ISE/INSTM – Best Poster Award** - "Self-healing of polycaprolactone (PCL) coated glass fiber/epoxy interface". National Interuniversity Consortium of Materials Science and Technology (INSTM), January 23-26th 2022, Sestriere (Italy).

International awards

- **Best young researcher – Best Oral Award** - "Graphene coatings for glass fibers through triboelectrification". Times of Polymer and Composites (TOP), September 5-9th 2021, Ischia (Italy).
- **Best poster Award** - "Investigation of the interfacial self-healing properties of polycaprolactone coated glass fibers/epoxy microcomposites". Milan polymers days (MIPOL), June 19-21th 2022, Milan (Italy).

Participation to Congress and Schools

(Updated to June 28th, 2024)

National congress contributions

- Simonini L, Mahmood H, Dorigato A, Pegoretti A. **"Development of graphene coatings for glass fibers through contact electrification"**. Associazione Italiana di Ingegneria dei Materiali (AIMAT), September 15-19th 2021, Cagliari (Italy).
- Simonini L, Mahmood H, Dorigato A, Pegoretti A. **"Self-healing of polycaprolactone (PCL) coated glass fiber/epoxy interface". N**ational Interuniversity Consortium of Materials Science and Technology (INSTM), January 23-26th 2022, Sestriere (Italy).
- Simonini L, Mahmood H, Dorigato A, Pegoretti A. **"Investigation of the interfacial self-healing properties of polycaprolactone coated glass fibers/epoxy composites".** Associazione Italiana di Scienza e Tecnologia delle Macromolecole (AIM), September 4-7th 2022, Trento (Italy).
- Simonini L, Mahmood H, Dorigato A, Pegoretti A. **"Studio di deposizione di grafene su fibre di vetro tramite triboelettrificazione".** Consorzio Interuniversitario Nazionale per la Scienza e Tecnologia dei Materiali (INSTM), January 22-25th 2023, Bressanone (Italy).
- Simonini L, Mahmood H, Dorigato A, Pegoretti A. **"Self-healing of functionalized interphases made of polycaprolactone coated glass fibers for composite applications".** Associazione Italiana di Scienza e Tecnologia delle Macromolecole (AIM - MACROGIOVANI), June 21-23th 2023, Catania (Italy).
- Simonini L, Mahmood H, Dorigato A, Pegoretti A. **"Self-healing interphase in polymer composites".** Associazione

Italiana di Scienza e Tecnologia delle Macromolecole (AIM - MACROGIOVANI), June 12-13th 2024, Rimini (Italy).

International congress contributions

- Simonini L, Mahmood H, Dorigato A, Pegoretti A. **"Graphene coatings for glass fibers through triboelectrification".** Times of Polymer and Composites (TOP), September 5-9th 2021, Ischia (Italy).
- Simonini L, Mahmood H, Dorigato A, Pegoretti A. **"Investigation of the interfacial self-healing properties of polycaprolactone coated glass fibers/epoxy composites".** International Conference on applied surface science (ICASS) , April 25 – 28th 2022, Palma de Mallorca (Spain).
- Simonini L, Mahmood H, Dorigato A, Pegoretti A. **"Investigation of the interfacial self-healing properties of polycaprolactone coated glass fibers/epoxy microcomposites"**. Milan polymers days (MIPOL), June 19-21th 2022, Milan (Italy).
- Simonini L, Mahmood H, Dorigato A, Pegoretti A. **"Evaluation of the self-healing capability of a polycaprolactone functionalized interphase for polymer composite applications".** European Conference on Composite Materials (ECCM), June 26-30th 2022, Lausanne (Switzerland).
- Simonini L, Mahmood H, Dorigato A, Pegoretti A. **"Evaluation of interfacial adhesion and self-healing in multifunctional composites".** Times of Polymer and Composites (TOP), June 11-15th 2023, Ischia (Italy). – **invited speaker**
- Simonini L, Mahmood H, Dorigato A, Pegoretti A. **"Development of a self-healing interphase for structural composites".** International Conference on Composite Materials (ICCM), August 1-6th 2023, Belfast (Northern Ireland).

- Simonini L. **"Multifunctional self-healing interphases for novel composite materials".** International Symposium on Current challenges of wind energy development, May 13-15th 2024, Athens (Greece) – **invited speaker**

Summer school

21th AIMAT School "**I Materiali nella Transizione Energetica**". AIMAT, July 13-16th 2022, Ischia (Italy).

Visiting period abroad

(Updated to June 28th, 2024)

Visiting PhD Student at the Faculty of Engineering and Natural Sciences - Tampere University (Finland) from 13/02/2023 to 16/04/2023. The vesting period was founded by ECIU research mobility found Programme.

Teaching activities

(Updated to June 28th, 2024)

- Tutor activity for the laboratory part of the course of "**Laboratorio di tecnologie delle materie plastiche**" during the second semester of the AY 2021-22, Materials and production engineering University of Trento, Department of Industrial Engineering.
- Tutor activity for the laboratory part of the course of "**Laboratorio di tecnologie delle materie plastiche**" during the second semester of the AY 2022-23, Materials and production engineering University of Trento, Department of Industrial Engineering.
- Tutor activity for the laboratory part of the course of "**Polymeric and composite materials engineering**" during the second semester of the AY 2022-23, Materials and production engineering University of Trento, Department of Industrial Engineering.
- Tutor activity for the laboratory part of the course of "**Laboratorio di tecnologie delle materie plastiche**" during the second semester of the AY 2023-24, Materials and production engineering University of Trento, Department of Industrial Engineering.

Acknowledgements

The completion of this PhD thesis was possible thanks to the support and contributions of many people. I am deeply grateful to all those who helped me along this path.
First of all, I would like to express my gratitude to my supervisors, Prof. Alessandro Pegoretti and Prof. Andrea Dorigato. Your guidance, profound knowledge, and continuous encouragement have been fundamental throughout my research. I thank you because you have given me the intellectual freedom to explore new ideas and your constructive feedback has been invaluable.
I would also like to extend my thanks to my co-supervisor, Dr. Haroon Mahmood. From my Master's thesis to the completion of my PhD, your insightful suggestions, expertise and dedicated involvement in my work have contributed significantly to my academic growth. Your support has been important during my research journey and I deeply appreciate your guidance and encouragement over the years.
Thanks also to Alfredo, Claudia, the laboratory technicians, whose technical expertise and assistance were sometimes crucial in the experimental part of my research. Your availability and contributions were essential for the practical aspects of this thesis.
During my visit to Tampere, Finland, I had the opportunity to work under the supervision of Prof. Mikko Kanerva. Thank you, Mikko, for welcoming me and providing an enriching and stimulating environment for my research abroad. I am also grateful to Dr. Markus Kakkonen, Dr. Royson Dsouza, Dr. Olli Tanhuanpää, Prof. Essi Sarlin, Prof. Pasi Kallio and Dr. Lijo George for their cooperation and support during this time. Your help in the experimental part of my research was crucial and I really appreciated your willingness to share your knowledge and expertise.
I am lucky to have had the support of my colleagues Marica, Sereno, Davide, Daniele, Edoardo, Lorenzo, Francesco, Giulia, Sofia,

Gabriele and Marco. Your friendliness and cooperation made this trip a pleasant experience. Marica, in particular, has been a valuable colleague and a true friend, and for this I am deeply grateful for our friendship.
Special thanks go to my parents, Loris and Margherita, to whom I express my gratitude for their love, encouragement and sacrifices. You have been and will always be my pillars of strength and my source of inspiration. Thank you for always believing in me and giving me the opportunity to pursue my dreams. To all my family members, your support has been a constant source of motivation during my academic journey.
Un ringraziamento speciale va ai miei genitori, Loris e Margherita, ai quali esprimo la mia gratitudine per il loro amore, il loro incoraggiamento e i loro sacrifici. Siete stati e sarete sempre i miei pilastri di forza e la mia fonte di ispirazione. Grazie per aver sempre creduto in me e per avermi dato l'opportunità di perseguire i miei sogni. A tutti i miei familiari, il vostro sostegno è stato una costante fonte di motivazione durante il mio percorso accademico.
I would like to thank Alessandro, with whom I have shared joys, exams and experiences since the first year of the Bachelor's degree. Sharing this academic journey with you, from undergraduate studies to the completion of our PhD, has been an incredible experience. The support and shared enthusiasm for our common scientific interest have been and will always be a great source of strength.
Finally, I would also like to thank my friends Riccardo and Gabriel, whose friendship has been a constant source of support and joy since the first year of our Bachelor's degree. Riccardo, your collaboration in one of my PhD research projects was precious and I am deeply grateful for your contribution.